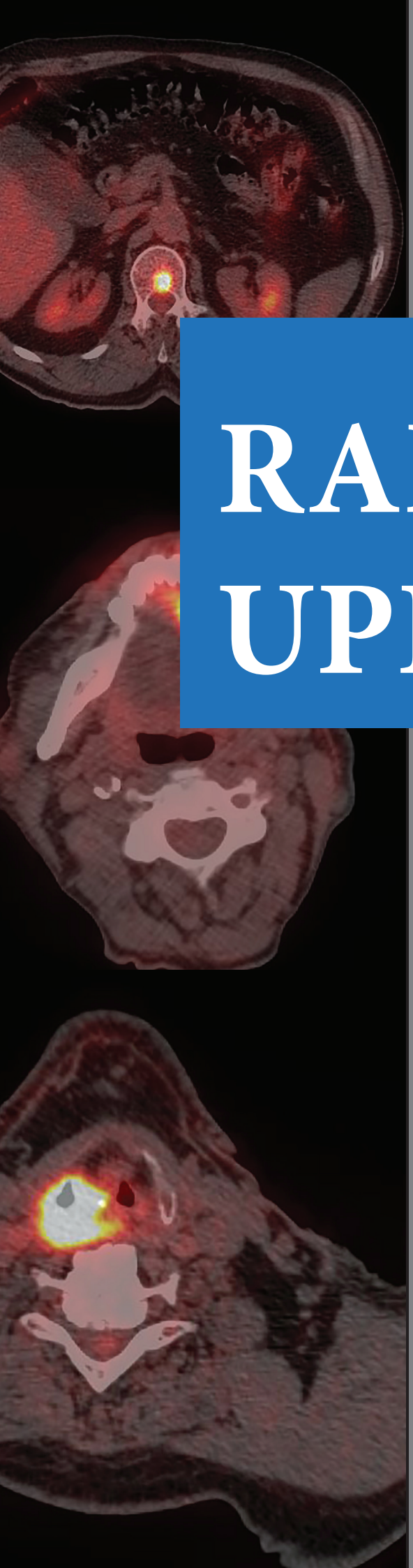

VOL. 2 (4). ISSN 2424-5755

# RADIOLOGY UPDATE

**JOURNAL available at radiologyupdate.org**

Online Journal

*Lithuanian Association of Radiologists*

This page is intentionally left blank

# Editorial board

Editor-in-chief: Prof. Algidas Basevicius

**MANAGING EDITORS:**

Prof. Saulius Lukosevicius
Prof. Rymante Gleizniene
Prof. Ilona Kulakiene
Prof. Egle Monastyreckiene
Prof. Algirdas Edvardas Tamosiunas
Prof. Nomeda Valeviciene
Prof. Vincentas Veikutis
Prof. Elona Juozaityte
Prof. Arturas Inciura
Assoc. Prof. Jurate Dementaviciene
Assoc. Prof. Antanas Jankauskas
Med. Dr. Arturas Samuilis
Prof. Dr. Renaldas Raisutis
Prof. Dr. Minvydas Ragulskis
Prof. Renaldas Jurkevicius
Prof. Remigijus Zaliunas

**INTERNATIONAL EDITORS**

**LATVIA:**

Prof. Gaida Krumina
Assist. Prof. Maija Radzina
Assoc. Prof. Karlis Kupcs
Assist. Prof. Peteris Prieditis

**ESTONIA:**

Prof. Sergei Nazarenko
Prof. Pilvi Ilves

**SWEDEN:**

Assoc. Prof. Augustinas Sakinis
Assoc. Prof. Karolina Kublickiene

**USA:**

Prof. Jovitas Skucas
Assoc. Prof. Arunas Gasparaitis

**UKRAINE:**

Dr. Tetyana Yalynska
Prof. Olena Sharmazanova
Prof. Volodymyr Rogozhyn
Prof. Tetyana Kozarenko

**CHINA:**

Assoc. Prof. Guang-qing Lu

**ADMINISTRATORS OF JOURNAL:**

Julius Vidikas
Tomas Budrys

This page is intentionally left blank

**CONTENTS**

Editorial board ..... 3

Gray-scale and Doppler ultrasound: significance in predicting malignancy of thyroid nodules .... 6

CT scan attenuation value measurement as a diagnostic tool for patients with pleural effusions ..... 15

Preoperative assessment of pancreatic adenocarcinoma. Value of CT imaging ..... 23

Radiologic imaging of the inflammatory renal diseases: literature review ..... 31

Application of Magnetic Resonance Imaging and
Computer Vision Technologies for Analysis of Knee Articular Cartilage Degeneration ..... 44

Positron emission tomography/computer tomography in the evaluation of head and
neck cancer treatment ..... 51

Congenital Lumbar hernia with lumbo-costo vertebral syndrome with ipsilateral short femur,
tibial and fibular hemimelia ..... 64

# Gray-scale and Doppler ultrasound: significance in predicting malignancy of thyroid nodules

**Gintaras Kuprionis[1], Raimondas Valickas[1], Rasita Pavilionė[1], Žygimantas Štaras[1], Ugnė Marcinkutė[1]**

[1]*Lithuanian University of Health Sciences, Kaunas, Lithuania*

## ABSTRACT

**Introduction:** There have been various systems for identifying risk of thyroid nodule malignancy using ultrasound (US), with the most recent being 2017 American College of Radiology proposed TI-RADS. However, this system does not take vascular patterns into account. The aim of this study is to determine the role of gray scale and color Doppler ultrasound in differentiating benign and malignant thyroid nodules

**Methods:** A total of 180 ultrasound images of patients with thyroid nodules were analyzed. Nodule composition, shape, margin, echogenicity, echogenic foci and vascular patterns were evaluated. The results were compared with histology findings

**Results:** 98 (54.4%) thyroid nodules were benign and 82 (45.5%) – malignant. Compared to malignant, more benign thyroid nodules (80.6%) were bigger than 1 cm, $p < 0.001$). Benign and malignant thyroid nodules did not significantly differ in frequency of composition or echogenicity ($p > 0.05$). Round and taller-than-wide shape, lobulated or irregular margin, microcalcifications were more common among malignant nodules ($p < 0.05$). Mean total TI-RADS score was significantly higher among malignant thyroid nodules compared to benign, $p < 0.001$. TI-RADS sensitivity in predicting the risk of malignancy was 82.9%, specificity – 69.4%, area under curve – 0.822, while vascularity had sensitivity of 40% and specificity of 36.7%. Mixed vascularity was more common among benign ($p = 0.003$) and weak perinodular vascularity was more common among malignant nodules ($p = 0.048$). Weak negative correlation was found between total amount of TI-RADS points and vascular patterns ($rs = - 0.238$, $p = 0.001$)

**Conclusions:** In our study irregular or lobulated margin, taller-than-wide shape and microcalcifications were more common among malignant thyroid nodules. While thyroid US using TI-RADS had good diagnostic value in predicting malignancy, vascular patterns had low sensitivity (40.2%) and specificity (36.7%). Thyroid nodules with intranodular vascularity had a lower TI-RADS score.

***Keywords:*** ultrasound, thyroid, malignancy.

## INTRODUCTION

With the introduction of high resolution ultrasound, the prevalence of thyroid nodules became exceedingly high – reaching up to 76% in adult population [1]. Even though such high prevalence is alarming, most of the nodules are benign with only a small fraction being malignant [2]. Fine-needle aspiration (FNA) cytology is a relatively easy and cost effective test to distinguish between the two [3]. However, it is not efficient to perform FNA on every single thyroid nodule case leading to overdiagnosis which would cause more harm than good [4]. Currently, thyroid ultrasound – a reliable and noninvasive method, is used to identify the probability of malignancy and the need for FNA.

There have been various systems for identifying risk of thyroid nodule malignancy using ultrasound (US), with the most recent being 2017 American College of Radiology proposed TI-RADS (Thyroid Imaging, Reporting and Data System). Using this system thyroid nodules are awarded points for their sonographic features: composition, echogen icity, shape, margin and echogenic foci [5]. However, this system does not take vascular patterns established with color Doppler US into account.

The aim of this study is to determine the role of gray scale and color Doppler ultrasound in differentiating benign and malignant thyroid nodules.

## LITERATURE REVIEW

### THYROID NODULES

The thyroid is an endocrine gland in the neck which plays an important role in metabolism by producing three hormones: Triiodothyronine (T3), Tetraiodothyronine (T4), Calcitonin, and releasing them into the bloodstream. American Thyroid Association describes thyroid nodules as "discrete lesions within the thyroid gland, radiologically distinct from surrounding thyroid parenchyma." [6]. These lesions are a common finding, with prevalence reaching up to 68-76% among adults [1,7]. There was a significant leap in prevalence of thyroid nodules due to introduction of high resolution ultrasound systems. Before, thyroid nodules were palpable only in 4-7% of population [8,9]. Most of the nodules are benign, with 10-15% being malignant [10,11].

Serum thyrotropin (TSH) and thyroid US are essential in thyroid nodule evaluation, with former providing important information about nodule functionality and latter – about the presence of sonographic features that suggest malignancy. Fine-needle aspiration cytology is the test that follows thyroid US if nodules are found to be suspicious. FNA is used to effectively determine thyroid nodule malignancy or the need for histological evaluation to reach a definitive decision [3,12]. Histologically thyroid cancer can be divided into four major types: papillary, follicular, medullary and anaplastic, with the most frequent being papillary thyroid carcinoma [13].

### THYROID ULTRASOUND

Thyroid sonography is an useful tool in evaluation of various thyroid disorders. According to American Association of Clinical Endocrinologists (AACE) and Associazione Medici Endocrinologi (AME) recommendations, thyroid ultrasound should be used [14,15]:

- To confirm the presence of thyroid nodules, to characterize them and to evaluate the risk of malignancy;
- To evaluate diffuse changes in thyroid parenchyma;
- To differentiate between thyroid nodules and other cervical masses;
- To detect post-operative residual or recurrent tumor in thyroid bed or metastases to neck lymph nodes;
- To screen high risk patients for thyroid malignancy (history of familial thyroid cancer, multiple endocrine neoplasia (MEN) type II and irradiated neck in childhood);
- To guide diagnostic and therapeutic interventional procedures.

As mentioned previously, thyroid ultrasound can be used to predict malignancy in thyroid nodules and to determine the need for FNA. Certain sonographic features: hypoechogenicity, taller-than-wide shape, irregular or lobulated margins, microcalcifications and increased intranodular vascularity were found to be independent risk factors suggesting malignancy [16-18]. However, 2017 American College of Radiology (ACR) TI-RADS regards solid composition of thyroid nodules as a suspicious feature and does not include vascular patterns at all [5]. Several other sources state that vascular patterns of thyroid nodules do not reflect risk of malignancy [19].

Reported diagnostic value of thyroid ultrasound in predicting malignancy varies by author. Sensitivity was reported to be as low as 41% or as high as 93%. Specificity and positive predictive value (PPV) ranged from 43 to 84% and from 34 to 74% respectively. However, reported negative predictive value (NPV) was high in most cases – ranging from 84 to 99.2% [20-22].

## METHODS AND MATERIALS

A retrospective study was performed, a total of 180 patient cases with thyroid nodules from 2014 to 2017 were analyzed in Lithuanian University of Health Sciences Kaunas Clinics. In all cases the definitive diagnosis was confirmed by post-operative histologic evaluation of surgical specimen. Patients' age, gender, sonographic features of thyroid nodules and results of cytological and histological evaluation were assessed.

Thyroid ultrasound procedure was performed as follows: patients were positioned lying face-up with a pillow placed under the shoulders to extend the area to be scanned, a linear transducer was used. Thyroid nodule composition, echogenicity, shape, margin, echogenic foci were

**Table 1. TI-RADS Categories**

| Composition | Echogenicity | Shape | Margin | Echogenic foci |
|---|---|---|---|---|
| Cystic or almost completely cystic – 0 pts. | Anechoic – 0 pts. | Wider-than-tall – 0 pts. | Smooth – 0 pts. | None or large comet-tail artifacts – 0 pts. |
| Spongiform – 0 pts. | Hyperechoic or isoechoic – 1 pts. | Taller-than-wide – 3 pts. | Ill-defined – 0 pts. | Macrocalcifications – 1 pts. |
| Mixed cystic or solid – 1 pts. | Hypoechoic – 2 pts. | | Lobulated or irregular – 2 pts. | Peripheral (rim) calcifications – 2 pts. |
| Solid or almost completely solid – 2 pts. | Very hypoechoic – 2 pts. | | Extra-thyroidal extension – 3 pts. | Punctate echogenic foci – 3 pts. |

Points awarded for sonographic features are then added. Depending on the total amount of points, thyroid nodules are assigned to one of the TI-RADS Levels (TR): TR1, TR2, TR3, TR4 or TR5 (Table 2) [5].

**Table 2. TI-RADS Levels**

| TI-RADS Level | Points |
|---|---|
| TR1 – Benign | 0 |
| TR2 – Not Suspicious | 2 |
| TR3 – Mildly Suspicious | 3 |
| TR4 – Moderately Suspicious | 4-6 |
| TR5 – Highly Suspicious | ≥ 7 |

Thyroid nodule size, presence of halo and vascular patterns were assessed as well. Vascular patterns were evaluated using Color Doppler US and assigned one of the following: absent vascular flow, exclusively weak or intense perinodular, exclusively weak or intense intranodular, mixed vascular flow. As suggested in 2017 ACR TI-RADS solid composition, hypoechogenicity, taller-than-wide shape, irregular or lobulated margin, punctate echogenic foci were considered as sonographic features suggesting malignancy, intranodular vascular pattern with or without perinodular vascularity was also considered as a sign of malignancy when evaluating the diagnostic value of vascularity (Fig. 1,2).

**Fig 1. Solid, very hypoechoic, taller-than-wide thyroid nodule with irregular margin, absent calcifications, weak perinodular and intranodular vascularity.**

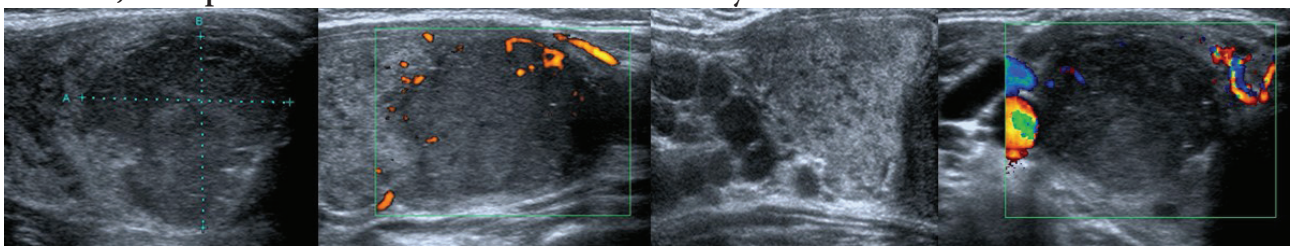

**Fig 2. Solid, hypoechoic, wider-than-tall thyroid nodule with lobulated margin, punctate echogenic foci, weak perinodular and intranodular vascularity.**

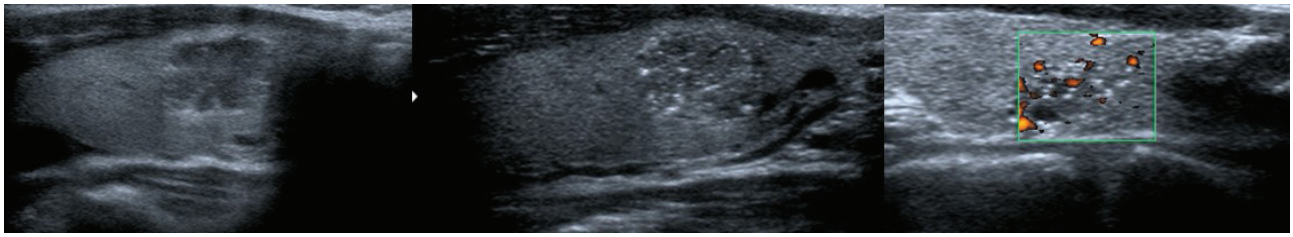

Statistical analysis was performed with "IBM SPSS Statistics 17.0" and "MedCalc 18.2.1". Descriptive statistics were given in form of means with standart deviation and minimum/maximum values of the variables. Student's t-test was used to compare means of two variables atleast on ordinal scale. Chi-squared test was used to compare two independant variables. Fisher's exact test was used to compare two independant variables if the sample sizes were small. Spearman correlation coefficient (rs) was used to evaluate the correlation between two variables – one on the interval and other on ordinal scale. Sensitivity, specificity and accuracy were calculated using ROC curve. Younden index (J) was used to find optimal cut-off value. Results were considered statistically significant with p values of 0.05 and lower.

## RESULTS

### DEMOGRAPHIC AND CLINICAL CHARACTERISTICS

Out of 180 cases that were analyzed, 22 (12.2%) patients were male and 158 (87.8%) – female. Patients' mean age was 54.38 ± 18.2 years, with the youngest being 12 and the oldest – 90 years. Mean age of male patients was 58.05 ± 19.7, female – 53.87 ± 18.0 years. Mean age of patients diagnosed with thyroid cancer was 52.9 ± 17.7, with benign nodules – 55.6 ± 18.7 years – higher compared to a study by Frates et al where mean age of patients with malignant and benign thyroid nodules was 46.2 ± 0.9 and 40.1 ± 0.3 respectively [23]. No significant differences between the age of male and female patients and between age of patients with malignant and benign thyroid nodules were found ($p > 0.05$).

Out of 180 thyroid nodules, 98 (54.4%) were benign and 82 (45.5%) were malignant. Diagnoses of all cases were verified by histologic evaluation of surgical specimen. In cases of malignant thyroid nodules, papillary thyroid carcinoma was the most common (90%) and medullary thyroid carcinoma – the least common (1.25%) diagnosis. Papillary and follicular thyroid cancer combined takes up 92.5% of the cases which matches the frequency mentioned in American Thyroid Association (ATA) guidelines (> 90%) [6]. Frequency of medullary thyroid cancer was lower than the one mentioned in a study by Ball – 2-5% of all thyroid cancer cases [24]. Distribution of thyroid cancer types found during histologic evaluation is shown in Fig 3.

**Fig 3. Types of thyroid cancer**

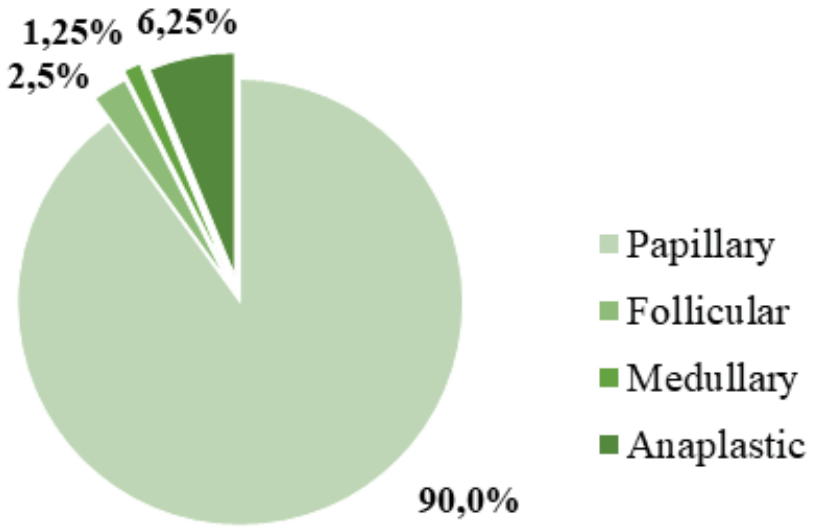

THYROID ULTRASOUND

Most of the benign thyroid nodules (80.6%) measured during thyroid US procedure were bigger than 1 cm. In comparison, number of malignant nodules that were smaller than 1 cm was significantly higher (53.7%) than benign (19.4%), $p < 0.001$. These results correspond to the conclusions of a study by Cavallo et al that larger nodules have lower malignancy rate [25]. 22 (22.4%) benign and 11 (13.4%) malignant thyroid nodules had a well-defined hypoechoic halo, which is usually a sign suggesting benignity [26], however, no significant difference was found between benign and malignant nodules ($p = 0.127$). In cases of multiple thyroid nodules malignancy was found in 19 (41.3%) cases, 27 (58.7%) were benign. Some authors have found that a higher number of thyroid nodules suggest a higher risk of malignancy [27], however, no significant differences in malignancy rates in cases of multiple thyroid nodules were found ($p = 0.607$).

Benign and malignant thyroid nodules did not significantly differ in composition ($p > 0.05$). Using 2017 ACR TI-RADS, mean score awarded for composition was $0.27 \pm 0.7$ for benign nodules and $1.35 \pm 1.45$ points for malignant nodules. No significant difference between these scores was found ($p = 0.651$). Distribution of thyroid nodule composition types established during thyroid US is shown in Table 3.

**Table 3. Thyroid nodules – composition**

| | All nodules | Benign | Malignant |
|---|---|---|---|
| Solid | 87 (48.3%) | 48 (48.5%) | 39 (47.6%) |
| Mixed cystic or solid | 89 (49.7%) | 46 (47.4%) | 43 (52.4%) |
| Spongiform | 4 (2.2%) | 4 (4.1%) | 0 |

Most of the thyroid nodules were hypoechoic (74.4%). In ACR TI-RADS hypoechogenicity is established as sign that suggests malignancy [5], however, there were no significant difference in frequency of hypoechogenicity among benign and malignant thyroid nodules ($p > 0.05$) No difference was found in scores awarded for echogenicity as well ($p = 0.281$), mean score that benign and malignant nodules were awarded was $2.23 \pm 0.76$ and $2.35 \pm 0.71$ points respectively. Distribution of thyroid nodule echogenicity established during thyroid US is shown in Table 4.

**Table 4. Thyroid nodules – echogenicity**

| | All nodules | Benign | Malignant |
|---|---|---|---|
| Hyperechoic | 5 (2.8%) | 4 (4.1%) | 1 (1.2%) |
| Isoechoic | 28 (15.6%) | 15 (15.3%) | 13 (15.9%) |
| Hypoechoic | 69 (38.3%) | 38 (38.8%) | 31 (37.8%) |
| Very hypoechoic | 78 (43.3%) | 41 (41.84%) | 37 (46.12%) |

Taller-than-wide shape is said to be a highly suggestive of malignancy [5,27], which corresponds to results found in this study as well – taller-than-wide shape was significantly more frequent among malignant nodules ($p = 0.005$). Round shape was also found to be more frequent among malignant nodules compared to benign ($p < 0.001$). Mean TI-RADS score reflects this as well – average amount of points awarded for shape to benign thyroid nodules was $0.12 \pm 0.6$ while malignant nodules were awarded significantly more points – $0.51 \pm 1.1$ ($p = 0.004$). Distribution of thyroid nodule shape established during thyroid US is shown in Table 5.

**Table 5. Thyroid nodules – shape**

| | All nodules | Benign | Malignant |
|---|---|---|---|
| Wider-than-tall | 119 (66.1%) | 85 (86.7%) | 34 (41.5%) |
| Taller-than-wide | 18 (10%) | 4 (4.1%) | 14 (17.1%) |
| Round | 43 (23.9%) | 9 (9.2%) | 34 (41.5%) |

Malignant thyroid nodules were found to have lobulated or irregular margins more often compared to benign nodules, $p < 0.001$. Also, mean score awarded to malignant nodules (0.63 ± 0.49 pts.) was significantly higher than that of benign nodules (0.04 ± 0.2 pts.), $p < 0.001$. Distribution of thyroid nodule margin type established during thyroid US is shown in Table 6.

**Table 6. Thyroid nodules – margins**

| **All nodules** | **Benign** | **Malignant** | |
|---|---|---|---|
| Smooth | 124 (68.9%) | 94 (95.9%) | 30 (36.6%) |
| Lobulated or irregular | 56 (31.1%) | 4 (4.1%) | 52 (63.4%) |

According to ACR TI-RADS, microcalcifications are associated with papillary thyroid cancer, especially when in combination with other suspicious sonographic features [5]. Similar results were found in this study as well – microcalcifications were more frequent among malignant thyroid nodules while absent echogenic foci was found more often among benign nodules, $p < 0.001$. Malignant thyroid nodules were awarded more points (1.35 ± 1.45 pts.) for presense of echogenic foci compared to benign nodules (0.27 ± 0.7 pts.), $p < 0.001$. Distribution of echogenic foci among thyroid nodules established during thyroid US is shown in Table 7.

**Table 7. Thyroid nodules – echogenic foci**

| | **All nodules** | **Benign** | **Malignant** |
|---|---|---|---|
| None or colloid artifacts | 123 (68.3%) | 82 (83.7%) | 41 (50%) |
| Macrocalcifications | 17 (9.5%) | 11 (11.2%) | 6 (7.3%) |
| Microcalcifications | 40 (22.2%) | 5 (5.1%) | 35 (42.7%) |

Points awarded for different sonographic categories: composition, shape, echogenicity, margin and echogenic foci, were added up. Mean total TI-RADS score was significantly higher among malignant thyroid nodules (6.3 ± 2.1 pts.) compared to benign (4.1 ± 1.37 pts.), $p < 0.001$. Depending on total score, TI-RADS Level was determined for all thyroid nodules. Distribution of thyroid nodules‘ TI-RADS Levels and comparison with cancer risk levels presented in a study by Middleton et al [28] are shown in Table 8.

**Table 8. TI-RADS Levels and malignancy risk comparison**

| | **All nodules** | **Benign** | **Malignant** | **Middleton et al cancer risk levels** |
|---|---|---|---|---|
| TR1 | 0 | 0 | 0 | < 2% |
| TR2 | 7 (3.9%) | 6 (3.3%) | 1 (0.6%) | < 2% |
| TR3 | 33 (18.3%) | 27 (15.0%) | 6 (3.3%) | < 5% |
| TR4 | 98 (54.4%) | 61 (33.9%) | 37 (20.6%) | 5-20% |
| TR5 | 42 (23.3%) | 4 (2.2%) | 38 (21.1%) | ≥ 20% |

Thyroid US using 2017 ACR TI-RADS had a high sensitivity of 82.9% and a lower specificity of 69.4% in predicting the risk of malignancy of thyroid nodules. Compared to studies by Tan et al and Cappelli et al with reported sensitivity of 41-93% and specificity of 43-84%, the values found in this study are on the higher end of the interval in both sensitivity and specificity. Comparison of thyroid US sensitivity and specificity is shown in Table 9.

**Table 9. Diagnostic value of thyroid US using TI-RADS**

| | Sensitivity (%) | Specificity (%) |
|---|---|---|
| Tan et al [20] | 41 | 84 |
| Cappelli et al [21] | 93 | 43 |
| Trimboli et al [29] | 81 | 62 |
| Horvath et al [30] | 88 | 49 |
| Stacul et al [22] | 57 | 67 |
| This study | 82.9 | 69.4 |

Thyroid US using TI-RADS was found to be an useful and accurate tool in predicting the risk of malignancy. Area under curve (AUC) was 0.822, $p < 0.001$. Optimal cut-off value was found to be at 5 TI-RADS points (TR4) – the point where both sensitivity and specificity are the highest. ROC curve detailing sensitivity and specificity of Thyroid US using TI-RADS at multiple points is shown in Fig 4.

**Fig 4. Diagnostic value of Thyroid US using TI-RADS – ROC curve**

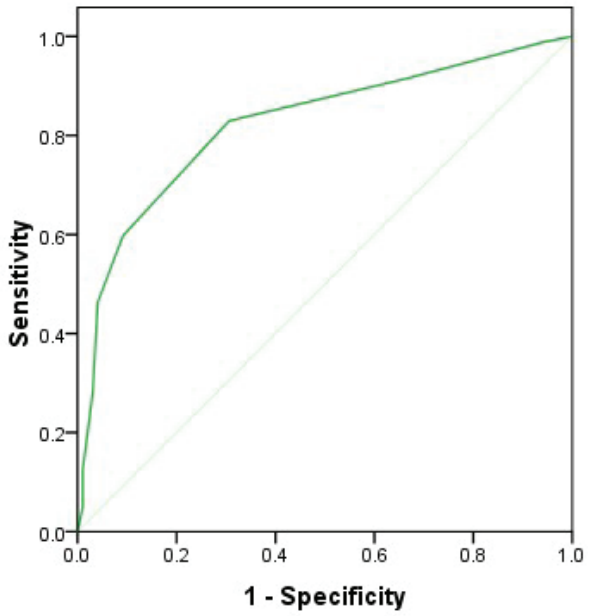


## THYROID ULTRASOUND – VASCULAR PATTERNS

Mixed (both perinodular and intranodular) was the most common (52.2%) type of vascularity. Intranodular flow is generally associated with malignancy [31]. However, as mentioned in a study by Khadra et al [19], no difference in frequency of purely intranodular (weak or intense) vascularity between benign and malignant nodules was found in this study as well. Mixed vascularity was more common among benign ($p = 0.003$) and weak perinodular vascularity was more common among malignant nodules ($p = 0.048$). Distribution of vascular patterns among thyroid nodules established during thyroid Doppler US is shown in Table 10.

Thyroid nodules were awarded less TI-RADS points if the vascularity was of intranodular type – weak and negative correlation was found between total amount of TI-RADS points and vascular patterns ($r_s = -0.238$, $p = 0.001$). This correlation is shown in Fig 5.

Some authors in their studies report good diagnostic value of thyroid nodule vascular patterns in predicting the risk of malignancy: Varverakis et al – sensitivity of 70% and specificity 66% [32], Sultan et al – sensitivity of 90% and specificity 88% [33]. However, in this diagnostic value of thyroid nodule vascular patterns evaluated with Doppler US was found to be low (sensitivity of 40% and specificity of 36.7%) with more likeness to the results of a study by Lyshchik et al where sensitivity was found to be 65.2% and specificity 52.5% [33]. Diagnostic value of thyroid nodule vascular patterns is shown in Table 11.

**Table 10. Thyroid nodules – vascular patterns**

| Vascular patterns | All nodules | Benign | Malignant |
|---|---|---|---|
| Absent | 17 (9.4%) | 4 (4.1%) | 13 (15.9%) |
| Weak perinodular | 63 (35%) | 28 (28.57%) | 35 (42.68%) |
| Intense perinodular | 5 (2.78%) | 4 (4.08%) | 1 (1.21%) |
| Weak intranodular | 1 (0.56%) | 1 (1.02%) | 0 |
| Intense intranodular | 0 | 0 | 0 |
| Mixed | 94 (52.2%) | 61 (62.2%) | 33 (40.2%) |

**Fig 5. Correlation between vascular patterns and TI-RADS score**

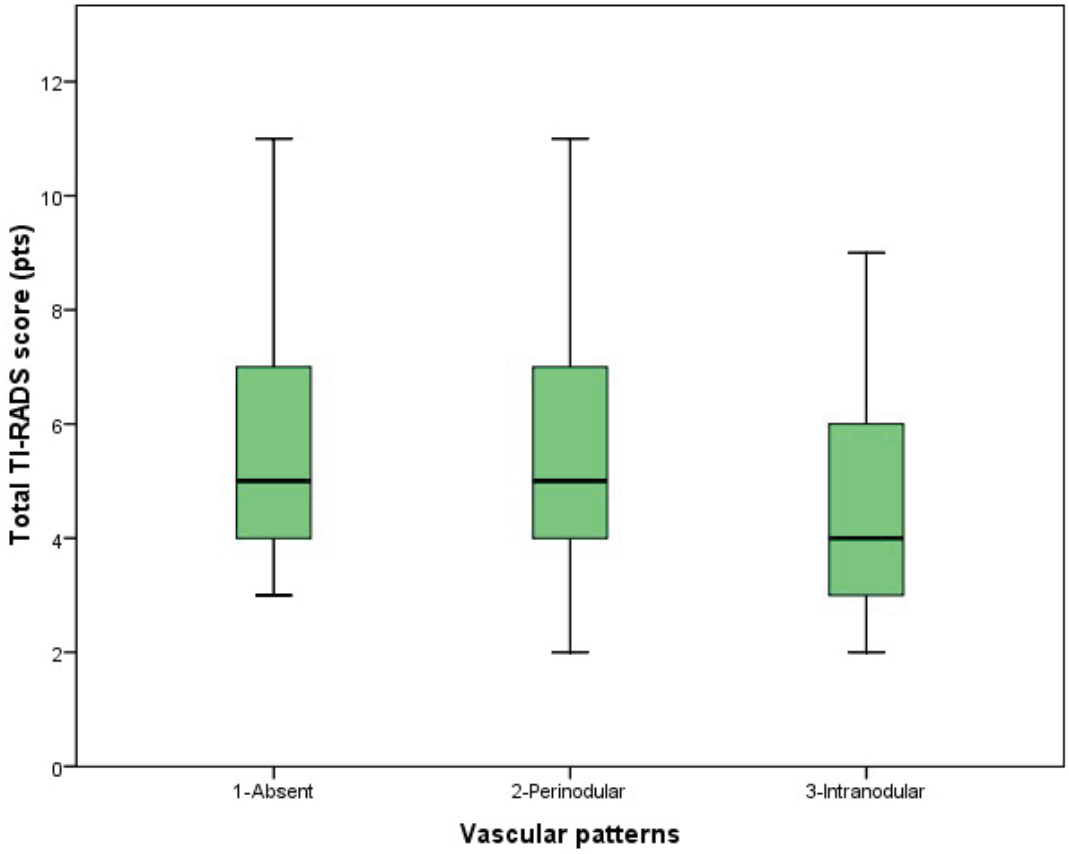


**Table 11. Vascular patterns – diagnostic values in determining risk of malignancy**

| Sensitivity | Specificity | Positive predictive value | Negative predictive value |
|---|---|---|---|
| 40.24% (95% CI 0.296-0.52) | 36.73% (95% CI 0.27-0.47) | 34.74% (95% CI 0.28-0.42) | 42.35% (95% CI 0.35- 0.52) |

## CONCLUSIONS

In our study sonographic features: irregular or lobulated margin, taller-than-wide shape and microcalcifications were found to be more common among malignant thyroid nodules. While thyroid ultrasound using TI-RADS had good diagnostic value in predicting malignancy (sensitivity – 82.9%, specificity – 69.4%), vascular patterns had low sensitivity (40.2%) and specificity (36.7%). Thyroid nodules with intranodular vascularity were found to have a lower TI-RADS score.

## REFERENCES


1. Popoveniuc G, Jonklaas J. Thyroid Nodules. Med Clin North Am. 2012 Mar; 96(2): 329–349.

2. Smith-Bindman R, Lebda P, Feldstein VA, Sellami D, Goldstein RB, Brasic N et al. Risk of thyroid cancer based on thyroid ultrasound imaging characteristics: results of a population-based study. JAMA Intern Med. 2013 Oct 28;173(19):1788-96.

3. Muratli A, Erdogan N, Sevim S, Unal I, Akyuz S. Diagnostic efficacy and importance of fine-needle aspiration cytology of thyroid nodules. J Cytol. 2014 Apr-Jun; 31(2): 73–78.

4. Vaccarella S, Franceschi S, Bray F, Wild CP, Plummer M, Dal Maso L. Worldwide Thyroid-Cancer Epidemic? The Increasing Impact of Overdiagnosis. N Engl J Med. 2016 Aug 18;375(7):614-7.

5. Tessler FN, Middleton WD, Grant EG, Hoang JK, Berland LL, Teefey SA et al. ACR Thyroid Imaging, Reporting and Data System (TI-RADS): White Paper of the ACR TI-RADS Committee. J Am Coll Radiol. 2017 May;14(5):587-595.

6. American Thyroid Association (ATA) Guidelines Taskforce on Thyroid Nodules and Differentiated Thyroid Cancer., Cooper DS, Doherty GM, Haugen BR, Kloos RT, Lee SL, et al. Revised American Thyroid Association management guidelines for patients with thyroid nodules and differentiated thyroid cancer. Thyroid. 2009 Nov; 19(11):1167-214.

7. Guth S, Theune U, Aberle J, Galach A, Bamberger CM. Very high prevalence of thyroid nodules detected by high frequency (13 MHz) ultrasound examination. Eur J Clin Invest. 2009 Aug;39(8):699-706.

8. Singer PA, Cooper DS, Daniels GH, Ladenson PW, Greenspan FS, Levy EG, et al. Treatment guidelines for patients with thyroid nodules and well-differentiated thyroid cancer. American Thyroid Association. Arch Intern Med. 1996 Oct 28; 156(19):2165-72.

9. Mazzaferri EL. Management of a solitary thyroid nodule. N Engl J Med. 1993 Feb 25; 328(8):553-9.

10. Yassa L, Cibas ES, Benson CB, Frates MC, Doubilet PM, Gawande AA, et al. Long-term assessment of a multidisciplinary approach to thyroid nodule diagnostic evaluation. Cancer 2007;111:508-16.

11. Siegel R, Naishadham D, Jemal A. Cancer statistics, 2012. CA Cancer J Clin 2012;62:10-29.

12. Singh Ospina N, Brito JP, Maraka S, Espinosa de Ycaza AE, Rodriguez-Gutierrez R, Gionfriddo MR et al. Diagnostic accuracy of ultrasound-guided fine needle aspiration biopsy for thyroid malignancy: systematic review and meta-analysis. Endocrine. 2016 Sep;53(3):651-61.

13. Shah JP. Thyroid Carcinoma: Epidemiology, Histology, and Diagnosis. Clin Adv Hematol Oncol. 2015 Apr; 13(4 Suppl 4): 3–6.

14. Gharib H, Papini E, Valcavi R, Baskin HJ, Crescenzi A, Dottorini ME, et al. American Association of Clinical Endocrinologists and Associazione Medici Endocrinologi medical guidelines for clinical practice for the diagnosis and management of thyroid nodules. Endocr Pract. 2006 Jan-Feb; 12(1):63-102.

15. Chaudhary V, Bano S. Thyroid ultrasound. Indian J Endocrinol Metab. 2013 Mar-Apr; 17(2): 219–227.

16. Papini E, Guglielmi R, Bianchini A, Crescenzi A, Taccogna S, Nardi F, et al. Risk of malignancy in nonpalpable thyroid nodules: predictive value of ultrasound and color-Doppler features. J Clin Endocrinol Metab. 2002 May; 87(5):1941-6.

17. Hong YJ, Son EJ, Kim EK, Kwak JY, Hong SW, Chang HS. Positive predictive values of sonographic features of solid thyroid nodule. Clin Imaging. 2010 Mar-Apr; 34(2):127-33.

18. Moon WJ, Jung SL, Lee JH, Na DG, Baek JH, Lee YH, et al. Benign and malignant thyroid nodules: US differentiation--multicenter retrospective study. Radiology. 2008 Jun; 247(3):762-70.

19. Khadra H, Bakeer M, Hauch A, Hu T, Kandil E. Is vascular flow a predictor of malignant thyroid nodules? A meta-analysis. Gland Surg. 2016 Dec; 5(6): 576–582.

20. Tan WJ, Sanghvi K, Liau KH, Low CH. An audit study of the sensitivity and specificity of ultrasound, fine needle aspiration cytology and frozen section in the evaluation of thyroid malignancies in a tertiary institution. Ann Acad Med Singapore. 2010 May;39(5):359-62.

21. Cappelli C, Castellano M, Pirola I, Cumetti D, Agosti B, Gandossi E et al. The predictive value of ultrasound findings in the management of thyroid nodules. QJM. 2007 Jan;100(1):29-35. Epub 2006 Dec 17.

22. Stacul F, Bertolotto M, De Gobbis F, Calderan L, Cioffi V, Romano A et al. US, colour-Doppler US and fine-needle aspiration biopsy in the diagnosis of thyroid nodules. Radiol Med. 2007 Aug;112(5):751-62.

23. Frates MC, Benson CB, Doubilet PM, Kunreuther E, Contreras M, Cibas ES, et al. Prevalence and distribution of carcinoma in patients with solitary and multiple thyroid nodules on sonography. J Clin Endocrinol Metab. 2006 Sep;91(9):3411-7.

24. Ball DW. Medullary Thyroid Cancer: Monitoring and Therapy. Endocrinol Metab Clin North Am. 2007 Sep; 36(3): 823–VIII.

25. Cavallo A, Johnson DN, White MG, Siddiqui S, Antic T, Mathew M, et al. Thyroid Nodule Size at Ultrasound as a Predictor of Malignancy and Final Pathologic Size. Thyroid. 2017 May;27(5):641-650.

26. Anil G, Hegde A, Chong FHV. Thyroid nodules: risk stratification for malignancy with ultrasound and guided biopsy. Cancer Imaging. 2011; 11(1): 209–223.

27. Kwak JY, Han KH, Yoon JH, Moon HJ, Son EJ, Park SH, et al. Thyroid imaging reporting and data system for US features of nodules: a step in establishing better stratification of cancer risk. Radiology. 2011 Sep;260(3):892-9.

28. Middleton WD, Teefey SA, Reading CC, Langer JE, Beland MD, Szabunio MM, et al. Multiinstitutional Analysis of Thyroid Nodule Risk Stratification Using the American College of Radiology Thyroid Imaging Reporting and Data System. AJR Am J Roentgenol. 2017 Jun;208(6):1331-1341.

29. Trimboli P, Guglielmi R, Monti S, Misischi I, Graziano F, Nasrollah N, et al. Ultrasound sensitivity for thyroid malignancy is increased by real-time elastography: a prospective multicenter study. J Clin Endocrinol Metab. 2012 Dec;97(12):4524-30.

30. Horvath E, Majlis S, Rossi R, Franco C, Niedmann JP, Castro A, et al. An ultrasonogram reporting system for thyroid nodules stratifying cancer risk for clinical management. J Clin Endocrinol Metab. 2009 May;94(5):1748-51.

31. Wong KT, Ahuja AT. Ultrasound of thyroid cancer. Cancer Imaging. 2005; 5(1): 157–166.

32. Varverakis E, Neonakis E, Tzardi M, Chrysos E. Role of color Doppler ultrasonography in the preoperative management of cold thyroid nodules. Hormones (Athens). 2007 Jan-Mar;6(1):44-51.

33. Sultan LR, Xiong H, Zafar HM, Schultz SM, Langer JE, Sehgal CM. Vascularity assessment of thyroid nodules by quantitative color Doppler ultrasound. Ultrasound Med Biol. 2015 May;41(5):1287-93.

34. Lyshchik A, Moses R, Barnes SL, Higashi T, Asato R, Miga MI, et al. Quantitative analysis of tumor vascularity in benign and malignant solid thyroid nodules. J Ultrasound Med. 2007 Jun;26(6):837-46.

# CT scan attenuation value measurement as a diagnostic tool for patients with pleural effusions

**Gerta Repečkaitė[1], Rokas Kurtinaitis[1], Laima Dobrovolskienė Md[1], Algidas Basevičius Md[1] Domas Golubickas[1]**

*[1]Department of Radiology of Lithuanian University of Health Sciences Kaunas, Lithuania.*

## ABSTRACT

**Background:** Fluid in the pleural cavity is a common clinical problem with many potential causes. Despite the clinical and radiological findings providing important data about the cause(s) of content in the pleural cavity, tube thoracostomy or diagnostic thoracentesis are still required to relieve the pressure and characterize the fluid. These procedures could be avoided by applying a non-invasive method such as measurement of fluid CT attenuation values (CT - AV).
Aim: To evaluate CT attenuation values as a diagnostic tool to distinguish between hydrothorax, pyothorax and haemothorax.

**Materials and methods:** For this retrospective observational study we reviewed 89 patient medical records and chest CT scans performed between October 2012 and January 2017. Patients with the diagnosis of either haemothorax, pyothorax or hydrothorax were included. CT - AV were measured in three CT scan slices with the highest amount of pleural effusion. We calculated the mean CT - AV for every study participant and evaluated the accuracy to distinguish pleural contents between haemothorax, pyothorax and hydrothorax groups using Receiver Operating Characteristic (ROC).

**Results:** The mean CT - AV of haemothorax were significantly ($P < 0.001$) higher from those of pyothorax and hydrothorax. The pyothorax mean CT - AV were also significantly higher than hydrothorax values ($P = 0.042$). The diagnostic accuracy of CT - AV to distinguish between haemothorax, pyothorax and hydrothorax was statistically significant ($P < 0.001$).

**Conclusion:** CT attenuation values between hydrothorax, pyothorax, and haemothorax are distinguishable.

***Keywords:*** pleural effusions, hemothorax, pyothorax, CT attenuation.

## INTRODUCTION

Pleural fluid is a common clinical problem with many potential causes [1]. The first step in prescribing treatment is to decide whether the pleural fluid is haemothorax, pyothorax (empyema) or hydrothorax (serous pleural effusion) [2,3]. The haemothorax can be classified as either traumatic, originating from blunt or penetrating trauma, or spontaneous, arising from multiple reasons: vascular, connective tissue disorders, haematological disorders, neoplastic and miscellaneous (exostoses, endometriosis) [4,5]. The aetiology of pyothorax is either hospital acquired or community acquired infections [6], including a number of bacterial [7] and fungal [8] infections. Many pathological conditions may attribute to the accumulation of hydrothorax. Malfunction of the heart, liver, pancreas or kidneys; certain medications (amiodarone, methotrexate, nitrofurantoin, phenytoin); pulmonary embolism and even pneumonia may cause transudate and exudate accumulation within the pleural cavity. [9] Malignant pleural effusions are due to pleural tumours or metastases originating from the lung, breast, ovarian or gastric cancer, lymphoma, etc. [10] Other conditions, such as autoimmune diseases (e. g. Sjögren's syndrome, Lupus, etc.) and even environmental factors, such as asbestos exposure, may cause hydrothorax. [11-13]. Such a wide array of pleural effusion etiological factors is one of the many reasons why it is crucial to optimise the methods for determining the type of fluid in the pleural cavity.

Despite the clinical and radiological findings which might provide important evidence about the cause(s) of pleural fluid(s) it might still be necessary to perform tube thoracostomy or diagnostic thoracentesis to relieve the pressure and to characterize the fluid. Even though needle thora-

centesis is less invasive than tube thoracostomy, it still caries small, but significant risks (e. g., the pneumothorax, bleeding (chest wall haematoma and haemothorax), and re - expansion pulmonary oedema) [14]. Pneumothorax occurs in 6% of the procedures and 34.1% of pneumothoraces requires chest tube insertion [15]. These unnecessary complications could be avoided using a non-invasive method such as diagnosing the type of pleural fluid using CT attenuation values (CT - AV). To our knowledge, there are no recent studies addressing this method of differentiating pleural effusions in Lithuania.

The aim of this study is to evaluate CT - AV as a diagnostic tool for distinguishing between hydrothorax, pyothorax or haemothorax.

## METHODS AND MATERIALS

### 2.1. STUDY DESIGN AND SETTING

We performed the retrospective observational study at the largest healthcare institution in Lithuania, annually exceeding 1.3 million outpatient consultations and 95 thousand hospital admissions. Kaunas Regional Biomedical Research Ethics Committee (KRBRE) approved the study protocol and waived an informed consent. In this study, medical health records made between October 2012 and January 2017 are analysed.

### 2.2. PATIENT SELECTION CRITERIA

We reviewed hospital's medical records for patients that underwent chest CT scans for suspected pleural or pulmonary pathology (n = 197) and selected patients with pathological findings in the pleural cavity (n = 113). For this study, patients with pleural effusions (n = 104) were selected and the one's with instances of pneumothorax were excluded. 17 more patients were excluded because they had not undergone any diagnostic studies of the pleural effusions or because the pleural contents were of gastric origin. The 89 enrolled patients were grouped into three categories: haemothorax, pyothorax, and hydrothorax, based on the discharge diagnosis, laboratory results, instrumental tests. The diagnosis of haemothorax was based on pleural fluid appearance or biochemical analysis of the fluid, determining criteria being haematocrit (Hct) > 50%. The confirmation of pleural content being pus required a visually purulent appearance and/or histological assessment of the pleura. We classified the remaining effusions as hydrothorax.

### 2.3. SCANNING PARAMETERS

All CT scans were performed using GE VCT 64 or GE VCT 16 slice CT scanner, following chest scanning protocols: at a slice thickness of 5 mm; pitch 0.969:1; 120 kV, 100 - 665 mA, rotation speed 0.5 s. When indicated and allowed, the intravenous contrast (80 ml. Sol. Ultravist or Visipaque 300) was injected at the speed of 2.5 ml/s. We reviewed all images using Picture Archiving and Communication System (PACS) server Cedara-I-Reach (TM).

### 2.4. DATA ACQUISITION AND STATISTICAL ANALYSIS

For this study, all CT scans were reviewed independently by two medicine students of Lithuanian University of Health Sciences (LSMU), and experienced radiologists: a doctor resident measured the data, and two doctors radiologists re-measured and described the images. Later the images were also reviewed by the thoracic radiology section chief during multidisciplinary team meetings. In every CT scan (before and after intravenous contrast media administration) we located three slices with the largest pleural effusion volume and measured the attenuation values in Hounsfield Units (HU) using the circular or ellipse region of interest (ROI) tool to mark the area containing only the fluid (Figures 1, 2). We situated the ROI so the measurements would not include bone, fat, lung, thickened pleural tissue or air. For statistical analysis, we recorded and used the mean of three attenuation values.

We analysed all data using IBM SPSS Statistics v. 23.0. Normally distributed data was expressed as the mean value (95% confidence intervals) and non-normally distributed data as the median (minimum - maximum values).

The Scheffe method in the one-way analysis of variances (ANOVA) was used to assess the differences of normally distributed attenuation values between haemothorax, pyothorax, and

hydrothorax groups. Using the Receiver Operating Characteristic (ROC) we determined the sensitivity and specificity of CT attenuation value measurement as a diagnostic tool for all three groups. The Youden' s J statistic was applied to determine the cut-off values for all three groups. We evaluated group homogeneity using 2, one-way ANOVA and Kruskal-Wallis tests. Values of P less than 0.05 were considered significant.

## RESULTS

The study population consisted of 89 patients: 69 (77.5%) were men and 20 (22.5%) women. 12 (13.5%) patients had been hospitalized within 24 hours and 77 (86.5%) within 6 hours after the onset of symptoms.

There were no significant age (P = 0.285), gender (P = 0.509), hospitalisation length (P = 0.503) differences between the pleural effusion (haemothorax, pyothorax, or hydrothorax) groups. (Table 1). The mean CT - AV of haemothorax were significantly (P < 0.001) different from those of pyothorax, and hydrothorax. The pyothorax mean attenuation values were also significantly higher than hydrothorax values (P = 0.042) (Figure 3).

We used the area under the ROC curve (AUC) to determine the accuracy of the mean CT - AV to differentiate between haemothorax, pyothorax, and hydrothorax (Table 2). All results were statistically significant (P < 0.001) (Figure 4, 5, 6). The cut-off values were determined as follows: to distinguish haemothorax from pyothorax ≥ 24.52 HU (SE: 83.3%; SP: 90.1%); haemothorax from hydrothorax ≥ 20.17 HU (SE: 90%; SP: 100%); pyothorax from hydrothorax ≥ 15.3 HU (SE: 65.6%; SP: 88.9%).

**Table 1. Demographic and pleural content CT attenuation findings in patients with haemothorax, pyothorax, and hydrothorax.**

| | Haemothorax | Pyothorax | Hydrothorax |
|---|---|---|---|
| Count | 30 (33.7%) | 32 (36.0%) | 27 (30.3%) |
| Age | 58.57 (51.82 - 65.31) | 52.41 (47.55 - 57.26) | 52.81 (45.48 - 60.15) |
| Gender | | | |
| Male | 22 | 27 | 20 |
| Female | 8 | 5 | 7 |
| Length of hospitalization (days) | 20.5 (2 - 147) | 25 (3 - 108) | 17 (2 - 73) |
| CT attenuation value (HU) | 33.85 (29.43 - 38.27) | 17.29 (15.1 - 19.47) | 11.92 (10.54 - 13.3) |

**Table 2. ROC curve results, assessing the use of CT attenuation values to distinguish between haemothorax, pyothorax, and hydrothorax.**

| | Area under the ROC curve | 95% CI |
|---|---|---|
| ROC (Haemothorax - Pyothorax) | 0.912 | 0.841 - 0.984 |
| ROC (Haemothorax - Hydrothorax) | 0.993 | 0.981 - 1.000 |
| ROC (Pyothorax - Hydrothorax) | 0.774 | 0.645 - 0.895 |
| | | |

**Figure 1. 73-year-old patient after thoracic trauma with suspected haemothorax. CT scan shows bilateral dorsal pleural effusion. Ellipse ROI tool shows the mean attenuation value of 34 - 49 HU.**

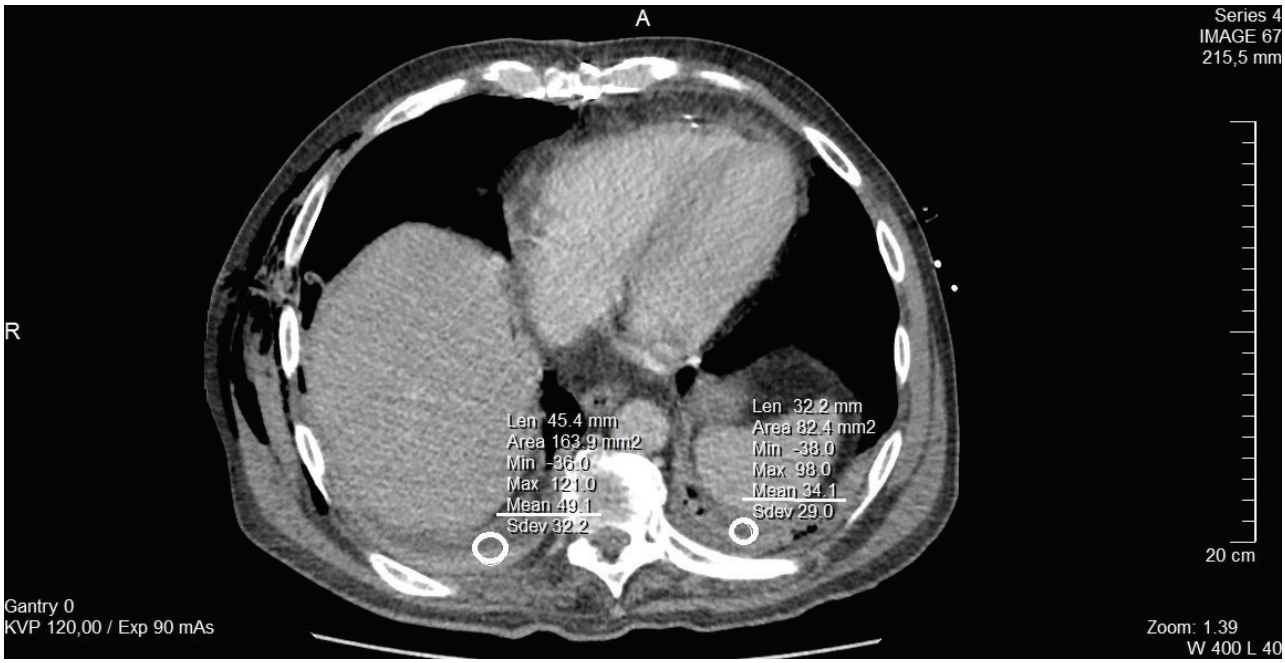


**Figure 2. 44 year old patient with fewer, pyothorax and empyema. CT scan shows separated lateral pleural effusions with multiple gaseous bubbles. Ellipse ROI tool shows the mean attenuation value of 19.5 - 20.2 HU.**

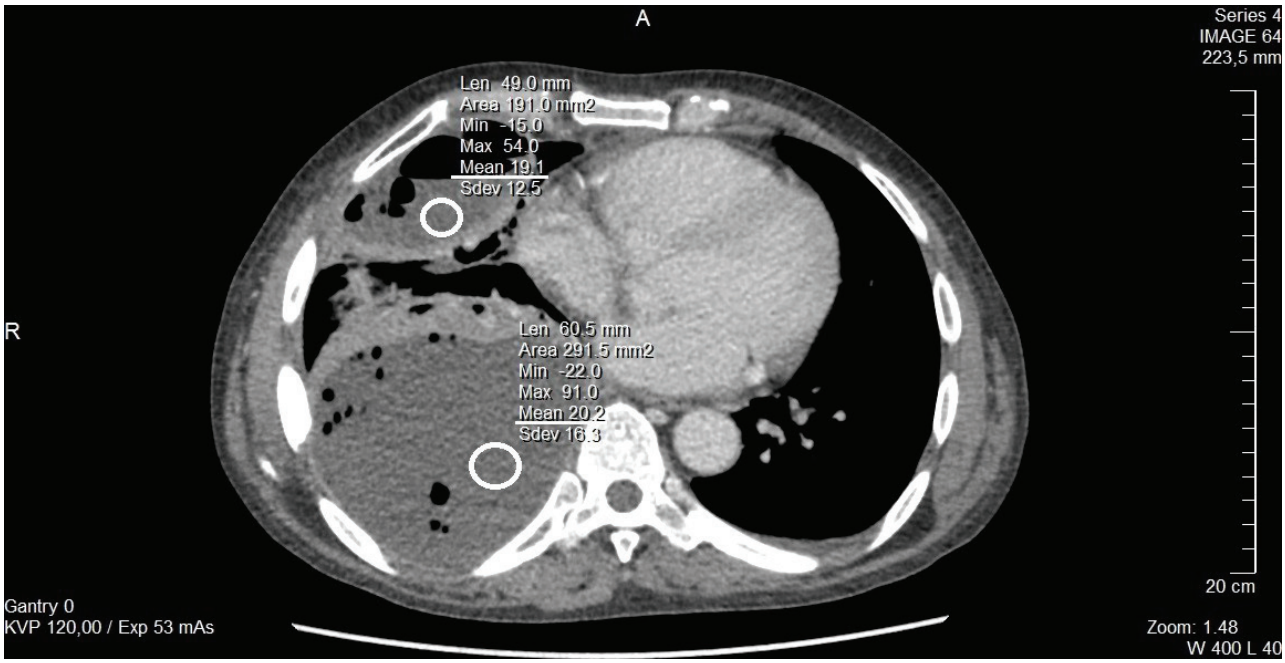

**Figure 3. Box and whisker plots demonstrating mean attenuation value in haemothorax, hydrothorax, and pyothorax groups.**

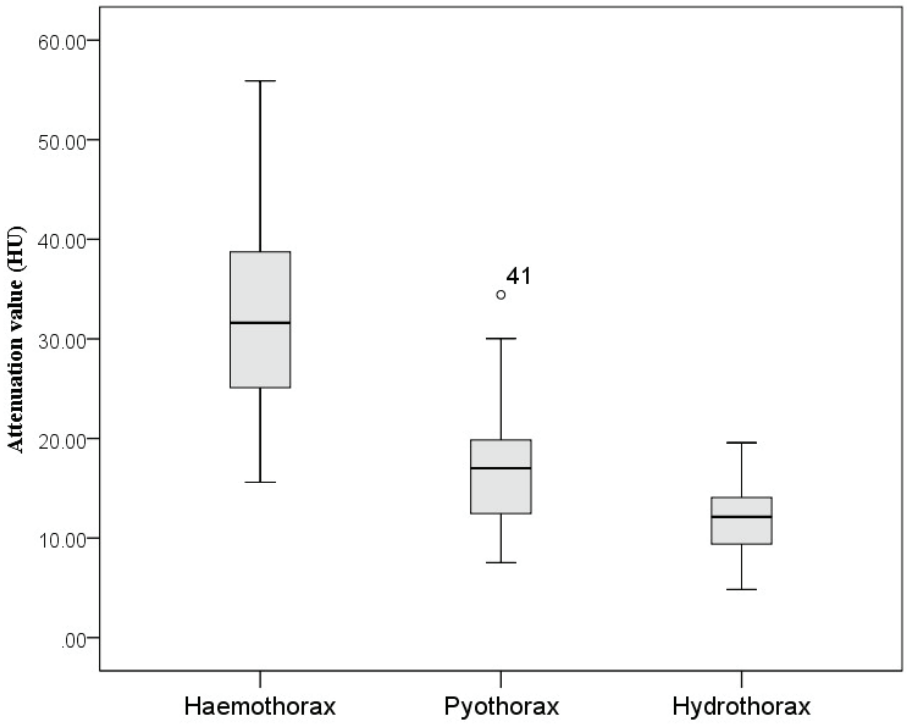


**Figure 4. ROC demonstrating excellent diagnostic accuracy differentiating haemothorax from pyothorax using CT attenuation values. (P < 0.001)**

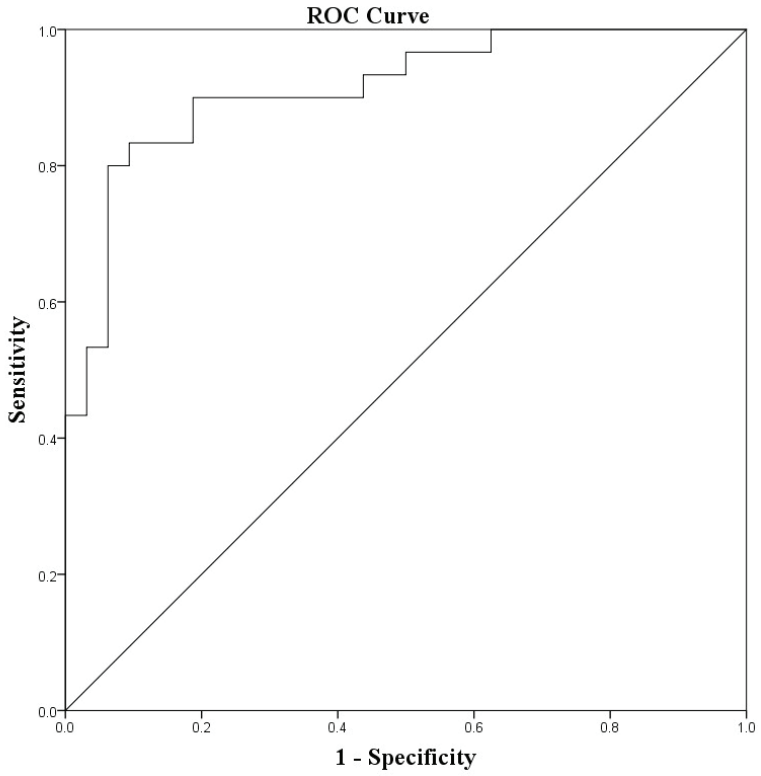

**Figure 5. ROC demonstrating excellent diagnostic accuracy differentiating haemothorax from hydrothorax using CT attenuation values. (P < 0.001)**

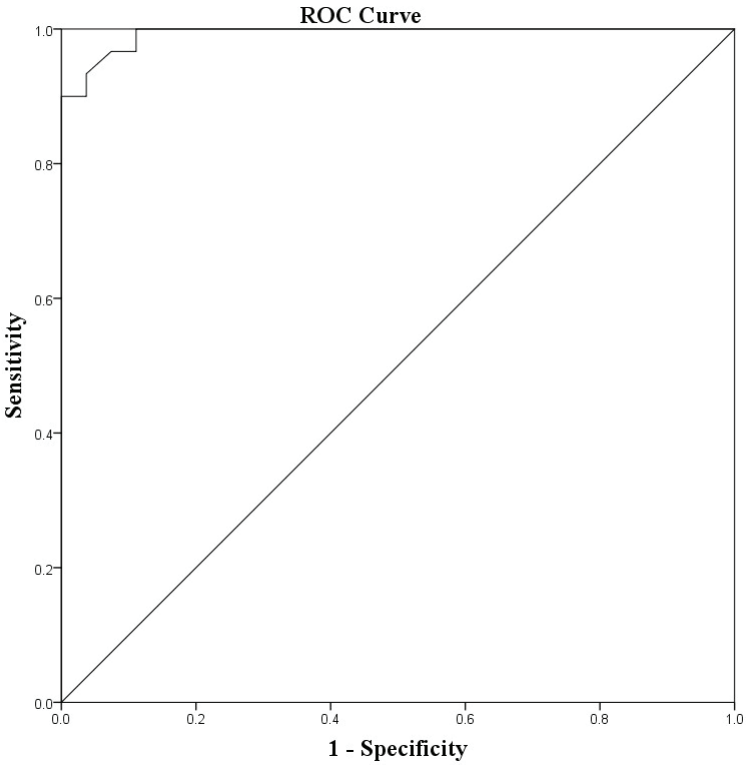


**Figure 6. ROC demonstrating fair diagnostic accuracy differentiating hydrothorax from pyothorax using CT attenuation values. (P < 0.001)**

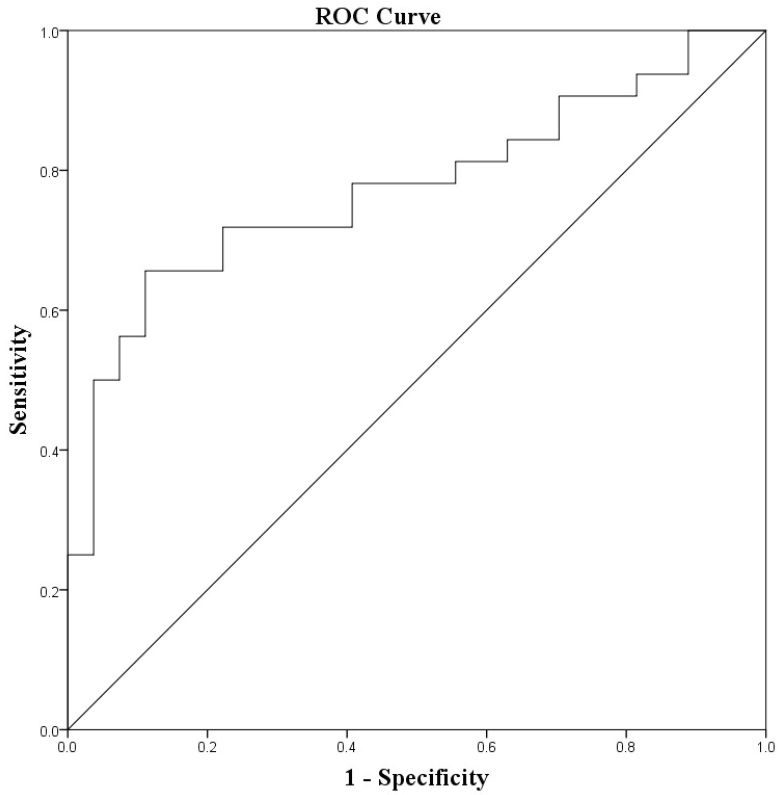

## DISCUSSION

The differential diagnosis to distinguish between haemothorax, pyothorax and hydrothorax in a clinical setting is usually achieved using fluid analysis by means of diagnostic thoracentesis, thoracostomy or pleural biopsy and histological examination [3]. In this study, we found that CT - AV is a relatively accurate measurement to determine the nature of the pleural fluid. In previous studies, researchers have discovered that CT - AV was useful to differentiate even transudates from exudates in patients with pleural effusions [16, 17]. However, more data is required because of the overlapping HU values as they decrease the sensitivity of the diagnostic method.

We predicted that haemothorax would have higher CT - AV than pyothorax and hydrothorax because, in the acute phase, extravasated blood usually has a higher HU value. Iron in the haemoglobin molecule increases tissue density more than protein does in pyothorax and hydrothorax [18]. In most cases, the blood comes from damaged vessels in the ribs, lungs, mediastinum, diaphragm, chest wall, or directly from ruptured great vessels. [19]. Pyothorax should also have higher CT - AV than hydrothorax due to the strands of fibrin, high levels of protein, bilirubin, and LDH contained in the purulent fluid, all of which increase attenuation on a CT scan [14, 20].

To our knowledge, only one study has compared CT - AV between haemothorax, empyema, and pleural effusion. Liu et al. [19] examined 189 patients and found that the cut-off value >15,6 HU to distinguish haemothorax from pleural effusion and a cut-off value of ≥15.9 HU to distinguish haemothorax from empyema.

In our study we found that the cut-off value of ≥ 24.52 HU (SE: 83.3%; SP: 90.6%) and ≥ 20.17 HU (SE: 90%; SP: 100%) was excellent to distinguish accordingly haemothorax from pyothorax and hydrothorax, while a cut-off value of ≥ 15.3 HU (SE: 65.6%; SP: 88.9%) to differentiate pyothorax from hydrothorax. However, the cut-off values are significantly higher than those, determined in the study performed by Liu et al.[19] This means further studies to establish the optimal cut-off values are necessary.

To sum up, CT - AV could be useful in emergency diagnostics and treatment for patients with contraindications for diagnostic thoracentesis such as hemorrhagic diathesis and cutaneous conditions (e.g., pyoderma or herpes zoster infection) [21]. Although CT is more sensitive than conventional chest sonography and radiography in differentiating between different pleural effusions [20], the value of diagnostic thoracentesis in normal clinical practice remains irreplaceable. The overlapping CT - AV decrease the applicability of this method and should not replace thoracentesis and/or tube thoracostomy as a diagnostic method to distinguish between haemothorax, pyothorax, and hydrothorax, especially when the latter are indicated for decompression or specific diagnostic tests.

## REFERENCES

1. Porcel JM, Esquerda A, Vives M, Bielsa S. Etiology of pleural effusions: analysis of more than 3,000 consecutive thoracenteses. Arch Bronconeumol 2014; 50 (5): 161-165.

2. Light RW. Management of pleural effusions. J Formos Med Assoc 2000; 99(7): 523-531.

3. Akulian J, Feller-Kopman D. The past, current and future of diagnosis and management of pleural disease. J Thorac Dis 2015 Dec; 7(Suppl 4): S329-38.

4. Broderick SR. Hemothorax: Etiology, diagnosis, and management. Thorac Surg Clin 2013; 23: 89–96.

5. Janik M, Straka L, Krajcovic J, Hejna P, Hamzik J, Novomesky F. Non-traumatic and spontaneous hemothorax in the setting of forensic medical examination: A systematic literature survey. Forensic science international 2014; 236: 22–9.

6. Zablockis R, Petruškevičienė R, Nargėla RV. Pleuros empiemos ir komplikuoto parapneumoninio pleurito priežastys ir rizikos veiksniai. Medicina 2010; 46(2): 113–119.

7. Dass R, Deka NM, Barman H, Duwarah SG, Khyriem AB, Saikia MK, Hoque R, Mili D. Empyema thoracis: analysis of 150 cases from a tertiary care centre in North East India. Ind J Pediatr 2011; 78: 1371–1377.

8. Nigo M, Vial MR, Munita JM, Jiang Y, Tarrand J, Jimenez CA, Kontoyiannis DP. Fungal empyema thoracis in cancer patients. J Infection 2016; 72(5): 615-621

9. McGrath EE, Anderson PB. Diagnosis of pleural effusion: a systematic approach. Am J Crit Care 2011; 20(2): 119–127.

10. Egan AM, McPhillips D, Sarkar S, Breen DP. Malignant pleural effusion. QJM 2014; 107: 179-84.

11. Ma D, Lu H, Qu Y, Wang S, Ying Y, Xiao W. Primary Sjogren's syndrome accompanied by pleural effusion: a case report and literature review. Int J Clin Exp Pathol 2015; 8: 15322–15327.

12. Gulhane S, Gangane N. Detection of lupus erythematosus cells in pleural effusion: an unusual presentation of systemic lupus erythematosus. J Cytol 2012; 29:77-79.

13. Robinson BW, Musk AW. Benign asbestos pleural effusion: diagnosis and course. Thorax. 1981 Dec; 36(12): 896–900.

14. Cantey EP, Walter JM, Corbridge T, Barsuk JH. Complications of thoracentesis: Incidence, risk factors, and strategies for prevention. Curr Opin Pulm Med 2016; 22: 378–85.

15. Gordon CE, Feller-Kopman D, Balk EM, Smetana GW: Pneumothorax following thoracentesis: a systematic review and meta-analysis. Arch Intern Med 2010; 170: 332-339.

16. Abramowitz Y, Simanovsky N, Goldstein MS, Hiller N. Pleural effusion: characterization with CT attenuation values and CT appearance. Am J Roentgenol 2009; 192: 618-623.

17. Cullu N, Kalemci S, Karakas O, Eser I, Yalcin F, Boyaci FN, Karakas E. Efficacy of CT in diagnosis of transudates and exudates in patients with pleural effusion. Diagn Interv Radiol 2014; 20: 116-120.

18. Parizel PM, Makkat S, Van Miert E, Van Goethem JW, van den Hauwe L, De Schepper AM. Intracranial hemorrhage: principles of CT and MRI interpretation. Eur Radiol 2001; 11: 1770-1783.

19. Liu F, Huang YC, Ng YB, Liang JH. Differentiate pleural effusion from hemothorax after blunt chest trauma; comparison of computed tomography attenuation values. J Acute Med 2016; 6(1): 1-6.

20. Helm EJ, Matin TN, Gleeson FV. Imaging of the pleura. J Magn Reson Imaging 2010; 32: 1275–1286.

21. Na M J. Diagnostic tools of pleural effusion. Tuberc Respir Dis 2014; 76(5): 199-210.

# Preoperative assessment of pancreatic adenocarcinoma. Value of CT imaging

**Inga Zaboriene[1], Tomas Tvarijonas[2], Gertruda Rudaityte[2] , Saulius Lukosevicius[1], Giedrius Barauskas[3], Kristina Zviniene[1]**

*[1]Department of Radiology, Lithuanian University of Health Sciences Kaunas, Lithuania.*
*[2]Lithuanian University of Health Sciences Kaunas, Lithuania.*
*[3]Lithuanian University of Health Sciences, Medical Academy. Department of Surgery.*

## ABSTRACT

**Background and aim**

Pancreatic adenocarcinoma is one of the most malignant cancer forms. It is fourth most common cause of cancer death worldwide, with a poor overall 5-year survival rate of only 4 %. The treatment depends upon tumour resectability at presentation. Therefore, radiological imaging is crucial in the management of the disease. In this study we evaluated the role of computed tomography in diagnosing pancreatic adenocarcinoma and CT diagnostic values in determining resectability of pancreatic.

**Matherial and methods.** This was a prospective randomized clinical study, in which 79 patients with resectable pancreatic cancer were studied. All the pacients underwent MDCT scan. In all CT images we analyzed location of pancreatic tumor, invasion into adjacent structures, vascular involvement and distant metastases. The results of preoperative CT staging were compared to the postoperative histological data. In order to determine diagnostic values of CT, we calculated the sensitivity, specificity, positive and negative prognostic values (PPV, NPV) as well, as accuracy. All calculations were performed using SPSS for Windows 25.0 software and Microsoft Excel 16.

**Results.** There was no difference in evaluating T stage pre and postoperatively X2 =74,452, df 15, p<0,001 and no statistically difference in evaluating tumor N stage pre- and postoperatively X2=8,978, df=1, p=0,003.

Overall CT sensitivity for tumor T stage was 73 %, specificity 85 %, PPV and NPV 67.1 % and 88.2 % respectively, accuracy 81.4 %. CT diagnostic values for N stage: sensitivity 75 %, specificity 59.3 %, PPV 78%, NPV 55.2% and accuracy 69.6%.

**Conclusions**

- CT is specific and accurate imaging modality in T stage of pancreatic adenocarcinoma.
- CT is quite sensitive, but non specific in N stage of pancreatic adenocarcinoma.

***Keywords:*** pancreatic adenocarcinoma, resectability, CT values

## INTRODUCTION

Pancreatic adenocarcinoma is one of the most malignant cancer forms. It is fourth most common cause of cancer death worldwide. Globally, about 338000 people had pancreatic cancer in 2012, making it the 11th most common cancer. The highest incidence and mortality rates of pancreatic cancer is found in developed countries. Prognosis of this cancer remains bad – 5 year survival rate is less than 5 percent. The incidence and mortality of pancreatic cancer worldwide correlated with increasing age and was slightly more common in men than in women [1,3]. Pancreatic cancer is diagnosed late in the natural history of the disease, given the few early indicators of illness, and the lack of screening tests for this disease [2]. In fact, 40% of the pancreatic cancer cases are diagnosed in late stages, when the disease has already spread far from the primary cancerous process, where as another 40% of the patients are diagnosed with locally advanced pancreatic cancer.

Early and precise diagnostics and grading are very important for further treatment and prognosis of patients. When the lesion of the pancreas is suspected, the first line diagnostic modality is computed tomography (CT). If any uncertainties occur, the following test after CT is usually magnetic resonance imaging (MRI) [2-4]. Lately, MDCT (multidetector computed tomography) became golden standard for preoperative evaluation and grading, as well as, treatment choice and observation of the pancreatic adenocarcinoma. However, when using CT as a diagnostic test, approximately 11% of the ductal adenocarcinoma‘s are missed, because density of parenchyma of the pancreas and cancerous tissue are the

same, as well as differential diagnosis between paraduodenal space pancreatitis and pancreatic cancer is complicated [4]. Moreover, it is complicated to diagnose pancreatic adenocarcinoma in the presence of chronic focal pancreatitis. In the cases mentioned above, computed tomography with perfussion and MRI are diagnostic tests of the first choice.

In this study we evaluated the role of computed tomography in diagnosing pancreatic adenocarcinoma and CT diagnostic values in determining pancreatic adenocarcinoma‘s resectability.

## AIM

To evaluate CT diagnostic values in determining pancreatic adenocarcinoma‘s resectability.

## OBJECTIVES

1. To identify CT diagnostic values in determining the local extention of pancreatic adenocarcinoma (T stage).
2. To calculate CT diagnostic values in determining the spreading of pancreatic adenocarcinoma into regional lymph nodes (N stage).

## MATHERIALS AND METHODS

This was a prospective randomized clinical study, in which 79 patients with resectable pancreatic cancer were studied.

**Inclusion criteria:**
1. Older than 18 year old patients with radiologically confirmed pancreatic adenocarcinoma

**Exclusion criteria:**
1. Patients with renal disfunction;
2. Sensitivity to iodine.
3. Refusal to participate in the study.
4. Distant metastases.

Patients were treated in clinics of surgery and gastroenterology between June year 2015 – september Year 2018. (TLK-10, C25.9). All the patients gave their written informed consent, and The Kaunas Regional Biomedical Research Ethics Committee approved the study (protocol Nr. BE-10-5, 2015 05 13 ).

All the patients underwent MDCT scan, using „GE light Speed Pro“ 64 CT scanner.

Native and contrast-enhanced scans were performed with non-ionic intravenous contrast, injecting 100ml of contrast media at high speed (3,5 ml/s). Arterial and venous phases were performed in 30s and 70s after the start of contrast injection, following the standard protocol, used for pancreatic imaging. If any focal liver lesions were found – late phase (after 10 minutes) was performed in order to identify the nature of those focal lesions. Axial CT images and MPR reconstructions were analysed.

According to NCCN (National Comprehensive Cancer Network) guidelines, it is recommended to use CT or MRI for grading. Decision, whether to use CT or MRI should depend on possibilities, accessibility, local practice and local experience.

Preoperative assessment is essential in identifying resectable disease, borderline resectable disease, locally advanced disease (unresectable without distant metastases) and metastatic disease (unresectable).

In our study we used NCCN guidelines version 3.2017 (pancreatic adenocarcinoma), for evaluation of resectability of the pancreatic tumor (Table 1).

During analysis of the CT images, we evaluated

**Table 1. NCCN Guidelines Version 3.2017 pancreatic adenocarcinoma [15].**

| **Arterial Evaluation** | | |
|---|---|---|
| **SMA Contact** | **Present** | **Absent** |
| Degree of solid soft-tissue contact | ≤180 | >180 |
| Degree of increased hazy attenuation/stranding contact | ≤180 | >180 |
| Focal vessel narrowing or contour irregularity | Present | Absent |
| Extension to first SMA branch | Present | Absent |
| **Celiac Axis Contact** | **Present** | **Absent** |
| Degree of solid soft-tissue contact | ≤180 | >180 |
| Degree of increased hazy attenuation/stranding contact | ≤180 | >180 |
| Focal vessel narrowing or contour irregularity | Present | Absent |

| CHA Contact | Present | Absent |
|---|---|---|
| Degree of solid soft-tissue contact | ≤180 | >180 |
| Degree of increased hazy attenuation / stranding contact | ≤180 | >180 |
| Focal vessel narrowing or contour irregularity | Present | Absent |
| Extension to celiac axis | Present | Absent |
| Extension to bifurcation of right/left hepatic artery | Present | Absent |

## Venous Evaluation

| MPV Contact | Present | Absent | Complete occlusion |
|---|---|---|---|
| Degree of solid soft-tissue contact | ≤180 | >180 | |
| Degree of increased hazy attenuation / stranding contact | ≤180 | >180 | |
| Focal vessel narrowing or contour irregularity (tethering or tear drop) | Present | Absent | |

| SMV Contact | Present | Absent | Complete occlusion |
|---|---|---|---|
| Degree of solid soft-tissue contact | ≤180 | >180 | |
| Degree of increased hazy attenuation / stranding contact | ≤180 | >180 | |
| Focal vessel narrowing or contour irregularity (tethering or tear drop) | Present | Absent | |
| Extension | Present | Absent | |

## Arterial Evaluation

| SMA Contact | Present | Absent |
|---|---|---|
| Degree of solid soft-tissue contact | ≤180 | >180 |
| Degree of increased hazy attenuation/stranding contact | ≤180 | >180 |
| Focal vessel narrowing or contour irregularity | Present | Absent |
| Extension to first SMA branch | Present | Absent |

| Celiac Axis Contact | Present | Absent |
|---|---|---|
| Degree of solid soft-tissue contact | ≤180 | >180 |
| Degree of increased hazy attenuation/stranding contact | ≤180 | >180 |
| Focal vessel narrowing or contour irregularity | Present | Absent |

| CHA Contact | Present | Absent |
|---|---|---|
| Degree of solid soft-tissue contact | ≤180 | >180 |
| Degree of increased hazy attenuation/stranding contact | ≤180 | >180 |
| Focal vessel narrowing or contour irregularity | Present | Absent |
| Extension to celiac axis | Present | Absent |
| Extension to bifurcation of right/left hepatic artery | Present | Absent |

## Venous Evaluation

| MPV Contact | Present | Absent | Complete occlusion |
|---|---|---|---|
| Degree of solid soft-tissue contact | ≤180 | >180 | |
| Degree of increased hazy attenuation/ stranding contact | ≤180 | >180 | |
| Focal vessel narrowing or contour irregularity (tethering or tear drop) | Present | Absent | |

| | | | |
|---|---|---|---|
| **SMV Contact** | **Present** | **Absent** | **Complete occlusion** |
| Degree of solid soft-tissue contact | ≤180 | >180 | |
| Degree of increased hazy attenuation/ stranding contact | ≤180 | >180 | |
| Focal vessel narrowing or contour irregularity(tethering or tear drop) | Present | Absent | |
| Extension | Present | Absent | |
| **Other** | | | |
| **Thrombus within vein (tumor, bland)** | **Present:**<br>MPV<br>SMV<br>SplenicVein | **Absent** | |
| **Venous collaterals** | **Present:**<br>Around pancreatic head<br>Porta hepatis<br>Root of the mesentery<br>Left upper quadrant | **Absent** | |

* SMA – superior mesenteric artery, CHA – common hepatic artery, MPV – main portal vein, SMV – superior mesenteric vein

homogenicity of the tumor, density of cancerous tissue in comparison with normal pancreatic parenchyma, relation with the surrounding vessels. For extrapancreatic evaluation we looked for distant liver metastases, peritoneal and omental nodules, ascites, suspicious lymph nodes and other extrapancreatic disease (invasion of adjacent structures).

After preoperative radiological evaluation, all the patients underwent radical surgical treatment with further histopathological examination of obtained specimens. The results of CT scans were compared with results of surgery and histopathological examination. Pathologic TNM staging system of pancreatic cancer in the 8th edition of UICC cancer staging system is presented in Table 2.

**Table 2 . TNM staging of pancreatic cancer (7th edition of the AJCC (The American Joint Committee on Cancer) stage system) [16].**

| CLINICAL | STAGE CATEGORY DEFINITIONS | PATHOLOGIC |
|---|---|---|
| Extent of disease before any treatment | | Extent of disease through completion of definitive surgery |
| y clinical – staging completed after neoadjuvant therapy but before subsequent surgery | | y pathologic – staging completed after neoadjuvant therapy AND subsequent surgery |

| | | |
|---|---|---|
| | **PRIMARY TUMOR (T)** | |
| Tx | Primary tumor cannot be assessed | Tx |
| T0 | No evidence of primary tumor | T0 |
| Tis | Carcinoma in situ* | Tis |
| T1 | Tumor limited to the pancreas, 2cm or less in greatest dimension | T1 |
| T2 | Tumor limited to the pancreas, more than 2 cm in greatest dimension | T2 |
| T3 | Tumor extends beyond the pancreas but without involvement of the celiac axis or the superior mesenteric artery | T3 |
| T4 | Tumor involves the celiac axis or the superior mesenteric artery (unresectable primary tumor) | T4 |
| | **Note: This also includes the "PanInIII" classification* | |
| | **REGIONAL LYMPH NODES (N)** | |
| Nx | Regional lymph nodes cannot be assessed | Nx |
| N0 | No regional lymph node metastasis | N0 |
| N1 | Regional lymph node metastasis | N1 |
| M0 | DISTANT METASTASIS (M) | M1 |
| | No distant metastasis (no pathologic M0; use clinical M to complete stage group | |
| M1 | Distant metastasis | |

| **ANATOMIC STAGE & PROGNOSTIC GROUPS** | | | |
|---|---|---|---|
| | | **CLINICAL** | |
| **GROUP** | T | N | M |
| 0 | Tis | N0 | M0 |
| IA | T1 | N0 | M0 |
| IB | T2 | N0 | M0 |
| IIA | T3 | N0 | M0 |
| IIB | T1 | N1 | M0 |
| | T2 | N1 | M0 |
| III | T3 | N1 | M0 |
| IV | T4 | Any N | M0 |
| Stage unknown | Any T | Any N | M1 |

## STATISTICAL ANALYSIS

Quantitative values were presented as mean values and standard deviation. Chi-square test was performed to evaluate correlation between Qualitative values. Statistically significant value was considered when $p < 0,05$. To determine pancreatic adenocarcinoma's local spreading and resectability, we calculated CT prognostic values. We calculated accuracy, the sensitivity, and specificity of this investigation, as well as positive and negative prognostic values. Calculations were performed using formulas [5]:

*Accuracy of diagnostic method* (percentage) = a + d / a + b + c + d x 100
*Sensitivity of diagnostic method* (percentage) = a / (a +c) x 100
*Specificity of diagnostic method* (percentage) = d / (b + d) x 100
*Positive predictive value* = a / (a + b) x 100
*Negative predictive valu*e (percentage) = d / (c + d) x 100
Where: a – fairly positive cases, b – false positive cases, c – false negative values, d – fairly negative values.

Statistical analysis was performed using IBM SPSS Statistics 25.0 software and Microsoft Excel 16.

## RESULTS

79 patients were enrolled in this study: 33 (41.8%) males and 46 (58.2%) females. Patient's age distribution was normal. There was no significant difference between male and female age.
After CT imaging in 82.3 % of all cases, pancreatic adenocarcinoma was diagnosed at stage T3 and T4 disease and only 17.7 % in stage T1 and T2.
After surgery there were 74,7 % T3 and T4 disease and 20,2 % of T1 and T2 disease. There was no difference in evaluating T stage pre and postoperatively X2 =74,452, df 15, p<0,001. More detailed characterstics of radiological and postoperative staging are presented in Table 3.
Based on CT scan results, stage N1 was the most common (63.3% of all the cases, n=50) and stage N0 was found in 36.7% of the cases (n=29). After surgery stage N1 was found in 52 of all cases (65,8 %) and stage N0 in 27 of all cases (34,2% ). There was no statistically difference in evaluating tumor N stage pre and postoperatively X2=8,978, df=1, p=0,003
Postoperative histological evaluation revealed adenocarcinomas in 76 cases ( 96,2%), 1 case was confirmed as metastases and two cases were proven to be pancreatic inflamatory changes (n=3, 3,8 %)

**Table 3. Radiological and postoperative characteristics of TNM staging of the study.**

| | T radiologically | | | | | T postoperatively | | | | | | |
|---|---|---|---|---|---|---|---|---|---|---|---|---|
| | T1 | T2 | T3 | T4 | Total | T1 | T2 | T3 | T4 | Ca in situ | Non tumor | Total |
| **Frequency** | 3 | 11 | 58 | 7 | 79 | 5 | 11 | 54 | 5 | 1 | 3 | 79 |
| **Percent** | 3.8 | 13.9 | 73.4 | 8.9 | 100 | 6.3 | 13.9 | 68.4 | 6.3 | 1.3 | 3.8 | 100 |

Table 4 shows accuracy, sensitivity, specificity, positive prognostic value (PPV), negative prognostic value (NPV) and accuracy of T and N staging, using MDCT.

**Table 4. Sensitivity, specificity, PPV, NPV and accuracy of T and N staging, using MDCT, of our study.**

| | HISTOLOGICAL STAGING | | | | |
|---|---|---|---|---|---|
| **T stage** | **Sensitivity %** | **Specificity %** | **PPV %** | **NPV %** | **Accuracy %** |
| **CT T1+T2** | 62.5 | 94.4 | 42.9 | 93 | 88.6 |
| **CT T3** | 83.3 | 48 | 77.6 | 57.1 | 72.2 |
| **CT T4** | 60 | 94.6 | 42.9 | 97.2 | 92.4 |
| **T overall** | 73 | 85 | 67.1 | 88.2 | 81.4 |
| **N stage** | **Sensitivity %** | **Specificity %** | **PPV %** | **NPV %** | **Accuracy %** |
| **CT N0** | 59.3 | 75 | 55.2 | 78 | 69.6 |
| **CT N1** | 69.2 | 48.1 | 72 | 44.8 | 62 |
| **N overall** | 75 | 59.3 | 78 | 55.2 | 69.6 |

## DISCUSSION

Detection and accurate staging of pancreatic carcinoma is essential for providing optimal therapy for the patients; MDCT is the most commonly used imaging modality for diagnosing and staging pancreatic adenocarcinoma. It allows pancreatic imaging with a very high spatial and temporal resolution within a short breath-hold and is still considered the gold standard for evaluation of pancretic solid tumors [6]. A complete and accurate assesment of the primary tumor, it's relationship with adjacent vascular structures and distant metastatic disease is required for accurate characterization of disease as resectable, borderline resectable or unresectable. The

resection criteria include: no invasion into major arteries; short segment of SMV (superior mesenteric vein) and portal vein involvement (in order to allow venous reconstruction) and absence of distant metastases.

The overall sensitivity of CT in the detection of pancreatic adenocarcinoma according to the literature has improved over the recent years, ranging between 75 and 100 %, with specificity of 70-100 % [7-9,11]. CT is considered to be the most reliable technique for evaluating unresectable tumor, with reported sensitivity and specificity of 79-94 % and 82-89 % respectively [10,11].

According to our study results, CT sensitivity of determining T1/T2 stage tumors was quite low - 62.5 %; specificity 94.4 %, positive predictive value 42.9 % (TPV) and negative predictive value 93 % (NPV). But the sample of T1/T2 groups is very small, so the results should be interpreted with caution.

T3 tumors were detected in 68.4% of all cases. CT sensitivity and specificity for T3 were 83.3% and 48% respectively and TPV and NPV were 77.6% and 57.1% respectively. Figure 1 demonstrates CT image of T2 disease.

T4 stage was detected in 6.3% of cases. CT sensitivity and specificity in T4 disease were 60% and 94.6% respectively and TPV and NPV - 42.9% and 97.2% respectively. These results should be interpreted with caution as well due to a small sample size. Figure 2 demonstrates an example of T4 disease.

**Figure 1. CT images of T2 disease Our case of T3 stage disease; contrast enhanced CT image, axial plane, venous phase; hypodense mass in the head of the pancreas abutting the superior mesenteric vein (arrow); no narrowing of the vessel is seen.**

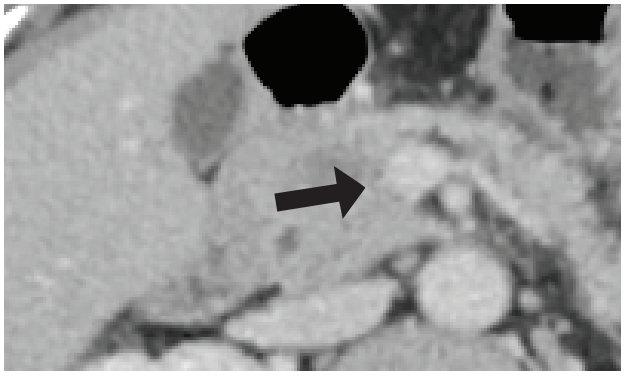

**Figure 2. CT images of unresectable T4 stage disease. The patient with pancreatic head adenocarcinoma with duodenal obstruction and dilatation of the stomach a) axial contrast enhanced CT image, arterial phase; an illdefined hypodense mass in the head of the pancreas ( arrow) with circumferential surrounding of SMA b) portal venous phase of the same patient shows involvement of SMV ( arrow).**

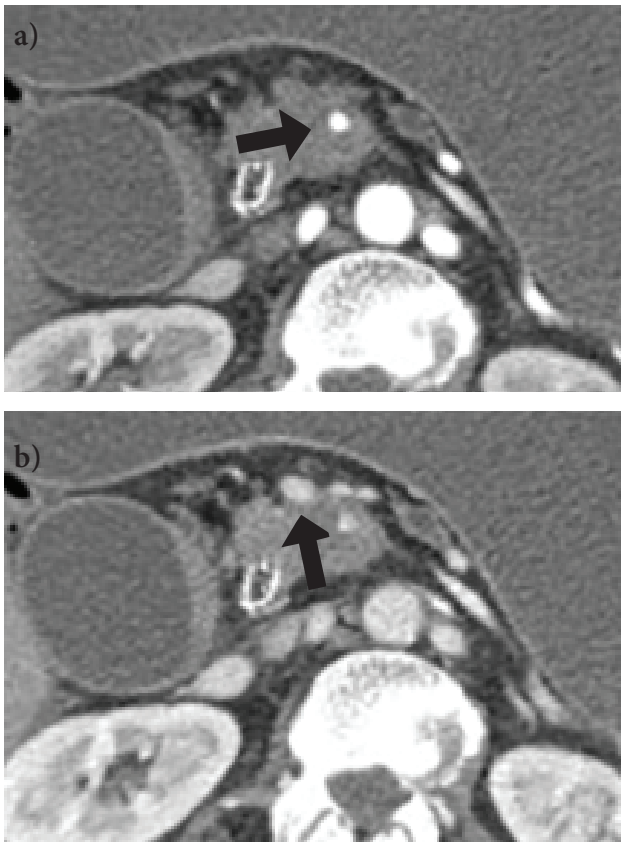


**Figure 3. CT image of T4 stage disease with „tear drop deformity" of SMV. Axial contrast enhanced CT image; venous phase; a hypodense mass in the head of the pancreas involving SMV with teardrop deformity (arrow).**

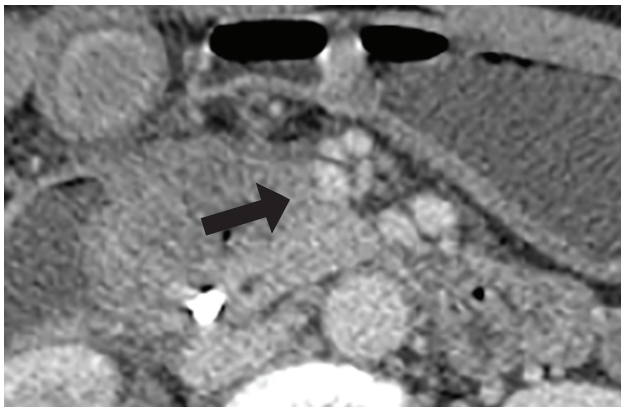

We also evaluated overall CT values for N staging of panreatic adenocarcinoma: 69.6% sensitivity and specificity was 75% and 59.3% respectively, TPV and NPV 78% and 55.2% respectively.
According to different authors, CT accuracy of N staging varies from 44 to 75 % and is not very accurate [11, 12]. In our study sensitivity of N staging based on CT scans is not very high, as well as accuracy and specificity. Although, we had cases when no pathological lymph nodes were visible on CT scans (CT N0 disease), however histological study revealed stage N1 disease. But in general, preoperative detection of peritumoral lymph nodes was estimated as not essential for assessing the resectability of pancreatic adenocarcinoma, because these lymph nodes are resected together with the primary tumor;
In conclusion, contrast enhanced CT is the primary imaging modality for the detection and staging of pancreatic adenocarcinoma; and our study results of preoperative assessment of pancreatic cancer T and N staging are very similar to those reported in the literature.
In the assesment of vessel invasion, the „teardrop vein sign" is a diagnostic sign of unresectable cancer [13, 14]. So, in our study we considered this sign as sign of unresectable disease (Figure 3).

## CONCLUSIONS

• CT is specific and accurate imaging modality in T stage of pancreatic adenocarcinoma.
• CT is quite sensitive, but non specific in N stage of pancreatic adenocarcinoma.

## REFERENCES

1. Evans db, george B, Tsai S. Non metastatic pancreatic cancer: resectable, borderline resectable, and locally advanced-definitions of increasing importance for the optimal delivery of multimodality therapy. Ann SurgOncol. 2015;22 (11):3409-13

2. Lu DS, Reber HA, Krasny RM, Kadell BM, Sayre J. Local staging of pancreatic cancer: criteria for unresectability of major vessels as revealed by pancretaic –phase, thin section helical CT. AJR Am J Roentgenol. 1997;168(6):1439-43.

3. Gillen S, Schuster T, Meyer Zum Buschenfelde C, Friess H, Kleeff J. Preoperative / neoadjuvant therapy in pancreatic cancer: a systematic review and meta-analysis of response and resection percentages. PloS Med. 2010;7(4):e1000267

4. Ishikawa O, Ohigashi H, Imaoka S, Furukawa H, Sasaki Y, Fujita M, et al. Preoperative indications for extended pancreatectomy for locally advanced pancreas cancer involving the portal vein. Ann Surg. 1992:215 (3): 231-6,

5. https://onlinecourses.science.psu.edu/stat507/node/71/

6. Katz MH, Marsh R, Herman JM, SHI Q, Collison E, Venook AP, et al. Borderline resectable pancreatic cancer: need for standartization and methods for optimal clinical trial design. Ann Surg Oncol. 2013;20(8):2787-95.

7. Bronstein YL, Loyer EM, Kaur H et al (2004) detection of small pancreatic tumors with multiphasic helical CT. AJR Am J Roentgenol 182:619-623

8. De Witt J, Devereaux B, Chriswell M et al (2004) Comparison of endoscopic ultrasonography and multidetector computed tomography for detecting and staging pancreatic cancer. Ann Intern Med 141:753-763.

9. Fusari M, Maurea S, Imriaco M et al (2010 Comparison between multislice CT and MR imaging in the diagnostic evaluation of patients with pancreatic masses. Radiol Med 115:453-466)

10. Karmazanovsky G, fedorov V, Kubyshkin V et al (2005) Pancretaic head cancer: accuracy of CT in determination of resectability. Abdom Imaging 30:488-500

11. Mirko D'Onofrio, Paola Capelli, Paolo Pederzoli (2015) Imaging and pathology of Pancreatic Neoplasms; a pictorial Atlas.

12. Roche CJ, hughes ml, garvey CJ et all (2003) CT and pathologic assessment of prospective nodal staging in patients with ductal adenocarcinoma of the head of the pancreas. AJR Am J Roentgenol 180:1311-1323

13. Hough TJ, Raptopoulos V Siewert B, Matthews JB (1999) teardrop superior mesenteric vein: CT sign for unresectable carcinoma of the pancreas. AJR Am J Roentgenol 173:1509-1512

14. Fuhrman GM, Leach SD, Staley CA et al (1996)Rationale for en bloc vein resection in the treatment of pancreatic adenocarcinoma adherent to the superior mesenteric-portal vein confluence. Pancreatic tumor study group. Ann surg 223:154-162.

15. https://www.nccn.org/professionals/physician_gls/default.aspx

16. NCCN Clinical Practice Guidelines in Oncology (NCCN GUIdelines). Pancreatic Adenocarcinoma. Version 3.2017 – September 11, 2017; NCCN.org

# Radiologic imaging of the inflammatory renal diseases: literature review

**Ruta Pupalyte[1], Algidas Basevicius[2]**

[1] *Faculty of Medicine, Lithuanian University of Health Sciences, Kaunas, Lithuania,*
[2] *Department of Radiology, Lithuanian University of Health Sciences, Kaunas, Lithuania*

## ABSTRACT

**Background and aim:** Inflammatory diseases of the kidney are a broad group of various renal pathologies. They are usually recognized by clinical symptoms and laboratory tests. However, radiology also has a role. The aim of this article is to assess radiologic imaging possibilities in diagnosis and follow-up of the most common inflammatory renal diseases.

**Materials and methods:** A selective search was carried out for relevant studies regarding radiologic imaging of acute pyelonephritis, renal and perinephric abscesses, emphysematous pyelonephritis, emphysematous pyelitis, chronic pyelonephritis and glomerulonephritis. ClinicalKey, Cochrane Library, Medline (PubMed), ScienceDirect and SpringerLink databases were used.

**Results:** Ultrasound is usually used as the initial imaging tool to evaluate patients with symptoms of acute pyelonephritis. However, computed tomography is the most appropriate imaging modality. If an abscess or gas-forming infection are suspected, CT is the modality of choice. The findings characteristic, yet not pathognomic to chronic pyelonephritis can be assessed using all of the previously mentioned imaging tools. In cases of glomerulonephritis, US and MRI are the most suitable.

**Conclusion:** Radiology plays an important role in diagnosis of inflammatory renal diseases. Imaging allows to identify renal abnormalities and differentiate between a few feasible pathologies. It may also evaluate the activity of the disease. Moreover, it can assess sequelae, such as renal scarring and decreased renal function.

***Keywords:*** pyelonephritis, renal abscess, glomerulonephritis, ultrasound, computed tomography, magnetic resonance imaging.

## 1. INTRODUCTION

Inflammatory diseases of the kidney are a broad group of various renal pathologies. These diseases can be insintric or manifest as systemic illnesses. The etiology of inflammation may be diverse, e.g. infectious or autoimmune. Inflammatory diseases are usually recognized by clinical symptoms and laboratory tests, such as blood count, C-reactive protein, autoantibodies and urinalysis [1, 2]. In some cases, percutaneous renal biopsy is the sole method that can confirm the diagnosis. However, it is an invasive procedure with potential complications [3].

Therefore, radiology also plays a role in the diagnosis. Radiologic imaging is constantly evolving and more new techniques emerge. With a wide variety of renal imaging tools, it is important to choose the modality which would provide the most information about the nature and extent of inflammatory lesions.

## 2. AIM

To assess radiologic imaging possibilities in diagnosis and follow-up of the most common inflammatory renal diseases.

## 3. MATERIALS AND METHODS

A selective search was carried out for relevant studies regarding radiologic imaging of acute pyelonephritis (APN), renal and perinephric abscesses, emphysematous pyelonephritis (EPN), emphysematous pyelitis (EP), chronic pyelonephritis (CPN) and glomerulonephritis (GN). We selected databases from the subscription list of Lithuanian University of Health Sciences. ClinicalKey, Cochrane Library, Medline (PubMed), ScienceDirect and SpringerLink databases were used.

## 4. RESULTS

Intravenous urography (IVU) has been replaced

almost completely by other modalities in diagnosis of APN, although this imaging technique was commonly performed in the past.

Ultrasound (US) is used as the initial imaging tool to evaluate patients with symptoms of APN. However, examination is usually normal due to relatively low sensitivity and specifity of this modality [4].

Computed tomography (CT) is the most appropriate imaging modality for diagnosing APN and its complications [5–8]. CT can also be useful in predicting the clinical course of the disease [9–11].

Magnetic resonance imaging (MRI) is not commonly used in diagnosing acute renal infections. Nonetheless, it is a radiation-free alternative for those patients who should not be exposed to radiation or are allergic to iodinated contrast agents.

Renal cortical scintigraphy (RCS) has high sensitivity in diagnosing renal infection [5, 12, 13]. RCS is considerably superior to IVU and US [14], as reliable as CT [5] and inferior to enhanced MRI [15] and DWI-MRI [16] in the acute phase of APN. Planar RCS is also slightly inferior or equivalent to single photon emission computed tomography (SPECT) in detecting pyelonephritic lesions [13, 17, 18].

If renal or perinephric abscess is suspected, CT is the modality of choice [19, 20]. MRI is not a frequently used imaging technique. US is inferior to CT and MRI in diagnosing renal abscesses [21].

US underestimates the depth of parenchymal involvement and perinephric extention of emphysematous pyelonephritis [22]. Therefore, CT is the most reliable imaging modality [23, 24].

Findings characteristic, yet not pathognomic to chronic pyelonephritis can be assessed using all of the above mentioned modalities. However, CT and MRI depict these findings in more detail. In cases of glomerulonephritis, US and MRI are the most appropriate imaging tools.

**Figure 1. Bilateral focal acute pyelonephritis. Axial contrast-enhanced CT depicts a few hypodense wedged-shaped pyeonephritic lesions in both kidneys. (Wang JH. Acute focal pyelonephritis. Urol Sci 2013; 24: 56-57)**

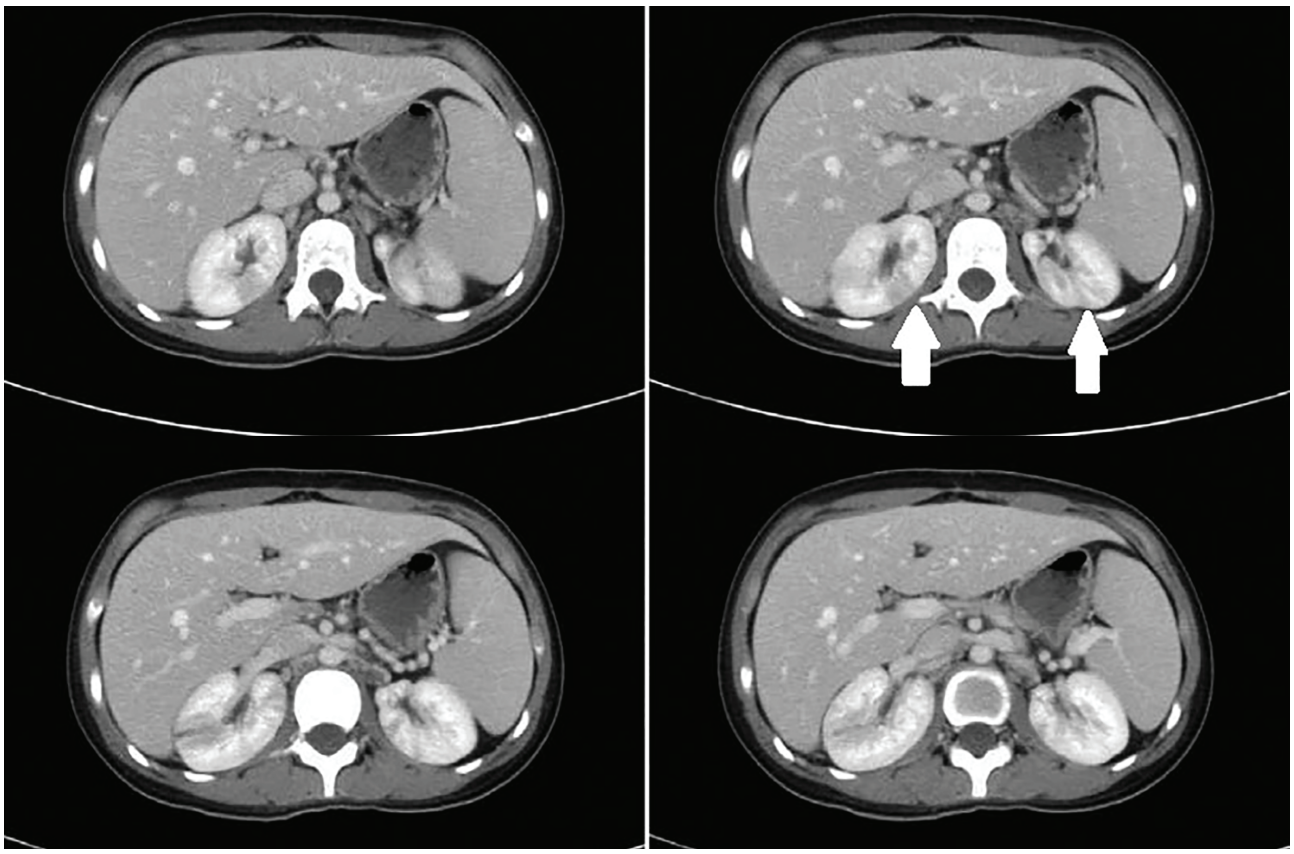

**Figure 2. Renal abscess. A well-defined hypodense lesion with peripheral enhancement is observed on coronal contrast-enhanced CT scan. (Linder BJ, Granberg CF. Pediatric renal abscesses: a contemporary series. J Pediatr Urol 2016; 12: 99.e1-99.e6)**

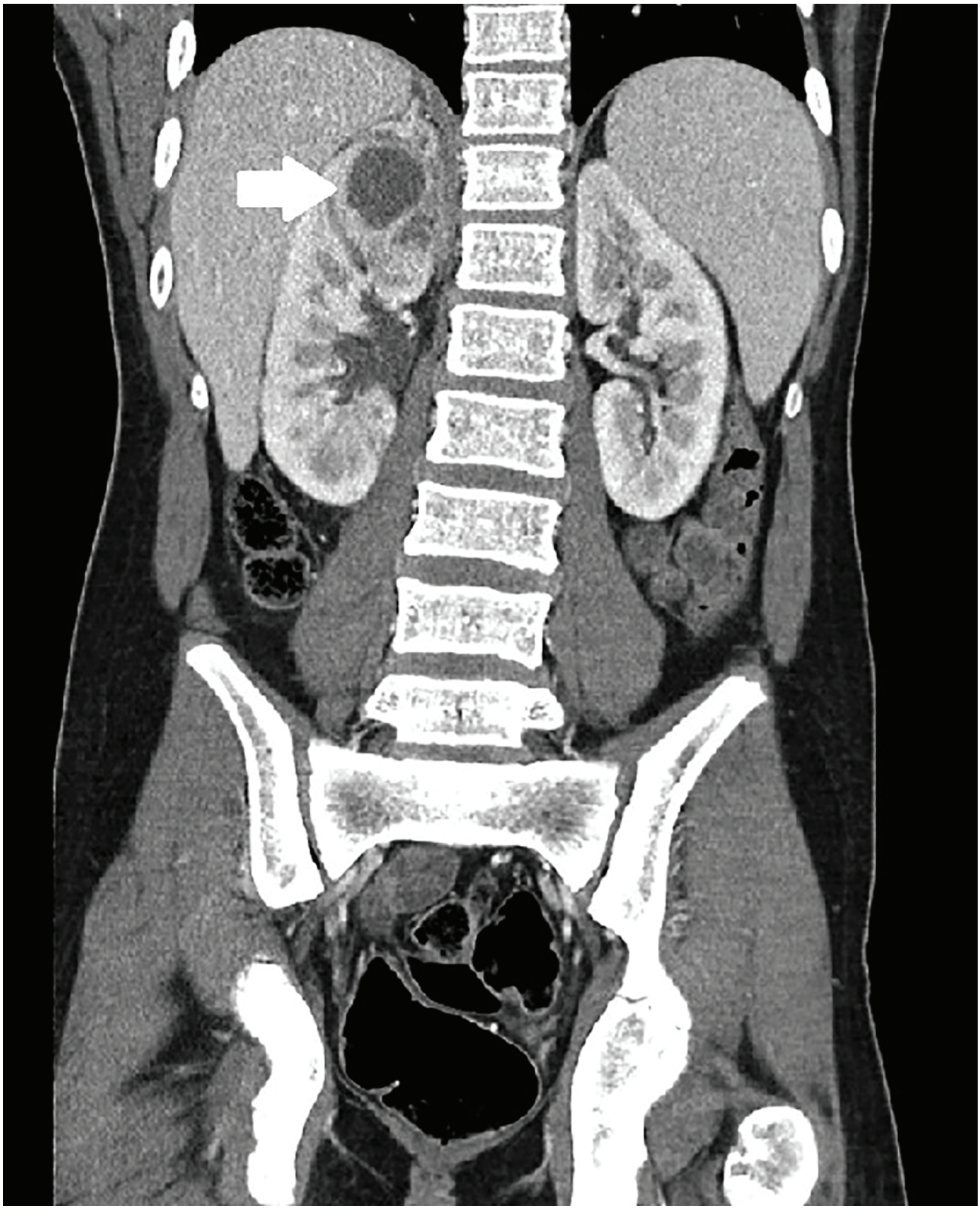

**Figure 3. Emphysematous pyelonephritis. Native CT shows enlarged bilateral kidneys with gas collections in the renal parenchyma. (Yao J, Gutierrez OM, Reiser J. Emphysematous pyelonephritis. Kidney Int 2007; 71: 462-465)**

**Figure 4. Emphysematous pyelitis. Gas in the bilateral pelvises and ureters (arrows) is observed on coronal native CT scan. Also, gas is seen in the left ureterovesicular junction (arrowhead). Asterisks show fat stranding. (Wiesel S, Hutman A, Abraham JE, Kiroycheva M. Foley follies: emphysematous pyelitis from instrumentation in obstructive uropathy. Cureus 2017; 9: e1612)**

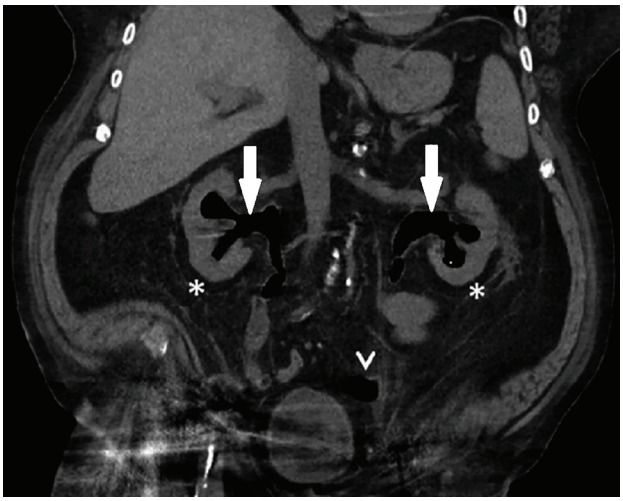

**Figure 5. Chronic pyelonephritis. On US, the right kidney is apparently smaller than the left one 7.6 cm vs. 11.5 cm). The renal parenchyma is echogenic and thin. Hypertrophy of the left kidney is observed. (Paltiel HJ, Babcock DS. The pediatric urinary tract and adrenal glands. In: Rumack C, Levine D. Diagnostic ultrasound. 5th ed. Philadelphia, PA, USA: Elsevier; 2018. pp. 1775-1832)**

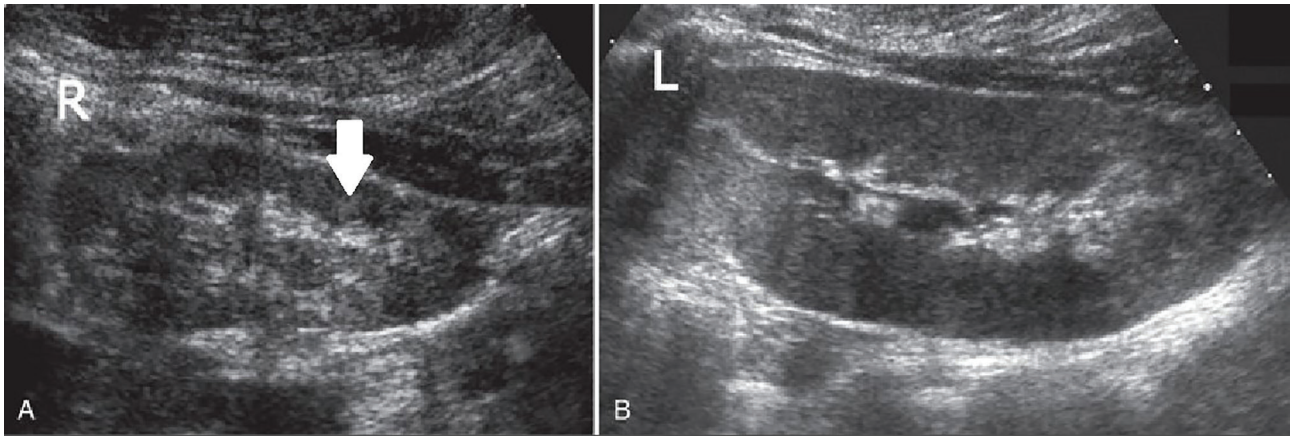

**Figure 6. Chronic pyelonephritis. Axial (a) and coronal (b) contrast-enhanced CT demonstrates scarring with cortical retraction (arrows) and calyceal deformation characteristic to CPN. (Ifergan J, Pommier R, Brion MC, Glas L, Rocher L, Bellin MF. Imaging in upper urinary tract infections. Diagn Interv Imaging 2012; 93: 509–519)**

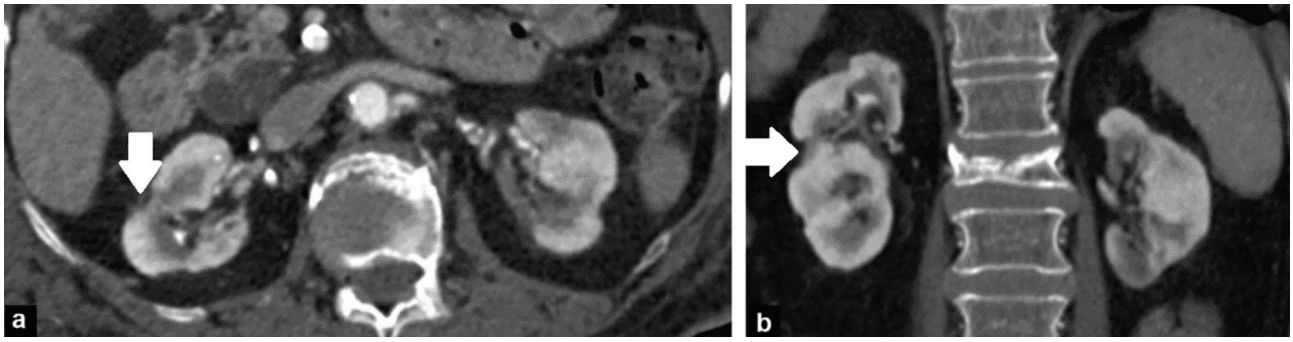


**Figure 7. Chronic glomerulonephritis. ADC maps (a-e) and FA maps (f-j) are shown in different disease stages (1-5) using MRI-DTI. Low signal region of the renal medulla on ADC maps and high signal region on FA maps decreases with each stage. Loss of corticomedullary differentiation is also apparent with increased stages. (Feng Q, Ma Z, Wu J, Fang W. DTI for the assessment of disease stage in patients with glomerulonephritis - correlation with renal histology. Eur Radiol 2015; 25: 92–98)**

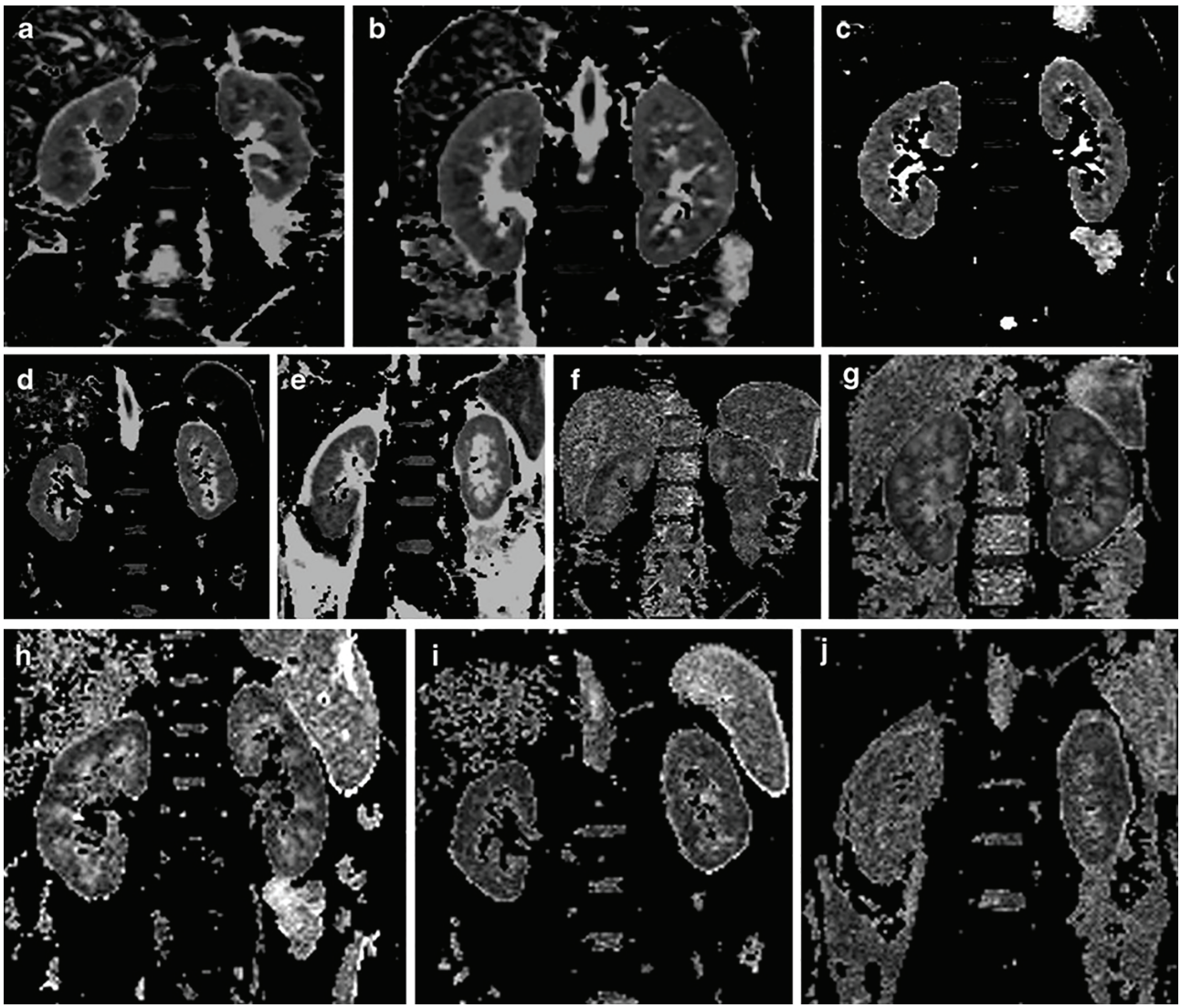

## 5. DISCUSSION

APN is an inflammation of the renal parenchyma and collecting system. Incidence rates of APN are highest in young females, infants and the elderly population [25, 26]. The most frequent causative uropathogen is Escherichia coli (70-80%) [25]. In most cases, APN is unilateral [27]. Diagnosis of APN is based on clinical and laboratory findings, therefore, radiologic imaging is not routinely used. However, diagnostic imaging allows to exclude urgent urinary pathologies.

In approximately 75% cases of uncomplicated APN, IVU is normal [14].

Abnormal findings characteristic to acute renal infection are diffuse renal enlargement, striated or delayed renal nephrogram and effacement or dilatation of the collecting cavities with delayed contrast medium filling [14]. Papillary necrosis, one of the possible complications of APN, can also be diagnosed on IVU [28].

Excretory urography is useful for assessment of the pelvocalyceal anatomy, however, it visualizes the renal parenchyma poorly [29].

On conventional US (CUS), generalised edema of the afftected kidney, loss of corticomedullary differentiation, pelvicalyceal thickening and dilatation without any evident obstruction are typical features of diffuse APN [4, 14, 30]. Hyperehoic perirenal fat, implying inflammatory response of the adjacent tissue, is also suggestive of diffuse APN.

In cases of focal APN, wedge-shaped or round hyper-, iso- or hypoechoic areas with regional loss of corticomedullary differentiation can be seen in the renal parenchyma [4, 14, 31, 32] These abnormal mass-like areas can be of low attenuation and have indistinct margins [33, 34]. Therefore, differentiation from renal abscess and tumours is important.

As a result of APN, renal scarring can develop, especially in patients with vesicoureteral reflux or recurrent infection [35]. On CUS, irregular contour, focal parenchymal thinning and underlying calyceal deformation are indicative of scars caused by previous infection [36–38].

The additional use of color or power Doppler increases sensitivity of CUS in diagnosis of focal APN [39, 40]. These imaging techniques present pyelonephritic lesions as hypovascular or even avascular foci [41–43].

However, several studies established that contrast-enhanced ultrasonography (CEUS) displays parenchymal abnormalities, associated with APN, better [44, 45]. Characteristic to focal APN, wedge-shaped or round hyperechoic lesions are hypoenchancing during the cortical and early parenchymal phase, isoenchancing and then hypoenchancing in the late parenchymal phase [43, 46]. These CEUS findings allow to exclude the growth of an abscess if a patient is unresponsive to antibiotic therapy. Nonetheless, using contrast enhancement in evaluating the affected kidney has not yet become the general practise because it does not significantly improve the accuracy of US [47].

Lastly, more recent techniques, such as tissue harmonic imaging (THI) and pulse inversion harmonic imaging (PIHI), has become valuable in abdominal imaging. These techniques provide higher spatial resolution. According to Kim et al., THI and PIHI, whether or not contrast material is used, are superior to CUS in the detection of focal pyelonephritic lesions [34].

Multiphasic helical CT protocol allows to evaluate kidneys accurately for APN [48]. Non-contrast CT may appear without any abnormal findings in patients with diffuse APN. It can also demonstrate only secondary signs of renal infection, such as low-attenuation renal parenchyma [49], general renal enlargement, pelvocalyceal thickening and enhancement, soft tissue perinephric stranding and thickening of the anterior pararenal (Gerota's) fascia [28, 50]. If radiologic imaging is performed early, wall thickening of the pelvis and calyces can be the only feature of the disease [48].

On native CT scans, focal APN presents in a different manner. Involved areas usually appear oval or wedge-shaped, ill-defined and hypodense owing to edema or necrosis [7, 21, 49, 50]. In rare cases of haemorrhagic focal APN, non-contrast CT shows hyperdense lesions due to parenchymal bleeding [32]. Therefore, abnormal density of renal lesions on CT correspond to echogenicity on CUS [7, 32]. Focal pyelonephritic lesions have a lobular distribution, contrary to renal abscesses. If a CT scan presents with round, not

wedge-shaped low attenuation peripheral renal lesions in a patient displaying symptoms of APN, hematogenous seeding should be considered.

A recent study demonstrated association of focal APN to atypical radiological findings. Pleural effusion, presence of fluid around the gallblader, thickened gallblader wall, perinephric fluid and ascites are more frequent in patients with focal form of APN [51].

Postcontrast CT examination commonly shows solitary or multiple wedge-shaped zones of low attenuation extending from the papilla to the cortical surface with poor corticomedullary differentiation (Figure 1). Enhancement of abnormal areas is inhomogeneous, delayed and only moderate, always less than of unaffected parenchyma [7, 42, 50, 52]. Moreover, sharply defined alternating bands of increased and decreased attenuation („striations") within the wedge-shaped lesions can be observed during nephrographic phase [47]. These uni- or multifocal lobular striations are the result of tubular stasis of contrast material due to inflammatory tubular obstruction [53]. However, „striated nephrogram" is characteristic, but not pathognomonic of APN. It may also be observed in cases of contusion, renal vein thrombosis, ureteric obstruction and dehydratation [54].

CT can promptly lead to the diagnosis of APN. However, it should be preserved for patients with history of diabetes mellitus, renal calculi or renal surgery and those who are unresponsive to antibiotic therapy after 72 hours.

MRI findings of APN are similar to those of CT. The affected kidney is focally or diffusely enlarged with poor corticomedullary differentiation and typical heterogeneous edematous lesions, i.e., low signal intensity (SI) on T1-weighted (T1W) images and high SI on T2-weighted (T2W) images [55, 56]. These edematous areas are better represented using T2W images with fat supression technique [48]. Perirenal effusion, stranding and pelvocalyceal wall thickening can be found, but these signs are not pathognomic to APN [48, 55].

Renal scarring, a sequela of APN, appears as a contour deformity without signal change [15].

MRI with gadolinium depicts renal lesions as wedge-shaped or round, sometimes striated regions of decreased or absent enhancement [56]. Inversion recovery MRI with gadolinium uses the negative enhancement effect of the contrast material. Unaffected renal parenchyma becomes hypointense, contrary to the inflammatory areas that remain hyperintense due to edema and poor delivery of the contrast medium [15].

However, T1W and T2W images are not sensitive enough to detect pyelonephritic lesions [56]. Various studies reveal the utility of diffusion weighted imaging (DWI) in cases with suspected APN. According to De Pascale et al., sensitivity and specificity of DWI-MRI is 95.2% and 94.9%, respectively [55]. On DWI, APN presents as areas of restricted diffusion, corresponding to the T1W and T2W parenchymal signal changes. Pyelonephritic lesions are hyperintense. Reduced SI is seen on apparent diffusion coefficient (ADC) maps [55, 57, 58]. DWI displays high diagnostic agreement with gadolinium-enhanced images [55, 57]. Moreover, DWI does not require contrast medium, hence, it can be used in patients with renal insufficiency or pregnant women. Therefore, unenhanced MRI with DWI should be a comprehensive examination in diagnosing APN [55, 57].

MR urography (MRU) allows to assess the urinary tract for obstruction which may predispose APN [59, 60]. Thus, the combination of conventional MRI and MRU is appropriate to evaluate renal infection, its complications and the urinary tract for dilatation. Furthermore, conventional MRI together with MRU allows to obtain morphologic and functional data and eliminates the need for renal scintigraphy, especially in children [61, 62].

There is no general agreement for the use of RCS in diagnosis of pyelonephritis. In pediatric population, clinical and laboratory findings frequently do not correlate to RCS, thus, RCS is important in diagnosis of APN [63]. Nevertheless, it is not recommended in routine practice [64, 65].

Several tracers are available, although 99mTc-dimercaptosuccinic acid (99mTc-DMSA) is the most appropriate. The uptake of 99mTc-DMSA correlates to the volume of functioning renal parenchyma. In patients with APN, scintigraphy usually displays reduced focal or diffuse build-up of the radiopharmaceutical without cortical

or volume loss [12, 15, 17]. Relative left and right 99mTc-DMSA uptake can be measured, normal lowest value being 45%. In cases of APN, relative uptake can be decreased [12]. These findings are not specific to the disease, hence, combination of RCS and other imaging modalities should be used.

RCS is also used for detecting the consequences of APN [16, 66, 67]. In adult patients, renal scarring is rare, therefore, RCS examination is more frequent in children. In 42% of pediatric population, persistent cortical abnormalities are found [68]. Normal RCS scans during the acute phase of APN show a low risk of scarring later [69]. Scars present as defects in uptake with cortical thinning and loss of volume in the same area as pyelonephritis [16]. Inflammatory parenchymal changes tend to dissapear only after a few months after the episode of APN [70]. In order to assess possible sequelae, it is recommended to undergo scintigraphy for pediatric patients at least 6 months after APN [65].

Renal abscess is a collection of pus limited to the kidney. In most cases of APN, patients do not experience this complication. However, if inflammation is severe, liquefarctive necrosis and, consequently, abscess can form. Several studies show that renal abscesses are more common in patients with diabetes mellitus and urolithiasis [19, 71]. Clinical and laboratory findings cannot identify patients with or without abscesses, therefore, radiologic imaging is important [21, 72].

In most cases of acute renal abscess, the kidney is enlarged with distorted outer contour. The abscess itself presents as a hypoechoic mass with through transmission and hazy borders [43, 52, 73, 74]. A fluid-filled mass with a thickened definite margins suggests a mature abscess [48]. Mobile debris can be observed inside the collection of pus [74]. On power Doppler, absent internal flow is seen [43].

Depiction of abscesess is better using THI and PIHI than CUS [34].

CEUS may demonstrate round unenhanced abscess cavities with possible rim or septa enhancement which allows to differentiate it from focal APN [43]. Nevertheless, US is inferior to CT and MRI in diagnosing renal abscesses [21].

Liquefaction of affected region is seen as a hypoattenuating area in the peripheral cortex on unenhanced CT [52].

Contrast-enhanced CT shows early renal abscess as a round hypodense well-defined fluid-filled area with an irregular wide halo of decreased enhancement, as shown in Figure 2 [74–77]. The outer contour of capsule can be irregular owing to surrounding inflammatory infiltration. Septations and areas of gas may also be observed within a suppuration [74], the latter being pathognomonic of an abscess. Secondary features of infection, such as thickening of Gerota's fascia, can also be found [52].

Collections of pus may be also observed in perinephric spaces [52]. Perinephric suppuration usually originates from ruptured renal cortical abscesses into the pararenal space. Furthermore, it can involve the muscles of the posterior abdominal wall, most frequently the psoas muscle. Hypodense mass with indistinct borders, gas bubbles or air-fluid levels in the enlarged psoas muscle leads to diagnosis of abscess [75, 78].

MRI is used as a substitute when CT scans cannot be performed. In cases of suppuration, MRI shows round inhomogenous hypointense lesions with thick walls on T1W images and hyperintense lesions with hypointense periphery on T2W images [56, 57].

Gadolinium-enhanced MRI scans display unenhanced areas, surrounded by high SI peripheral rim [56, 76]. Cellular debris and irregular septations can also be seen within the abscess. Edema or fine streaks of fluid can be found in the perirenal space [56].

On DWI-MRI, inflammatory changes are hyperintense with restricted ADC [57, 79].

EPN is a rare life-threatening, usually fulminant urologic infection with gas accumulation within or around the kidneys. Emphysematous pyelitis (EP) is a less severe gas-forming renal infection with gas limited only to the renal collecting system. However, mortality between patients with EPN and EP does not significantly differ [80]. Uropathogens, such as E. coli, Klebsiella, Proteus, use the necrotic tissue as a substrate to produce carbon dioxide, thus, gas formation is seen. EPN and EP are more common in female patients [22, 23, 80–83]. These diseases are usually

unilateral [22, 23, 80, 81]. Uncontrolled diabetes mellitus and urolithiasis are associated with EPN [23, 81, 84].

Abdominal radiograph can display mottled gas shadows over the renal fossa, which should not be mistaken for bowel gas [85, 86]. If EPN progresses, speckled or crescent-shaped gas collection can be seen. Calculi may be observed as well [23].

CUS shows an enlarged kidney with parenchymal or pelvocalyceal hyperechoic foci with posterior dirty acoustic shadowing that are characteristic of gas [85].

In cases of EPN, native CT detects the presence and extent of gas in the renal parenchyma and around the kidney, possible accumulation of perinephric fluid, abscesses, along with the origin of obstruction if present [86]. Intraparenchymal gas appear as small bubbles or fine streaks of air radiating from papillae on native CT (Figure 3). Contrast-enhanced CT may show irregular enhancement or delayed excretion [48].

Wan et al. characterized two types of EPN based on CT findings. Type 1 exhibits focal tissue necrosis with mottled or loculated gas collections in the renal parenchyma or collecting system. Gas can extend to the subcapsular, perinephric and pararenal spaces. In type 2, these features are accompanied by renal or perirenal fluid collections. Type 1 is more aggresive and, consequently, has a higher mortality rate than type 2 (69% vs. 18%) [87].

Huang et al. classified EPN into several classes according to CT. Class 1 presents only pelvocalyceal gas, class 2 is distinguished by parenchymal gas, in class 3A abscess or gas are extended to perinephric space, in class 3B extension is seen in pararenal space. Class 4 represents bilateral EPN [88].

These classifications allow to predict the course of EPN and apply the most appropriate treatment [22].

The lack of intraparenchymal gas differentiates EP from EPN [89]. In cases of EP, non-contrast CT demonstrates bubbles of gas or gas-fluid levels in the collecting system and pelvic or calyceal dilatation, as seen in Figure 4.

CPN is a chronic tubulointerstitial fibrosing nephritis that involves renal parenchyma and the collecting system. The purpose of radiologic imaging is to detect not only chronic renal damage, but also the underlying cause of the recurrent inflammation.

In cases of CPN, IVU usually shows focal contraction of the renal parenchyma with adjacent calyceal clubbing [90, 91]. However, this modality is not so commonly used.

On US, may display focal or diffuse renal atrophy, hyperechoic parenchyma, irregular contour, loss of corticomedullary differentiation and dilatation of the calyces (Figure 5) [92–94].

CTU and MRI depict the disease more in detail with renal atrophy, hypertrohy of residual normal tissue (pseudotumor), irregular borders, cortical thinning, poor corticomedullary differentiation, parenchymal scars, calyceal distortion and clubbing (Figure 6). Moreover, contralateral renal hypertrophy, as a compensatory mechanism, can be observed [48].

RCS displays defects of 99mTc-DMSA uptake characteristic to renal scarring.

Renal needle biopsy is a gold standart for diagnosing glomerulonephritis (GN). However, radiologic imaging is useful prior to biopsy.

Enlarged kidneys with either reduced or increased visibility of pyramids can be seen on CUS. Echogenicity of the renal parenchyma is associated to tubulointerstitial, not glomerular changes [95], [96]. In proliferative glomerulonephritis and interstitial nephritis tubulointerstitial compartment is severely damaged, therefore, renal cortex is hyperechoic. Contrary, renal parenchyma is normal in membranous glomerulonephritis, IgA nephropathy, minimal-change glomerulonpehritis and focal glomerulosclerosis at first. Nonetheless, progression of these diseases extend to the tubules and interstitium, hence, parenchyma gradually becomes hyperechoic [97]. In addition, CUS may demonstrate inhomogeneous renal sinus with poor renal sinus-parenchymal differentiation.

Doppler US allows to assess renal function precisely in patients with chronic GN. Several studies show that resistive index (RI) correlates to the extent of arteriolosclerosis, glomerulosclerosis and interstitial fibrosis [98, 99]. T.Yura et al. also established correlation between creatinine clearance and both peak systolic velocity and end-di-

astolic velocity. Moreover, inverse correlation between creatinine clearance, RI and pulsatility index (PI) was determined in their study [100]. RI usually increases only in acute crescentic and proliferative glomerulonephritis and diseases of the tubulointerstitial compartment. However, these findings are not specific to GN.

CEUS benefits in diagnosing early glomerular disease. According to M. Nestola et al., histological activity of GN correlates with persistence of contrasts material signal in the wash-out phase. Slower contrast agent wash-out purposes disturbed glomerular perfusion in early GN [101].

A recent study concluded that a quantitative elastography technique can also contribute to the early diagnosis of GN. Shear wave based elastography point quantification (ElastPQ) determines renal cortical stifness, which is higher in pediatric patients with glomerular disease [102]. Nonetheless, further research is needed.

MRI is another imaging modality that is helpful in diagnosis and follow-up of patients with chronic GN. Diffusion tensor imaging (DTI) allows to evaluate renal function and the degree of histopathological abnormalities. Glomerulosclerosis and tubulointerstitial fibrosis reduces parenchymal perfusion, leading to decreased diffusivity. These histopathological changes may also influence diffusion direction along the tubules. As a result, ADC and fractional anisotropy (FA) values decreases with increased chronic GN stages. Furthermore, corticomedullary differentiation is poorer with each stage, as shown in Figure 7 [103].

Contrast-enhanced MRI may differentiate active and treatable glomerular disease between sclerotic ones. In cases of chronic GN, ultrasmall superparamagnetic iron oxide particles (USPIO) are used as a contrast agent. USPIO displays cortical macrophage infiltration, corresponding to inflammatory renal regions. Due to accumulation of iron particles in mononuclear cells, MRI demonstrates diffusely decreased enhancement of renal parenchyma on T2W images after USPIO administration [104].

In conclusion, radiology plays an important role in diagnosis of inflammatory renal diseases. Imaging allows to identify renal abnormalities and differentiate between a few feasible pathologies. It may also evaluate the activity of the disease. Moreover, it can assess sequelae, such as renal scarring and decreased renal function. Although US is the first-line imaging modality in most of the cases, CT is usually referred to be the most informative one. MRI is a radiation-free alternative and is not routinely used. Nonetheless, it is relevant in the early detection of glomerulonephritis. In order to identify the sequelae of these diseases, RCS can be beneficial, especially in the pediatric population.

## REFERENCES


1. Koufadaki AM, Karavanaki KA, Soldatou, Tsentidis CH, Sourani MP, Sdogou T, Haliotis FA, Stefanidis. Clinical and laboratory indices of severe renal lesions in children with febrile urinary tract infection. Acta Paediatr 2014; 103: e404–e409.

2. Kirac Y, Bilen S, Duranay M. Comparison of laboratory findings in patients with glomerulonephritis classified according to histopathologic diagnosis. Minerva Medica 2014; 105: 149-156.

3. Al Turk AA, Estiverne C, Agrawal PR, Michaud JM. Trends and outcomes of the use of percutaneous native kidney biopsy in the United States: 5-year data analysis of the Nationwide Inpatient Sample. Clin Kidney J 2017; 11(3): 330–336.

4. Nickavar A, Safaeian B, Biglari abhari M. Radiologic and clinical evaluation of children with first febrile urinary tract infection. Int J Pediatr Adolesc Med 2015; 2: 24–28.

5. Yoo JM, Koh JS, Han CH, Lee SL, Ha U-S, Kang SH, Yung YS, Lee YS. Diagnosing acute pyelonephritis with CT, 99mTc-DMSA SPECT, and Doppler ultrasound: a comparative study. Korean J Urol 2010; 51: 260–265.

6. Nikolic O, Stojanovic S, Till V, Basta-Nikolic M, Petrovic K, Vucaj-Cirilovic V. Multislice computed tomography urography in the diagnosis of urinary tract diseases. Vojnosanit Pregl 2011; 68(5): 417–422.

7. Lee JKT, McClennan BL, Melson GL, Stanley RJ. Acute focal bacterial nephritis: emphasis on grey scale sonography and computed tomography. AJR 1980; 135: 87-92.

8. Venkatesh L, Hanumegowda RK. Acute pyelonephritis - correlation of clinical parameter with radiological imaging abnormalities. J Clin Diagnostic Res 2017; 11(6): TC15-TC18.

9. Piccoli GB, Colla L, Burdese M, Marcuccio C, Mezza E, Maass J, Picciotto G, Sargiotto A, L. Besso, Magnano E et al. Development of kidney scars after acute uncomplicated pyelonephritis: relationship with clinical, laboratory and imaging data at diagnosis. World J Urol 2006; 24: 66–73.

10. Cheng CH, Tsau YK, Chen SY, Lin TY. Clinical courses of children with acute lobar nephronia correlated with computed tomographic patterns. Pediatr Infect Dis J. 2009; 28: 300–303.

11. Lim SK, Ng FC. Acute pyelonephritis and renal abscesses in adults-correlating clinical parameters with radiological (computer tomography) severity. Ann Acad Med Singapore 2011; 40: 407–413.

12. Lavocat MP, Granjon D, Allard D, Gay C, Freycon MT, Dubois F. Imaging of pyelonephritis. Pediatr Radiol 1997; 27: 159–165.

13. Majd M, Rushton HG, Chandra R, Andrich MP, Tardif CP, Rashti F. Technetium-99m-DMSA renal cortical scintigraphy to detect experimental acute pyelonephritis in piglets: comparison of planar (pinhole) and SPECT imaging. J Nucl Med 1996; 37: 1731–1734.

14. Sty JR, Wells RG, Starshak RJ, Schroeder BA. Imaging in acute renal infection in children. AJR 1987; 148: 471–477.

15. Kovanlikaya A, Okkay N, Cakmakci H, Ozdogan O, Degirmenci B, Kavukcu S. Comparison of MRI and renal cortical scintigraphy findings in childhood acute pyelonephritis: preliminary experience. Eur J Radiol 2004; 49: 76–80.

16. Bosakova A, Salounova D, Havelka J, Kraft O, Sirucek P, Kocvara R, Hladik M. Diffusion-weighted magnetic resonance imaging is more sensitive than dimercaptosuccinic acid scintigraphy in detecting parenchymal lesions in children with acute pyelonephritis: a prospective study. J Pediatr Urol 2018; 14: 269. e1-269.e7.

17. Kavanagh EC, Ryan S, Awan A, McCourbrey S, O'Connor R, Donoghue V. Can MRI replace DMSA in the detection of renal parenchymal defects in children with urinary tract infections? Pediatr Radiol 2005; 35: 275–281.

18. Brenner M, Bonta D, Eslamy H, Ziessman HA. Comparison of 99mTc-DMSA dual-head SPECT versus high-resolution parallel-hole planar imaging for the detection of renal cortical defects. AJR 2009; 193: 333–337.

19. Liu XQ, Wang CC, Liu YB, Liu K. Renal and perinephric abscesses in West China Hospital: 10-year retrospective-descriptive study. World J Nephrol 2016; 5(1): 108-114.

20. Manjon CC, Sanchez AT, Lara JDP, Silva VM, Betriu GC, Sanchez AR, Penalver CG, Galvis OL. Retroperitoneal abscesses - analysis of a series of 66 cases. Scand J Urol Nephrol 2003; 37: 139–144.

21. Rollino C, Beltrame G, Ferro M, Quattrocchio G, Sandrone M, Quarello F. Acute pyelonephritis in adults: a case series of 223 patients. Nephrol Dial Transplant 2012; 27: 3488–3493.

22. Tsu JHL, Chan CK, Chu RWH, Law IC, Kong CK, Liu PL, Cheung FK, Yiu MK. Emphysematous pyelonephritis: an 8-year retrospective review across four acute hospitals. Asian J Surg 2013; 36: 121–125.

23. Wang JM, Lim HK, Pang KK. Emphysematous pyelonephritis. Scand J Urol Nephrol 2007; 41: 223–229.

24. Kim DS, Woesner ME, Howard TF, Olson LK. Emphysematous pyelonephritis demonstrated by computed tomography. AJR 1979; 132: 287–288.

25. Czaja CA, Scholes D, Hooton TM, Stamm WE. Population-based epidemiologic analysis of acute pyelonephritis. Clin Infect Dis 2007; 45: 273–280.

26. Ki M, Park T, Choi B, Foxman B. The epidemiology of acute pyelonephritis in South Korea, 1997-1999. Am J Epidemiol 2004; 160(10): 985–993.

27. Lee YJ, Cho S, Kim SR. Unilateral and bilateral acute pyelonephritis: differences in clinical presentation, progress and outcome. Postgrad Med J 2014; 90: 80–85.

28. Kawashima A, Sandler CM, Goldman SM, Raval BK, Fishman EK. CT of renal inflammatory disease. Radiographics 1997; 17(4): 851-866.

29. Craig WD, Wagner BJ, Travis MD. Pyelonephritis: radiologic-pathologic review. RadioGraphics 2008; 28: 255–277.

30. Dinkel E, Orth S, Dittrich, M, Schulte-Wissermann H. Renal sonography in the differentiation of upper from lower urinary tract infection. AJR, 1986; 146: 775–780.

31. Farmer KD, Gellett LR, Dubbins PA. The sonographic appearance of acute focal pyelonephritis 8 years experience. Clin Radiol 2002; 57: 483–487.

32. Rigsby CM, Rosenfield AT, Glickman MG, Hodson J. Hemorrhagic focal bacterial nephritis: findings on gray-scale sonography and CT. AJR 1986; 146: 1173–1177.

33. Kao HW, Wu CJ. Ultrasound of renal infectious disease. J Med Ultrasound 2008; 16(2): 113–122.

34. Kim B, Lim HK, Choi MH, Woo JY, Ryu J, Kim S, Peck KR. Detection of parenchymal abnormalities in acute pyelonephritis by pulse inversion harmonic imaging with or without microbubble ultrasonographic contrast agent: correlation with computed tomography. J Ultrasound Med 2001; 20: 5–14

35. Ehsanipour F, Gharouni M, Rafati AH, Ardalan M, Bodaghi N, Otoukesh H. Risk factors of renal scars in children with acute

pyelonephritis. Braz J Infect Dis 2012; 16(1): 15–18.

36. Chung EM, Soderlund KA, Fagen KE. Imaging of the pediatric urinary system. Radiol Clin N Am 2017; 55: 337–357.

37. Hamoui N, Hagerty JA, Maizels M, Yerkes EB, Chaviano A, Shore R, Kaplan WE, Cheng EY. Ultrasound fails to delineate significant renal pathology in children with urinary tract infections: a case for dimercapto-succinic acid scintigraphy. J Urol 2008; 180: 1639–1642.

38. Gulati M, Cheng J, Loo JT, Skalski M, Malhi H, Duddalwar V. Pictorial review: renal ultrasound. Clin Imaging 2018; 51: 133–154.

39. Dacher JN, Pfister C, Monroc M, Eurin D, Le Dosseur P. Power Doppler sonographic pattern of acute pyelonephritis. AJR 1996; 166: 1451-1455.

40. Winters WD. Power Doppler sonographic evaluation of acute pyelonephritis in children. J Ultrasound Med 1996; 15: 91-96.

41. Rathaus V, Werner M. Acute focal nephritis: its true sonographic face. Isr Med Assoc J 2007; 9: 729–731.

42. Uehling DT, Hahnfeld LE, Scanlan KA. Urinary tract abnormalities in children with acute focal bacterial nephritis. BJU Int 2000; 85: 885–888.

43. Fontanilla T, Minaya J, Cortes C, Hernando CG, Aranguena RP, Arriaga J, Carmona MS, Alcolado A. Acute complicated pyelonephritis: contrast-enhanced ultrasound. Abdom Imaging 2012; 37: 639–646.

44. Granata A, Andrulli S, Fiorini F, Basile A, Logias F, Figuera M, Sicurezza E, Gallieni M, Fiore CE. Diagnosis of acute pyelonephritis by contrast-enhanced ultrasonography in kidney transplant patients. Nephrol Dial Transplant 2011; 26: 715–720.

45. Mitterberger M, Pinggera GM, Colleselli D, Batsch G, Strasser H, Steppan I, Pallwein L, Friedrich A, Gradl J, Frauscher F. Acute pyelonephritis: comparison of diagnosis with computed tomography and contrast-enhanced ultrasonography. BJU Int 2008; 101: 341–344.

46. Bertolotto M, Bucci S, Valentino M, Curro F, Sachs C, Cova MA. Contrast-enhanced ultrasound for characterizing renal masses. Eur J Radiol 2018; 105: 41–48.

47. Ifergan J, Pommier R, Brion MC, Glas L, Rocher L, Bellin MF. Imaging in upper urinary tract infections. Diagn Interv Imaging 2012; 93: 509–519.

48. Quaia E, Reiser MF, Kauczor HU, Gricak H, Knauth M. Radiological imaging of the kidney. 2nd ed. Berlin, Germany: Springer; 2014.

49. El-Merhi F, Mohamad M, Haydar A, Naffaa L, Nasr R, Deeb IAS, Hamieh N, Tayara Z, Saade C. Qualitative and quantitative radiological analysis of non-contrast CT is a strong indicator in patients with acute pyelonephritis. Am J Emerg Med 2018; 36: 589–593.

50. Gold RP, McClennan BL, Rottenberg RR. CT appearance of acute inflammatory disease of the renal interstitium. AJR 1983; 141: 343–349.

51. Campos-Franco J, Macia C, Huelga E, Diaz-Louzao C, Gude F, Alende R, Gonzalez-Quintela A. Acute focal bacterial nephritis in a cohort of hospitalized adult patients with acute pyelonephritis. Assessment of risk factors and a predictive model. Eur J Intern Med 2017; 39: 69–74.

52. Hoddick W, Jeffrey RB, Goldberg HI, Federle MP, Laing FC. CT and sonography of severe renal and perirenal infections. AJR 1983; 140: 517-520.

53. Saunders HS, Dyer RB, Shifrin RY, Scharling ES, Bechtold RE, Zagoria RJ. The CT nephrogram: implications for evaluation of urinary tract disease. RadioGraphics 1995; 15(5): 1069–1085.

54. Yu M, Robinson K, Siegel C, Menias C. Complicated genitourinary tract infections and mimics. Curr Probl Diagn Radiol 2017; 46: 74–83.

55. De Pascale A, Piccoli GB, Priola SM, Rognone D, Consiglio V, Garetto I, Rizzo L, Veltri A. Diffusion-weighted magnetic resonance imaging: new perspectives in the diagnostic pathway of non-complicated acute pyelonephritis. Eur Radiol 2013; 23: 3077–3086.

56. Martina MC, Campanino PP, Caraffo F, Marcuccio C, Gunetti F, Colla L, Cassinis MC, Gandini G. Dynamic magnetic resonance imaging in acute pyelonephritis. Radiol Med 2010; 115: 287–300.

57. Vivier PH, Sallem A, Beurdeley M, Lim RP, Leroux J, Caudron J, Coudray C, Liard A, Michelet I, Dacher JN. MRI and suspected acute pyelonephritis in children: comparison of diffusion-weighted imaging with gadolinium-enhanced T1-weighted imaging. Eur Radiol 2014; 24(1): 19–25.

58. Aoyagi J, Odaka J, Kuroiwa Y, Nakashima N, Ito T, Saito T, Kanai T, Yamagata T, Momoi MY. Utility of non-enhanced magnetic resonance imaging to detect acute pyelonephritis. Pediatr Int 2014; 56: e4-e6.

59. Reuther G, Kiefer B, Wandl E. Visualization of urinary tract dilatation: value of single-shot MR urography. Eur Radiol 1997; 7: 1276–1281.

60. Vegar-Zubovic S, Kristic S, Lincender L. Magnetic resonance urography in children - when and why? Radiol Oncol 2011; 45(3): 174–179.

61. Boss A, Martirosian P, Fuchs J, Obermayer F, Tsiflikas I, Schick F, Schafer JF. Dynamic MR urography in children with uropathic disease with a combined 2D and 3D acquisition protocol-comparison with MAG3 scintigraphy. Br J Radiol 2014; 87: 20140426.

62. McDaniel BB, Jones RA, Scherz H, Kirsch AJ, Little SB, Grattan-Smith JD. Dynamic contrast-enhanced MR urography in the evaluation of pediatric hydronephrosis: part 2, anatomic and functional assessment of uteropelvic junction obstruction. AJR 2005; 185: 1608–1614.

63. Ilyas M, Mastin ST, Richard GA. Age-related radiological imaging in children with acute pyelonephritis. Pediatr Nephrol 2002; 17: 30–34.

64. American academy of pediatrics. Urinary tract infection: clinical practice guideline for the diagnosis and management of the initial UTI in febrile infants and children 2 to 24 months. Pediatrics 2011; 128(3): 595–610

65. Piepsz A, Colarinha P, Gordon I, Hahn K, Olivier P, Roca I, Sixt R, van Velzen J. Revised guidelines on 99mTc-DMSA scintigraphy in children. Eur J Nucl Med 2009; 28(3): BP37-41.

66. Araujo CB, Barroso JR U, Barroso VA, Vinhaes AJ, Jacobino M, Calado A, Filho MZ. Comparative study between intravenous urography and renal scintigraphy with DMSA for the diagnosis of renal scars in children with vesicoureteral reflux. Int Braz J Urol 2003; 29(6): 535–539.

67. Raz R, Sakran W, Chazan B, Colodner R, Kunin C. Long-term follow-up of women hospitalized for acute pyelonephritis. Clin Infect Dis 2003; 37: 1014–1020.

68. Faust WC, Diaz M, Pohl HG. Incidence of post-pyelonephritic renal scarring: a meta-analysis of the dimercapto-succinic acid literature. J Urol 2009; 181: 290–298.

69. Hitzel A, Liard A, Vera P, Manrique A, Menard JF, Dacher JN.

Color and power Doppler sonography versus DMSA scintigraphy in acute pyelonephritis and in prediction of renal scarring. J Nucl Med 2002; 43(1): 27–32

70. Supavekin S, Surapaitoolkorn W, Pravisithikul N, Kutanavanishapong S, Chiewvit S. The role of DMSA renal scintigraphy in the first episode of urinary tract infection in childhood. Ann Nucl Med 2013; 27: 170–176.

71. Lee BE, Seol HY, Kim TK, Seong EY, Song SH, Lee DW, Lee SB, Kwak IS. Recent clinical overview of renal and perirenal abscesses in 56 consecutive cases. Korean J Intern Med 2008; 23(3): 140–148.

72. Piccoli G, Consiglio V, Deagostini MC, Serra M, Biolcati M, Ragni F, Biglino A, De Pascale A, Frascisco MF, Veltri A et al. The clinical and imaging presentation of acute "non complicated" pyelonephritis: a new profile for an ancient disease. BMC Nephrol 2011; 12: 68.

73. Sato M, Suzuki S, Shimada S, Yamamoto S, Taketazu G, Mukai T, Taketazu M, Sakata H, Oki J. Serial sonographic findings during progression from acute pyelonephritis to renal abscess: a rare case report. CEN Case Reports 2017; 6: 8–21.

74. Morehouse HT, Weiner SN, Hoffman C. Imaging in inflammatory disease of the kidney. AJR 1984; 143: 135–141.

75. Zissin R, Gayer G, Kots E, Werner M, Shapiro-Feinberg M, Hertz M. Iliopsoas abscess: a report of 24 patients diagnosed by CT. Abdom Imaging 2001; 26: 533–539.

76. Brown ED, Brown JJ, Kettritz U, Shoenut JP, Semelka RC. Renal abscesses: appearance on gadolinium-enhanced magnetic resonance images. Abdom Imaging 1996; 176: 172–176.

77. Gerzof SG, Robbins AH, Birkett DH. Computed tomography in the diagnosis and management of abdominal abscesses. Abdom Imaging 1978; 3: 287–294.

78. Hoffer FA, Shamberger RC, Teele RL. Ilio-psoas abscess: diagnosis and management. Pediatr Radiol 1987; 17: 23–27.

79. Unal O, Koparan HI, Avcu S, Kalender AM, Kisli E. The diagnostic value of diffusion-weighted magnetic resonance imaging in soft tissue abscesses. Eur J Radiol 2011; 77: 490–494.

80. Olvera-Posada D, Armengod-Fischer G, Vazquez-Lavista LG, Maldonado-Avila M, Rosa-Nava E, Manzanilla-Garcia H, Castillejos-Molina RA, Mendez-Probst CE, Sotomayor M, Feria-Bernal G et al. Emphysematous pyelonephritis: multicenter clinical and therapeutic experience in Mexico. Urology 2014; 83(6): 1280–1284.

81. Lu YC, Chiang BJ, Pong YH, Huang KH, Hsueh PR, Huang CY, Pu YS. Predictors of failure of conservative treatment among patients with emphysematous pyelonephritis. BMC Infect Dis 2014; 14: 418.

82. Sanford TH, Myers F, Chi T, Bagga HS, Taylor AG, Stoller ML. Emphysematous pyelonephritis: the impact of urolithiasis on disease severity. Transl Androl Urol 2016; 5(5): 774–779.

83. Bjurlin MA, Hurley SD, Kim DY, Cohn MR, Jordan MD, Kim R, Divakaruni N, Hollowell CMP. Clinical outcomes of nonoperative management in emphysematous urinary tract infections. Urology 2012; 79(6): 1281–1285.

84. Aswathaman K, Gopalakrishnan G, Gnanaraj L, Chacko NK, Kekre NS, Devasia A. Emphysematous pyelonephritis: outcome of conservative management. Urology 2008; 71 (6): 1007–1009.

85. Allen HA, Walsh JW, Brewer WH, Vick CW, Haynes JW. Sonography of emphysematous pyelonephritis. J Ultrasound Med 1984; 3: 533–537.

86. Narlawar RS, Raut AA, Nagar A, Hira P, Hanchate V, Asrani A. Imaging features and guided drainage in emphysematous pyelonephritis: a study of 11 cases. Clin Radiol 2004; 59: 192–197.

87. Wan YL, Lee TY, Bullard MJ, Tsai CC. Acute gas-producing bacterial renal infection: correlation between imaging findings and clinical outcome. Radiology 1996; 198(2): 433-438.

88. Huang JJ, Tseng CC. Emphysematous pyelonephritis. Clinicoradiological classification, management, prognosis and pathogenesis. Arch Intern Med 2000; 160(6): 797-805.

89. Kua CH, Abdul Aziz YF. Air in the kidney: between emphysematous pyelitis and pyelonephritis. Biomed Imaging Interv J 2008; 4(3): e24.

90. Hodson CJ. The radiological diagnosis of pyelonephritis. Proc R Soc Med 1959; 52: 669–672.

91. Hodson CJ. The radiology of chronic pyelonephritis. Postgrad Med J 1965; 41: 477–480.

92. Kay CJ, Rosenfield AT, Taylor KJW, Rosenberg MA. Ultrasonic characteristics of chronic atrophic pyelonephritis. AJR 1979; 132 : 47–49.

93. Tchakarski V, Mushmov D. Potentials of ultrasonography for early diagnosis of primary chronic pyelonephritis. Int Urol Nephrol 1988; 20(6): 665–667.

94. Schneider M, Becker JA, Staiano S, Campos E. Sonographic-radiographic renal and perirenal correlation infections. AJR 1976; 127: 1007–1014.

95. Rosenfield T, Siegel NJ. Renal parenchymal disease: histopathologic-sonographic correlation. AJR 1981; 137: 793-798.

96. Rosenfield AT. Ultrasound evaluation of renal parenchymal disease and hydronephrosis. Urol Radiol 1982; 4: 125–133.

97. Quaia E, Bertolotto M. Renal parenchymal diseases: is characterization feasible with ultrasound? Eur Radiol 2002; 12: 2006–2020.

98. Mostbeck GH, Kain R, Mallek R, Derfler K, Walter R, Havelec L, Tscholakoff D. Duplex Doppler sonography in renal parenchymal disease. J Ultrasound Med 1991; 10: 189–194.

99. Gigante A, Barbano B, Di Mario F, Rosato E, Simonelli M, Rocca AR, Conti F, Ceccarelli F, Giannakakis K, Valesini G et al. Renal parenchymal resistance in patients with biopsy proven glomerulonephritis: correlation with histological findings. Int J Immunopathol Pharmacol 2016; 29(3): 469–474.

100. Yura T, Yuasa S, Sumikura T, Takahashi N, Aono M, Kunimune Y, Fujioka H, Miki S, Takamitsu Y, Matsuo H. Doppler sonographic measurement of phasic renal artery blood flow velocity in patients with chronic glomerulonephritis. J Ultrasound Med 1993; 4: 215–219.

101. Nestola M, De Matthaeis N, Ferraro PM, Fuso P, Constanzi S, Zannoni GF, Pizzolante F, Quadra SV, Gambaro G, Rapaccini GL. Contrast-enhanced ultrasonography in chronic glomerulonephritides: correlation with histological parameters of disease activity. J Ultrasound 2018; 21: 81–87.

102. Xu B, Jiang G, Ye J, He J, Xie W. Research on pediatric glomerular disease and normal kidney with shear wave based elastography point quantification. Jpn J Radiol 2016; 34: 738–746.

103. Feng Q, Ma Z, Wu J, Fang W. DTI for the assessment of disease stage in patients with glomerulonephritis - correlation with renal histology. Eur Radiol 2015; 25: 92–98.

104. Hauger O, Grenier N, Deminere C, Lasseur C, Delmas Y, Merville P, Combe C. USPIO-enhanced MR imaging of macrophage infiltration in native and transplanted kidneys: initial results in humans. Eur Radiol 2007; 17: 2898–2907.

# Application of Magnetic Resonance Imaging and Computer Vision Technologies for Analysis of Knee Articular Cartilage Degeneration

**Artjoms Suponenkovs[1], Ardis Platkajis[2], Zigurds Markovics[1]**

[1]*Faculty of computer science and information technology, Riga Technical University, Riga, Latvia*

[2]*Medical Academy of Latvia, Riga, Latvia*

**ABSTRACT**

**Introduction:** There is a growth in the number of people with osteoarthritis. Consequently, the analysis of knee articular cartilage degeneration by magnetic resonance imaging data is very important. The magnetic resonance imaging data of a knee contains a lot of information. Unfortunately, a radiology technologist who uses simple (grayscale) images can analyze only a small part of knee data. The aim of the proposed methods is to provide more information about knee articular cartilage.

**Materials and Methods:** This paper proposes methods for visualization of knee cartilage, segmentation of knee tissues and analysis of cartilage changes.

**Results:** The experimental part contains the results and descriptions of visualization, segmentation and analysis methods.

**Conclusions:** The proposed methods and data obtained from cartilage experiments can be useful for diagnosing osteoarthritis, which will allow starting treatment earlier and therefore reducing the risk of cartilage destruction.

***Keywords:*** medical imaging; knee-joint; computer vision; osteoarthritis; image pre-processing; magnetic resonance imaging; image segmentation; tissue analysis; DICOM.

## INTRODUCTION

Today there is a remarkable growth in the number of people with osteoarthritis(OA)[1] in response to decreasing human physical activity. In osteoarthritis, the knee cartilage becomes thin, worn or torn [2]. Therefore, the analysis of knee articular cartilage degeneration by magnetic resonance imaging data is very important. Magnetic resonance imaging (MRI) is used to analyze and display knee articular cartilage. A knee MRI scanning result contains a lot of information. A radiology technologist which uses simple (grayscale) images can see and analyze only a small part of the knee MRI scanning information. This makes it very difficult for a technologist to make an early osteoarthritis diagnosis. The aim of this work is to provide more information about the soft tissues of the knee, using computer vision technologies. Computer vision technologies make it possible to analyze all of the knee MRI scanning information. This analysis can be helpful for early diagnosis of osteoarthritis.

Ramifications of OA are very dangerous: limiting the range of movement, pain and other problems. It is moreover important to start treatment of OA as soon as possible. The early OA detection gives a chance to completely cure osteoarthritis. The early OA detection is rendered difficult for a radiology technologist which uses simple (grayscale) images. The aim of this work is to help the radiology technologist make the right OA diagnosis with the help of computer vision technologies. To reach this aim, it is useful to solve three problems (Fig. 1): the visualization of a knee MRI scanning result - displaying the important information about knee cartilage for radiology technologist; the automatic/semi-automatic tissue segmentation - knee tissue segmentation for further analysis; the tissue analysis - get the quantitative information about the condition of knee tissues.

**Fig. 1. Flowchart of analysis of knee articular cartilage degeneration**

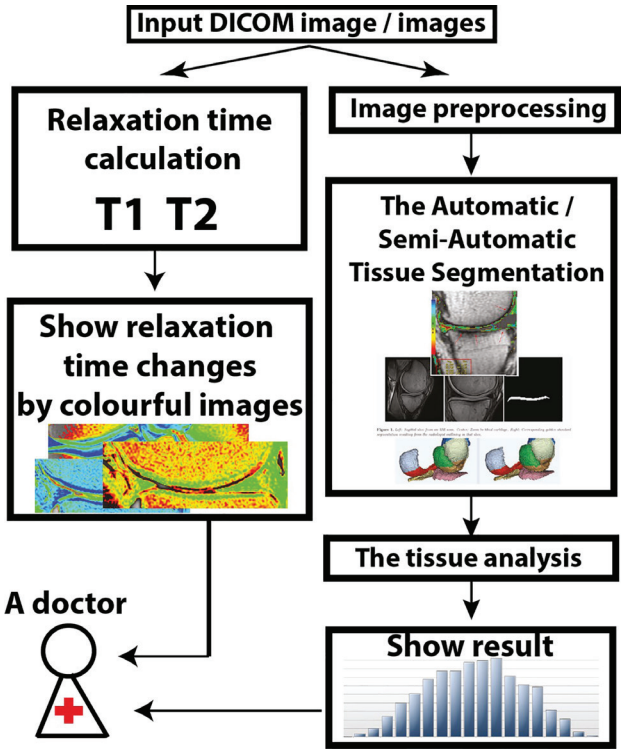


## MATERIALS AND METHODS

Usually the result of MRI scanning is saved in the DICOM (Digital Imaging and Communications in Medicine) file. This file contains a knee image of signal intensities. This image of signal intensities is the main source of information for tissue analysis [3]. The range of signal intensity values is very wide: from 0 to 6 000 (sometimes reaching 15 000). However, this image has to be converted in order to display signal intensities on computer. The result of this conversion is a grayscale image. Grayscale image values are in the range from 0 to 255. Therefore, the grayscale image shows only a small part of knee MRI scanning information. However, it is possible to show more information about knee tissues by using color image. Color image values are in the range from 0 to 16 777 215. It is important to choose the most appropriate color model, keeping in mind the human perception of color [4]. One of the appropriate color systems is hue-saturation-value (HSV) color model. Special visualization methods of a knee MRI scanning result can be useful for displaying signal intensities.

The automatic / semi-automatic tissue segmentation is an important and complicated task. Tissue segmentation makes it possible to analyze different tissues. This segmentation can be helpful for 3D reconstruction of knee tissue. Today there are many methods for segmentation: k-means clustering [5], watershed segmentation [6], active contour segmentation [7] and other methods. It is possible to separate different tissues in an image, by using a combination of these methods. Each tissue type has a unique texture. Therefore, knee tissue segmentation results could be improved by textural tissue features analysis. Textural tissue analysis can be performed by analyzing spatial frequencies, statistical characteristics and structural elements.

After tissue segmentation, it is possible to make separate tissue analysis that is based on physical and biochemical tissue features, biological information of knee structure. This type of analysis identifies the tissue anomalies, pathology. Therefore, it is possible to define knee articular cartilage degeneration by using quantitative information about knee tissues condition.

**The are 5 grades of OA [8,9] by Outerbridge classification. Each grade has a unique visual symptom:**

0) Normal cartilage;
1) Cartilage softening;
2) Loss of <50% cartilage thickness;
3) Loss of > 50% cartilage thickness;
4) Cartilage loss.

Early diagnosis of OA is very important, since it is necessary to start OA treatment as soon as possible. However, it is hard to detect the first grade (cartilage softening) by MRI. Therefore, we were trying to find additional symptoms of the first grade. It is possible to use additional information about biochemical tissue features. **The first grade has additional MRI symptoms [10]:**

1) Increased proton density (where proton density – is the number of hydrogen resonating protons per unit of volume);
2) Increased T1rho relaxation time (where relaxation time – is the recovery time of the proton spin magnetization after RF exposure);
3) Increased T2 relaxation time.

These symptoms make it possible to detect the first grade.

## RELAXATION TIME CALCULATION

MRI scanning result is an image of signal intensities. This scanning result makes it possible to calculate relaxation time. The relaxation time can be calculated by one, two or more MRI images.
The T1 and T2 relaxation times calculation by one MRI image is not precise. However, this approximate method can be useful for relaxation time comparison of different knee tissue segments.
The relaxation times calculation by two MRI images is more precise than the previous method. However, for this method it is necessary to get more scanning information than in the previous method.
The relaxation time calculation by many MRI images allows modulate relaxation process [11]. For this method it is necessary to get 7 or 8 images that display the same knee slice. These images have different TE (T2 relaxation time calculation) or TR (T1 relaxation time calculation) parameters. It is possible to calculate T2 and T1 relaxation time by using partial derivatives and the least square method (1).

$$S(P1,P2) = \sum_{i=1}^{n}(S_i - P1*\exp(\frac{-TE_i}{P2}))^2 \to \min$$

$$\begin{cases} \frac{\partial S}{\partial P1} = \\ -2\sum_{i=1}^{n}(e^{\frac{-TE_i}{P2}}*(S_i - P1*e^{\frac{-TE_i}{P2}})) = 0 \\ \frac{\partial S}{\partial P2} = \\ -\frac{2}{P2^2}*P1*\sum_{i=1}^{n}(e^{\frac{-TE_i}{P2}}*(S_i - P1*e^{\frac{-TE_i}{P2}})*TE_i) = 0 \end{cases}$$

Where:
S – MRI signal,
P1 – initial magnetization (M0),
P2 – relaxation time (T2),
SI – intensity value of image pixel,
TE – Echo Time,
n – Count of images.

Visualization of a knee MRI scanning result
Visualization of a knee MRI scanning result makes it possible to show more information about knee tissues by using color images. The task of visualization is to convert intensity or relaxation time values into the color image. Therefore, each value has an appropriate color. For this purpose, it is possible to use the function (2). This function changes the parameter of a color model (CMP). Change of a parameter depends on the values of intensities or relaxation times.

$$CMP = CR_{MIN} + VALUE * STEP$$

Where CMP – modifiable parameter of color model;
CRMIN – minimal CMP value;
VALUE - value of intensity or relaxation time;
STEP – the ration of CMP range to value range (equation 3).

$$STEP = \frac{CR_{MAX} - CR_{MIN}}{VR_{MAX} - VR_{MIN}}$$

Where CRMAX – maximal CMP value;
VRMAX – maximal visualization value;
VRMIN – minimal visualization value.
The color image of the scanning result depends on the color model. There are 2 color models used in this work. The color model allows converting MRI signal value to color. BGRA model contains 4 components: blue, green, red, alpha. It is not difficult to display the BGRA information on the RGB-screen. However, HSV model is closer to the human perception of color than BGRA model. Therefore, HSV to RGB conversion is required for the visual display of HSV information. HSV model contains 3 components: hue, value, saturation. There are 4 display modes in this work (Fig. 2.).
1) BLUE RED: BGRA model – color range is CRMAX = 500, CRMIN = 0; modifiable parameters (CMP) are blue and red components.
2) FULL HUE: HSV (hue, saturation value) model - color range is CRMAX = 360, CRMIN = 0; modifiable parameters (CMP) is the hue component.
3) BLUE GREEN RED: HSV model – color range is CRMAX = 250, CRMIN = -10; modifiable parameters (CMP) is hue.
4) GREEN RED: HSV model – color range is CRMAX = 150, CRMIN = -30; CMP is hue.

**Fig. 2. Display modes of MRI scanning result**

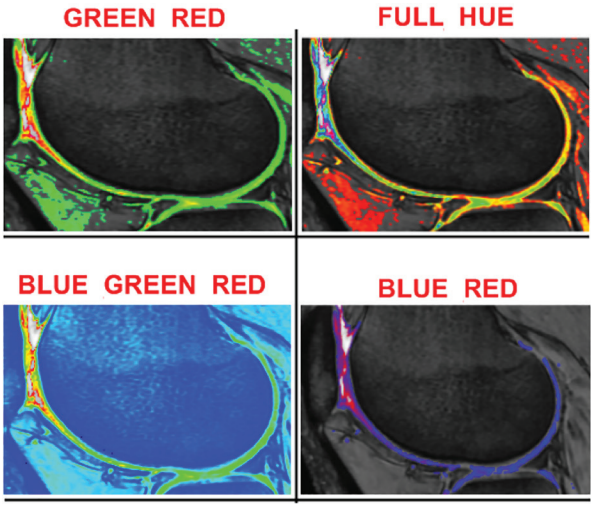


**The value range (VRMAX - VRMIN) depends on the power of the MRI magnet. For example:**
1) Power of MRI magnet is 1.5 Tesla - range of signal intensities is 0 – 6000;
2) Power of MRI magnet is 3 Tesla – range of signal intensities is 0 – 9000.
**After relaxation time calculation, it is possible to get ranges of relaxation times:**
1) Range of relaxation time T1 – is 0...6000 ms (3 Tesla);
2) Range of relaxation time T2 – is 0…2000 ms.
Sometimes, it is necessary to show only one type of tissues (for example cartilage), in this case, it is possible to decrease value range. This minimization, in turn, has made it possible to show more information about the proper tissue.

## IMAGE PREPROCESSING AND SEGMENTATION OF A KNEE MRI SCANNING RESULT

The image segmentation makes it possible to perform an analysis of knee. However, segmentation is a very complicated task, because MRI image contains a lot of information. Therefore, it is important to remove unnecessary information from MRI image. For this purpose, it is possible to use image preprocessing (Fig.3).
There are two types of image preprocessing used in this work: Perona – Malik filter [12] and Sobel operator. Perona – Malik filter is an anisotropic diffusion that removes high frequency components (noise, small details). This filter has an advantage that it does not remove borders of

**Fig. 3. Two types of MRI image preprocessing**

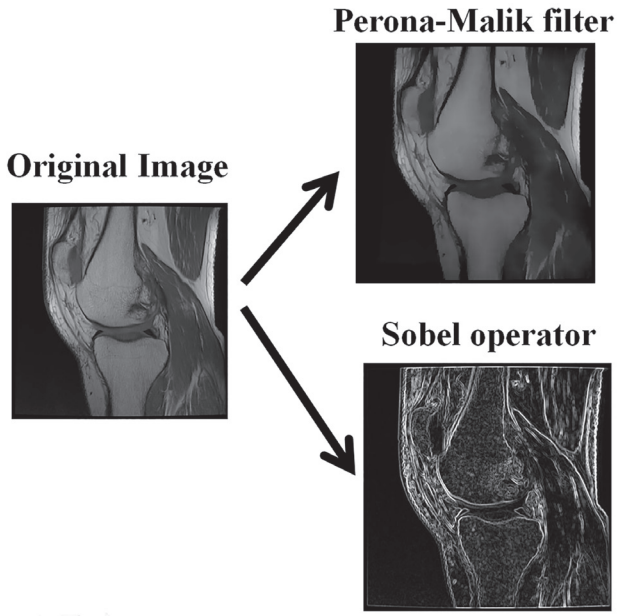


large segments. Therefore, Perona – Malik filter prepares MRI image for further segmentation. The anisotropic diffusion is described with the equation (4):

$$I_t(x,y,t) = div(c(x,y,t)\nabla I(x,y,t)$$

Where
c - Special diffusion coefficient;
I - smoothing image (the level of smoothing of the image depends on the t parameter);
div - divergence;

## IT - RESULTING IMAGE.

As shown in Figure 4, combination of two methods (Perona – Malik filter and K-means clustering [13]) provided good segmentation results.
The second segmentation type is watershed segmentation [14]. As shown in Figure 4, this segmentation works well together with Sobel operator. However, the result of watershed segmentation contains a lot of tiny segments. This problem can be solved by using additional information about knee.
Sometimes, it is necessary to improve the accuracy of segmentation. For this reason, knee tissue segmentation results could be improved by textural tissue features analysis. Textural tissue features analysis can be performed by using a co-occurrence matrix [15].

**Fig. 4. Two types of MRI image segmentation**

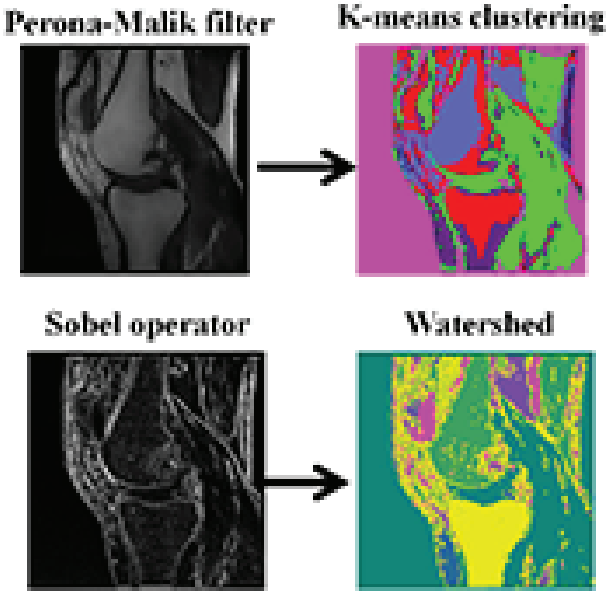


## THE TISSUE ANALYSIS

After automatic / semi-automatic tissue segmentation is finished, it is possible to perform knee analysis. The goal of this analysis is to detect the OA symptoms. There are many visual symptoms of OA: synovial effusion, eroded cartilage, narrowed joint space, subchondral bone lesion, osteophyte, inflamed synovium. However, these are symptoms of OA 2-4 grades. The first grade of OA is of most interest in respect to treatment benefits. The first grade is very important because at this stage it is possible to completely cure OA. However, there are no perceptible visual changes of a knee at this stage. Therefore, biochemical changes of a knee must be taken into account. There are some biochemical and physical changes of cartilage tissue at this stage: increase in the water content in cartilage; development of surface fibrillation; destruction of collagen fibers; increase in the T1rho, T2 and proton density. These changes of cartilage tissue have an influence on the intensities of cartilage tissue. For this reason, it is possible to analyze intensities of cartilage tissue by calculating the dispersion (5) and histogram.

$$D = \overline{X^2} - (\overline{X})^2$$

$$\overline{X} = \frac{1}{n}\sum_{i=1}^{n} X_i$$

$$\overline{X^2} = \frac{1}{n}\sum_{i=1}^{n} X_i^2$$

$$\sigma = \sqrt{D}$$

Where

D – Dispersion of cartilage pixel intensities;

– Arithmetic mean of cartilage pixel intensities;

– Arithmetic mean of square cartilage pixel intensities;

n – Pixel count;

σ – Standard deviation.

## RESULTS

### RESULTS OF VISUALIZATION METHODS

Experiments were performed with special visualization methods, aiming to look for cartilage degeneration by using HSV and BGRA color models. These matching experiments used 5 display modes: MRI original image (monochrome), Blue Red (BGRA model), Full Hue (HSV model), Blue Green Red (HSV model), Green Red (HSV model). The results of these experiments (fig. 5) show that the highest number of observable changes of cartilage has been in HSV and BGRA color models. The Full Hue display mode has the best result because of the wide range of hue values. These experiments were performed using 19 different MRI images.

**Fig. 5. Evaluation of visualization methods**

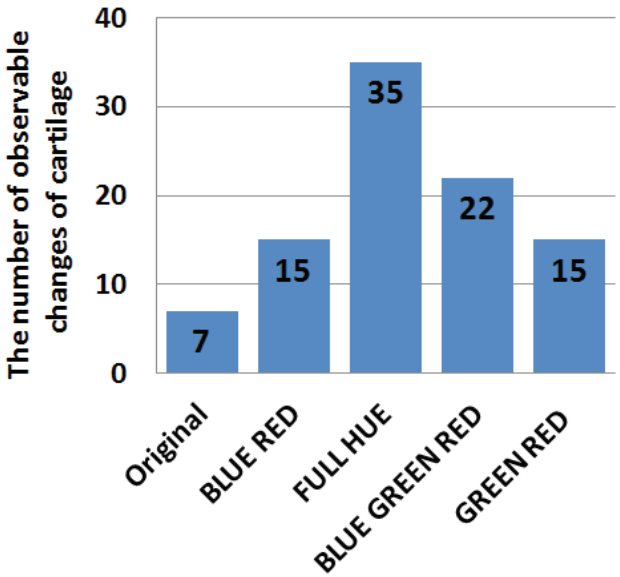

## RESULTS OF SEGMENTATION

Experiments were performed with k-means clustering and watershed segmentation (fig. 4). The results showed that the combined use of Perona – Malik filter and k-means clustering provide the most effective tissue segmentation. The results showed that some tissues are difficult to separate from each other. Therefore, additional textural tissue features analysis should be used.

## RESULTS OF TISSUE ANALYSIS

The aim of this experiment is to compare the intensity dispersion of healthy and damaged cartilages. For these comparative experiments, proton density (PD) fat-suppressed (FS) MRI sequence was used. The MRI sequence TE and TR parameters have the following values:
1) TE - from 26 to 29;
2) TR - from 2923 to 3170.
The results of cartilage tissue analysis (fig. 6) show that a healthy patient (green color P2 and P5) has lesser standard deviation of cartilage signal intensity values than patients with OA (red color P1, P3, P4, et al.).

**Fig. 6. Standard deviation of cartilage pixel intensities**

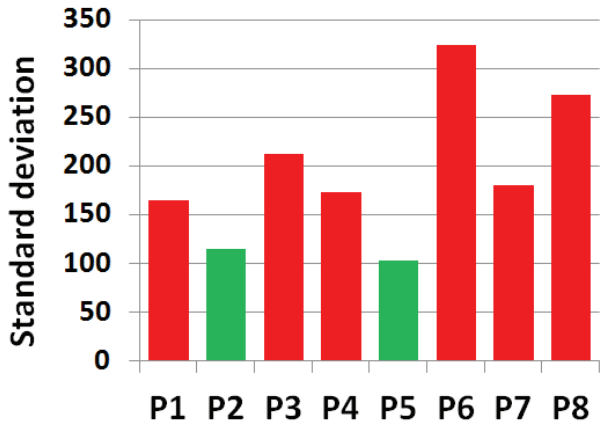


## CONCLUSION

Results of visualization methods show that the use of HSV and BGRA model provides the most effective visualization of the cartilage degeneration. Moreover, the Full Hue display mode is the most sensitive to changes in cartilage intensity values. Results of tissue analysis show that the intensity dispersion and intensity standard deviation of cartilage can help with the OA detection. The above-mentioned methods and results can be useful for OA diagnosis, which allows starting treatment earlier and therefore reduces the risk of cartilage destruction.

## REFERENCES

1. Ian J. Wallace, Steven Worthington, David T. Felson, et al. Knee osteoarthritis has doubled in prevalence since the mid-20th century. Proc Natl Acad Sci U S A. 2017 Aug 29; 114(35): 9332–9336.

2. Alice Roberts. The complete human body. Penguin Random House. 2016.

3. Mario Mustra, Kresimir Delac, Mislav Grgic. Overview of the DICOM Standard. 50th International Symposium ELMAR-2008, 10-12 September 2008, Zadar, Croatia.

4. Michael A Webster. Human colour perception and its adaptation. Computation in Neural Systems 7 (1996) 587–634.

5. Kalpana Shrivastava, Neelesh Gupta, Neetu Sharma. Medical Image Segmentation using Modified K Means Clustering. International Journal of Computer Applications. Volume 103 – No 16, October 2014.

6. Dibyendu Goshal, Pinaki Pratim Acharjya. MRI Image Segmentation Using Watershed Transform. International Journal of Emerging Technology and Advanced Engineering. ISSN 2250-2459, Volume 2, Issue 4, April 2012.

7. Amira Ben Rabeh, Faouzi Benzarti, Hamid Amiri. Segmentation of Brain MRI Using Active Contour Model. National Engineering School of Tunis (ENIT), Signal, Image and Technology Information (LR-SITI), Manar, Tunisia, 2016.

8. Helmtrud I. Roach and Simon Tilley. The Pathogenesis of Osteoarthritis. Bone and Osteoarthritis. Springer. 2007.

9. Magdalena Posadzy, Julie Desimpel, Filip M Vanhoenacker. Staging of Osteochondral Lesions of the Talus: MRI and Cone Beam CT. December 2017.

10. Nasnikova I.U., Morozov S.P., and Filisteev P.A.. Magnetic resonance tomography: quantitative assessment methods in articular cartilage structure analysis of in patients with osteoartrosis. Russian Electronic Journal of Radiology 1 75-81

11. Bruce C. Po.. Graphical Interface for Quantitative T1 and T2 Mapping of MRI Data (Massachusetts Institute of Technology) p 119

12. Caio A. Palma, Fabio A.M. Cappabianco, Jaime S. Ide, Paulo A.V. Miranda. Anisotropic Diffusion Filtering Operation and Limitations - Magnetic Resonance Imaging Evaluation. The International Federation of Automatic Control, Cape Town, South Africa. August 24-29, 2014.

13. Kalpana Shrivastava, Neelesh Gupta, Neetu Sharma. Medical Image Segmentation using Modified K Means Clustering. International Journal of Computer Applications (0975 – 8887) Volume 103 – No 16, October 2014.

14. V. Grau, A. U. J. Mewes, M. Alcaniz, R. Kikinis, S. K. Warfield. Improved Watershed Transform for Medical Image Segmentation Using Prior Information. IEEE Transactions on medical imaging, vol. 23, 2004.

15. Lidong Fu and Bin Zhang. A Co-Occurrence Matrix Algorithm Used for Medical Image. International Conference on Computer Science and Network Technology, 2011.

# Positron emission tomography/computer tomography in the evaluation of head and neck cancer treatment

**Severina Šedienė[1], Ilona Kulakienė[1], Viktoras Rudžianskas[2]**

[1]*Lithuanian University of Health Sciences, Medical Academy*

[2]*Lithuanian University of Health Sciences, Oncology Institute*

**ABSTRACT**

The role of 18F-fluorodeoxy-D-glucose positron emission tomography-computed tomography (18F-FDG PET/CT) imaging in head and neck carcinoma (HNC) during pre-treatment staging, treatment response assessment after induction chemotherapy, radiotherapy planning and after entire therapy, follow-up is analyzed with attention on contemporary evidence. The 18F-FDG PET/CT is properly established in staging for distinction of cervical nodal involvement or rejection of distant metastases. Recently, many papers on the assessment of treatment response of 18F-FDG PET/CT have been published. 18F-FDG PET/CT performed in 2 weeks after the completion of induction chemotherapy (ICT) prevents from irrelevant invasive procedures, such as full neck dissection, with a significant impact on clinical outcome. 18F-FDG PET/CT completed in 8 weeks after the radio-chemotherapy treatment also has a high negative predictive value. From another point of view, the low positive predictive value due to feasible post-ICT and radiation therapy inflammation findings needs adequate attention to make a clinical decision. Recently, 18F-FDG PET/CT imaging in head and neck carcinoma has emerged, especially in radiotherapy planning for tumour volume delineation. In the near future, there are some expectations that new PET radiopharmaceuticals would present significant information on specific tumour characteristics, and all possible limitations of 18F-FDG may be avoided.

***Keywords:*** $^{18}$F-FDG, PET/CT, Head and neck cancer

## 1. INTRODUCTION

Head and neck cancer comprises malignancies of the upper aerodigestive tract. Even though the different sites are anatomically very close, their prognosis and response to treatment are surprisingly different. More than 85% of head and neck cancer arise from squamous cells [1]. The five year overall survival (OS) for head and neck cancer patients is quite poor, commonly reported as less than 60%, but with heterogeneity between the head and neck cancer sites [2]. The assessment of the therapy response varies widely between institutions. It usually consists of a combination of clinical evaluation and imaging. In recent years, functional imaging with PET/CT has gradually been incorporated in clinical practice. 18F-FDG PET/CT is applied in various clinical settings, ranging from pre-treatment staging to treatment planning and response assessment after induction chemotherapy or chemo-radiotherapy, as well as post-therapy follow-up [3, 4].

18F-FDG uptake represents glucose metabolism. Most of the cases of glucose metabolism can be visible in the tissue of several organs, for example, brain, liver, kidneys, salivary glands, etc. Although 18F-FDG is the most commonly used PET tracer for oncological purposes, its use in HNC suffers from some limitations due to the complex anatomy of this region and the small size of the anatomical structures.

After surgery, chemotherapy or radiotherapy treatment, inflammatory cells could be activated; therefore, they would show increased 18F-FDG uptake, and those PET/CT scans could be interpret as false positive PET results [5]. With all the mentioned limitations, PET/CT imaging is still fast with high resolution images; at the same time, there is a very comprehensive correlation between an anatomical location and function-

al images. This review will focus on the use of 18F-FDG PET/CT in various clinical situations of head and neck cancer.

## 2. PET/CT FOR PRE-TREATMENT STAGING AND METASTATIC DISEASE EVALUATION

In routine clinical practice, HNC patients' diagnostic strategy involves accurate physical examination and endoscopy. Clinical examination usually is followed by several imaging modalities, for instance, neck ultrasound, magnetic resonance imaging (MRI) or contrast-enhanced computer tomography (ceCT) for the evaluation of disease extent or possible second primary tumour.

Precise evaluation of disease extension is significant in planning the most specific treatment, with important findings for patient outcomes. There are few current studies which have shown that 18F-FDG PET/CT is more accurate than conventional imaging in head and neck, and the results make it possible to individualize and change therapeutic management for more than 30% of patients [6-8]. Connell et al. showed that in 34% of patients TNM classification was changed after a PET scan, which had a direct clinical impact on almost half of them [7].

Primary HNC tumour is generally discovered with clinical examination, endoscopy, CT and MRI, despite high sensitivity (> 95%)18F-FDG PET/CT imaging [9]. Standard PET/CT with low-dose non-enhanced CT has its own limitations, especially when there is a need to distinguish the precise location, extent of tumour spread and tumour invasion to adjacent structures. Contrast-enhanced PET/CT just partially can overcome those limitations [8].

PET plays an important role in the detection of primary tumour in case of cancer of unknown origin (CUP). 18F-FDG PET/CT performed for patients with cervical lymph node metastasis without the primary tumour detects primary tumour in about 25–38.5% cases [10, 11].

Patients with advanced disease, particularly with hypopharyngeal carcinomas and nodal involvement, should be checked for distant metastases. The most frequent sites for metastases are lungs, bone and liver (Fig. 1).

**Figure 1. 18F-FDG PET/CT performed at staging in a patient with laryngeal carcinoma. Whole body PET/CT (a) shows intense 18F-FDG uptake of the primary tumour and a right lateral cervical lymphadenopathy (b). In addition, a high 18F-FDG uptake is evident in the first lumbar vertebral body, suggesting a metastatic lesion (c and d)**

**a)**

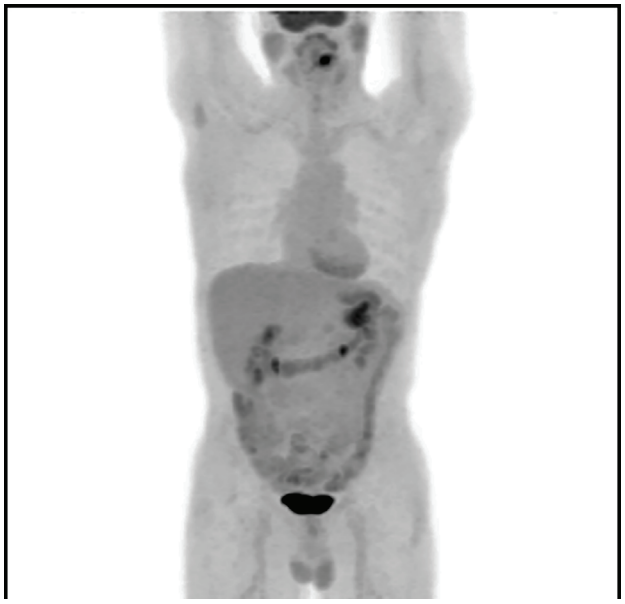

**b)**

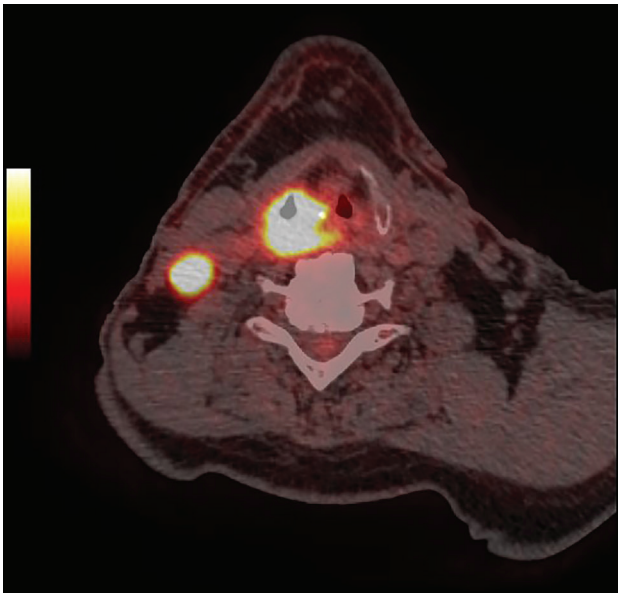

c)

d)

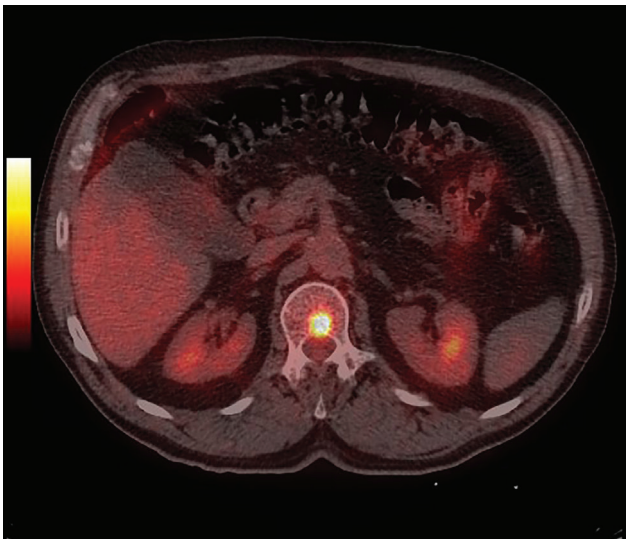

18F-FDG PET/CT has higher accuracy for detection of distant metastasis than CT. Therefore, in around 13% of clinical cases with detected distant lesions, a change in the treatment strategy has resulted in improvement of major outcomes for patient survival [12, 13].

18F-FDG PET/CT is a precise method to determine second primaries, with a high negative predictive value. Also, a relatively lower positive predictive value of PET/CT following inflammation and benign hyperplasia diagnosis was noticed in the head and neck region, which may result in false positive PET findings [14]. Second primary tumors may occur in 5–10% of HNC patients and are more often detected in the head and neck region, esophagus and lungs (Fig. 2).

**Figure 2. 18F-FDG PET/CT performed at staging in a patient with oropharyngeal carcinoma. Whole body PET/CT (a and b) shows intense 18F-FDG uptake in the primary tumour as well as in a gastric mass located in the body segment of the dorso-medial part (c and d). These findings suggest a second primary tumour.**

a)

b)

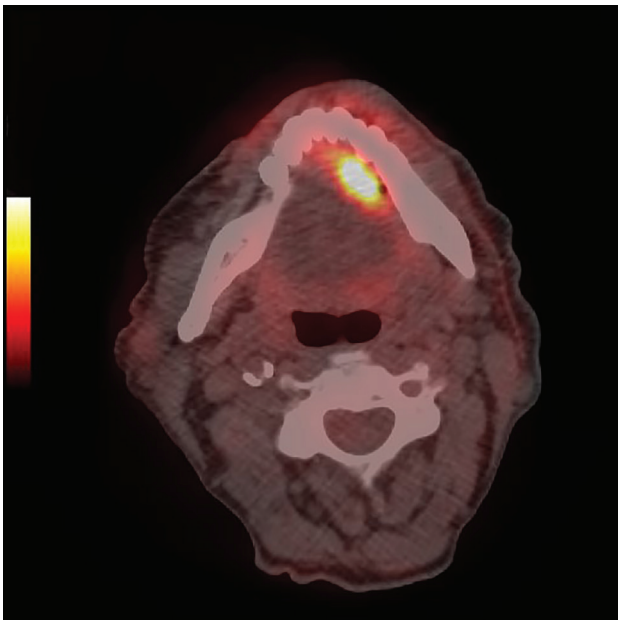

c)

d)

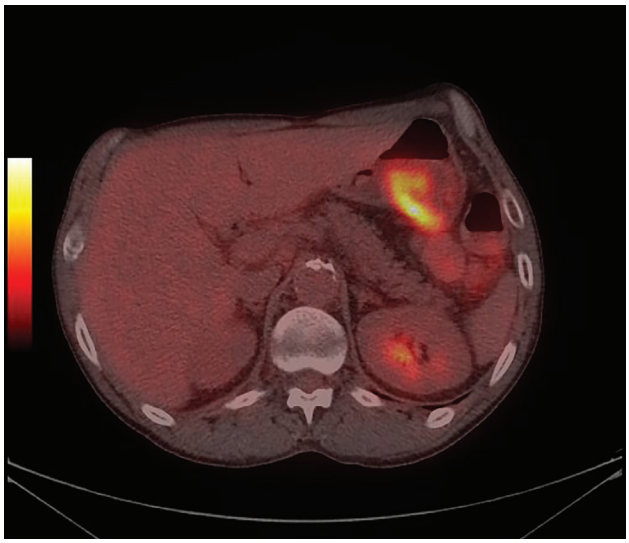

Secondary primary tumours are notably the first cause of death with a decisive impact on overall survival rates of early stage HNC patients [15]. PET/CT by detecting second primary tumour may change the treatment strategy and overall survival of HNC [16].

### 3. CERVICAL LYMPH NODE EVALUATION

In a meta-analysis by Kyzas et al., pretreatment lymph node staging capability was estimated and showed a sensitivity of 79% and a specificity of 86% in patients with different types of HNC [17]. In a one study analysis, it was demonstrated that PET before panendoscopy was cost-effective in N1-N2 tumours [18]. The results of the study suggest that PET should be performed before treatment in advanced stage (III and IV) tumours, tumours with an increased risk of distant metastases and in the diagnosis of CUP [19]. In our institution and mostly in all European centers, the main indication of 18F-FDG PET/CT in newly diagnosed HNC is identification of cervical lymph node involvement. The main disadvantages of these studies are false negative results. However, more and more data from the literature maintain superiority of PET/CT over morphological imaging in lymph node involvement identification [8]. The biggest advantage of functional imaging is that even small or normal size lymph nodes with a typical structure could be detected as metastatic lesions (Fig. 3).

Nevertheless, it should be considered that small lymph nodes may be missed (as a false negative result), and sometimes reactive or inflammatory lymph nodes may accumulate the tracer (possible false positive results). However, PET/CT scanner has its limitation, for example, spatial resolution is limited to 5 mm, and accordingly microscopic disease or metastases could be missed. Thus, an 18F-FDG PET/CT scan without lymph node involvement does not validate a surveillance approach in all cases. The ultimate decision to perform neck dissection in patients with negative morphological and functional imaging still depends mainly on the assessment of risk factors and tumour characteristics [20, 21]. Sentinel lymph node scintigraphy in this case may be a solution.

According to literature, positron emission tomography-magnetic resonance (PET/MR) has higher sensitivity and specificity for nodal involvement (85% and 92%, respectively) than 18F-FDG PET/CT, but spatial resolution has the same limitation for patients with micrometastases [22].

### 3. RADIOTHERAPY PLANNING

Radiation therapy is routinely planned on pre-treatment CT images. Low soft tissue resolution and dental artefacts may especially make the primary tumour delineation difficult. Delineation studies incorporating functional imaging

**Figure 3. 18F-FDG PET/CT performed at staging in a patient with laryngeal carcinoma. Whole body PET/CT (a and b) shows intense 18F-FDG uptake of the primary tumour as well as left side cervical node, which demonstrates a short axis less than 6 mm in the transaxial plane of CT (c and d). These findings have both prognostic and therapeutic implications.**

a)

b)

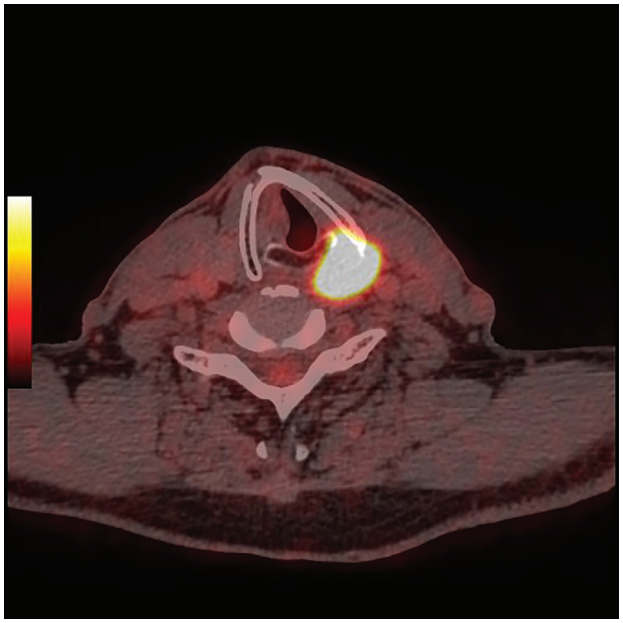

c)

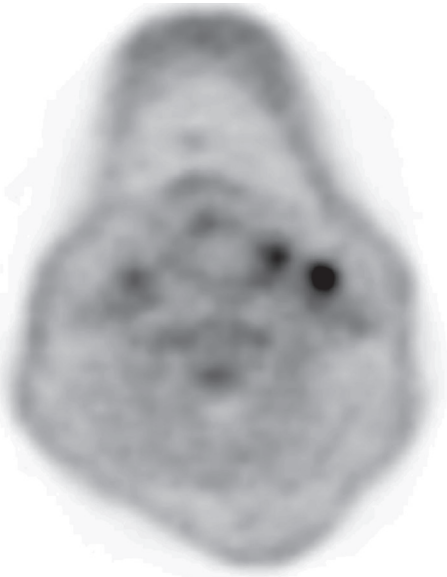

d)

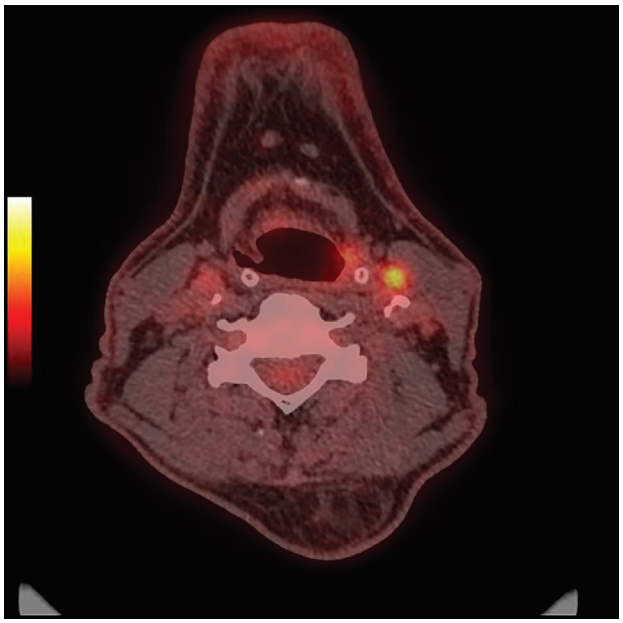

of the primary site have been performed and PET has been shown to be more accurate in defining gross tumour volume (GTV) than CT or MRI alone. However, all modalities have failed to detect superficial tumour extension [23].

18F-FDG PET/CT is a perfect tool for tumour target volume selection with the possibility of reducing the radiotherapy target volume and, therefore, reducing acute or late side effects after the radiotherapy treatment [10, 11]. For precise delineation of target volumes, molecular imaging has better sensitivity and contrast resolution; thus, it is possible to optimize the treatment plan [24]. In one study, GTV delineated by 18F-FDG

PET/CT was significantly smaller than GTV delineated by CT and MRI. It was noticed that GTV delineated by PET/CT was approximately close to the pathologic GTV from a surgical sample [23].
The main limitation of PET/CT is the deficiency of a standardized method for functional volume segmentation [25]. Currently, there are few clinical investigations of 18F-FDG PET/CT for radiotherapy planning experimenting with dose escalation for metabolically active tumours, and in some cases adjusting the radiotherapy plan during treatment [24-26].
Recently, molecular imaging, especially its application in finding out the fundament biological information, has been under investigation. In various trials, new hypoxia-related PET tracers, because of their possibility to recognize the tumour hypoxic region and radiation-resistant tumour within the GTV, are most often involved in the radiation planning process. Those hypoxic cells will be provided with higher doses of radiation [27].

## 4. TREATMENT RESPONSE EVALUATION

A precise assessment of response is substantial in the management of patients with head and neck tumour treated with induction chemotherapy and later on with chemo-radiotherapy. The evaluation of treatment response varies widely between institutions. It usually comprises a combination of clinical evaluation and imaging. Usually, morphological imaging such as MRI, CT or ultrasound can be used. In recent years more centers have started treatment response evaluation after ICT treatment. Later on, functional imaging with PET has gradually been incorporated in the evaluation of therapy response. 18F-FDG PET/CT can identify viable tumour and overcome the most commonly occurring limitations of morphological imaging modalities [28, 29]. However, after radiation therapy, the inflammation process can be very active, which may lead to a high number of false positive findings and a low positive predictive value of PET/CT [30]. By choosing proper timing for PET/CT post-treatment evaluation, it is possible to decrease the number of false positive findings. There is a suggestion that an optimum time to perform 18F-FDG PET/T for patients treated with induction chemotherapy is 10–14 days after treatment and 8–12 weeks after radiotherapy.
In latest treatment planning, patients with a complete metabolic response may avoid neck dissection, despite the presence of remaining node irregularity detected by conventional imaging [31] (Fig. 4).

Although a completely negative PET scan at the end of therapy typically suggests a good prognosis, it does not necessarily correspond to a complete absence of cancer cells, as 18F-FDG PET/CT is unable to discriminate between minimal tumour burden and no tumour burden. Hence, the recognition of different prognostic factors could help to establish high-risk patients who respond poorly to therapy and could benefit from amplification or treatment changing modality. Accordingly, the prognostic value of different 18F-FDG parameters, such as maximum and mean standardized uptake value (SUVmax and SUVmean), total lesion glycolysis (TLG) and metabolic tumour volume (MTV), are analyzed in some clinical trials [32]. Several studies have shown that a reduction of at least 45% of primary tumour MTV or TLG after induction chemotherapy may predict progression free survival in patients with advanced HNC [33, 34]. This enables identification of patients at risk of treatment failure at an early time-point, permitting treatment individualization and consideration of alternative strategies such as radiotherapy dose-escalation or surgery. In some studies, the efficacy of these parameters has been assessed with controversial results [32, 35]. The main deficiency is that different metabolic parameters could change in a few different ways, depending on the calculation and reproducibility model.
The prognostic benefit of 18F-FDG PET/CT, performed at the end of radio-chemotherapy, for regional control and survival has been observed after comparison between post-treatment metabolic response and clinical outcomes. However, some studies have shown controversial results about the role of PET/CT performed early during treatment [5, 36]. Castaldi et al. in his study

**Figure 4. 18F-FDG PET/CT performed at staging (a and b) and after induction chemotherapy (lower panels) in a patient with tongue carcinoma. PET/CT (upper panels) shows intense 18F-FDG uptake of the primary tumour and very faint uptake of the primary tumour in 10 days after induction chemotherapy (c and d). These findings have both prognostic and therapeutic implications.**

a)

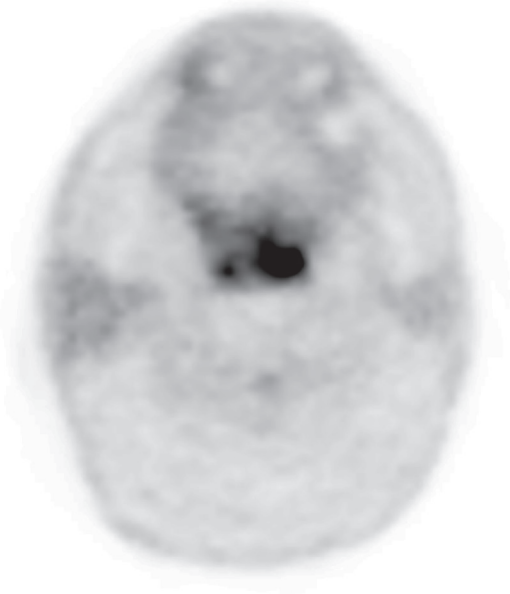

b)

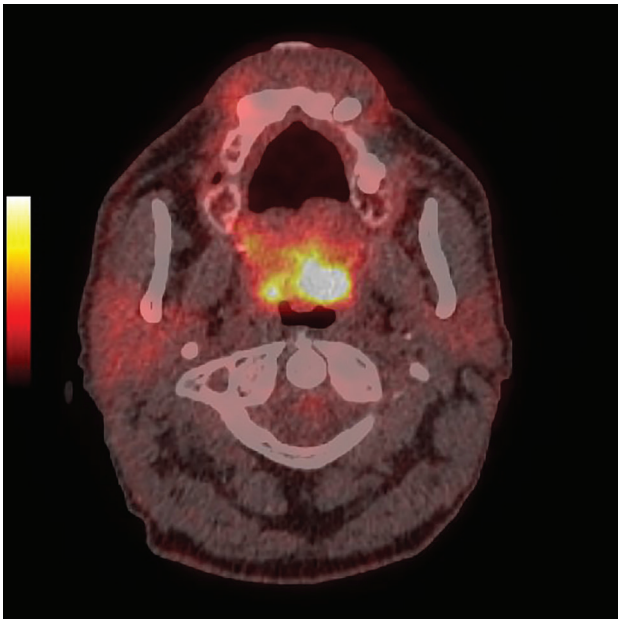

c)

d)

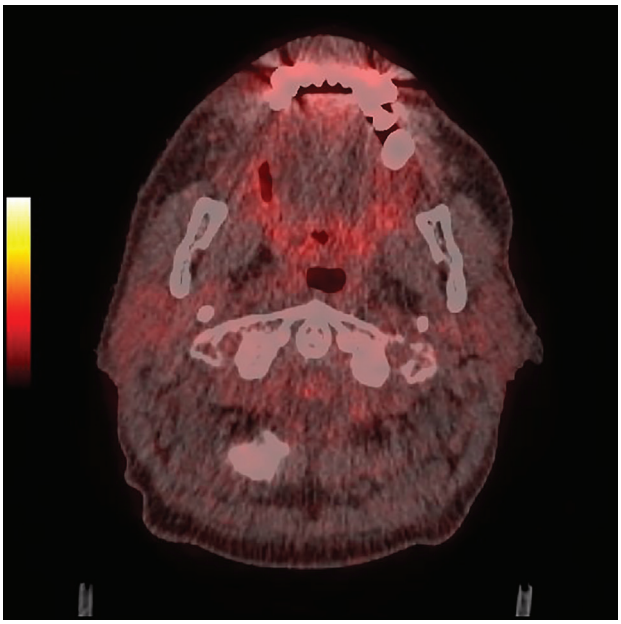

did not find a significant correlation among the "early" changes of FDG uptake in the head and neck tumour and lymph node involvement [36]. In contrast with this study, Hentschel et al. showed that a decrease of 50% or more of SUVmax from the treatment beginning to the first or second week of treatment (10 or 20Gy) was a likely prognostic tool for patients with head and neck cancer [5].

## 5. PET IN THE FOLLOW-UP SITUATION

Even after initial very aggressive treatment, regional or distant recurrence can arise in head and neck cancer patients, particularly during the first year. Salvage therapy and PET/CT might be proper diagnostic tools for early detection of regional disease, herewith changing the survival rate. Detection of recurrence or residual disease with routine imaging, such as CT or MRI, may be complicated because of treatment-induced tissue changes that could be easily misinterpreted with scar tissue, recurrent or residual disease. Several retrospective studies have implied the value of PET/CT in the follow-up, at 3 to 6 and at 12 months post-therapy far exceeding the ability of a physical examination for detection of recurrences with high sensitivity, specificity and predictive values [37]. Mostly asymptomatic recurrences are diagnosed within the first year and almost all within two years, and approximately half of them are distant metastases [38].
It should be considered that when PET/CT is positive, biopsy is suggested due to a moderately high false positive rate according to post-treatment inflammation [8]. In one systematic review, assessing the diagnostic performance of 18F-FDG PET/CT in response evaluation and surveillance, imaging of HNC patients showed a high negative predictive value for the primary site and cervical nodes [39].

## 6. OUR EXPERIENCE

In our hospital, usually pre-treatment 18F-FDG PET/CT evaluation in patients with head and neck cancer who are candidates for surgery is performed. The most significant clinical information coming from this pre-treatment scan is improvement of neck staging and assessment of distant metastases or the second primary tumour. In our opinion, this examination provides a substantial impact on treatment planning.
18F-FDG PET/CT is also performed in patients with cervical squamous cell cancer metastases and unknown primary tumour on a regular basis at our institution.
For treatment response evaluation, an interim PET/CT scan 10–14 days after the end of induction chemotherapy is usually performed. Patients with a complete or partial metabolic response are referred to chemo-radiotherapy. In other cases, the treatment plan is changed by a multidisciplinary team consensus.
During follow-up, particularly in the first year, 18F-FDG PET/CT is performed when morphological imaging results are uncertain or possible recurrence is not detected but diagnosed recurrence will radically change further treatment and prognosis of a patient.

## 7. CONCLUSIONS

18F-FDG PET/CT is very useful for head and neck cancer staging, restaging, induction chemotherapy response assessment and radiotherapy planning, because it is more precise over morphological imaging. Currently, the biggest limitation, particularly in the post-treatment situation, is feasible false positive results because of inflammation and the inability to discover microscopic disease. It is possible that in the future, new tracers other than 18F-FDG, as well as PET/MRI imaging, will provide superior results in various clinical situations.

## APPENDIX B

**Figure A1**

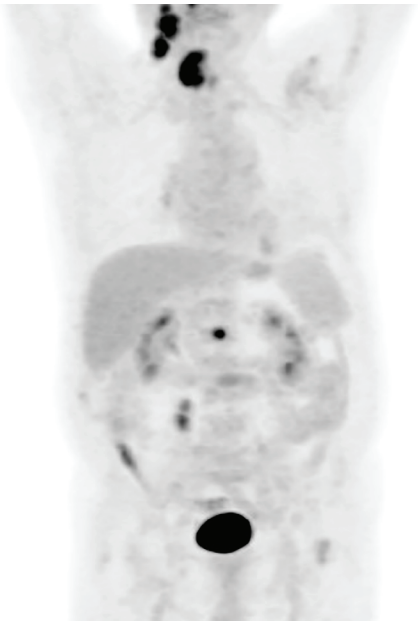

**Figure A2**

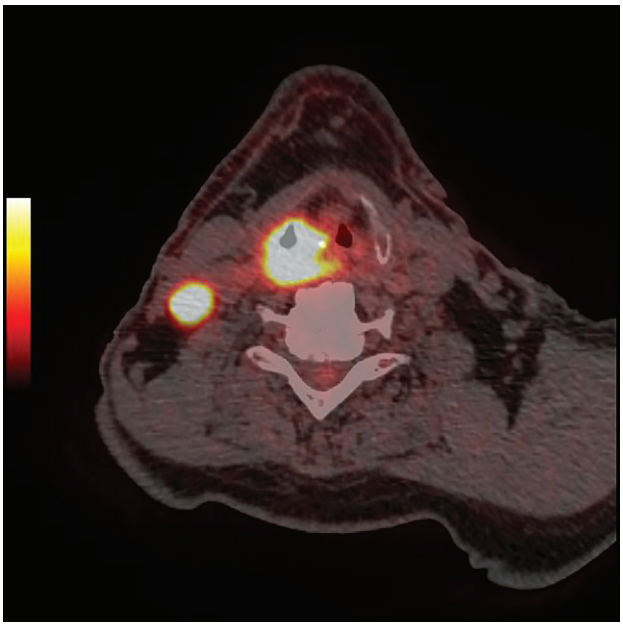

**Figure A3**

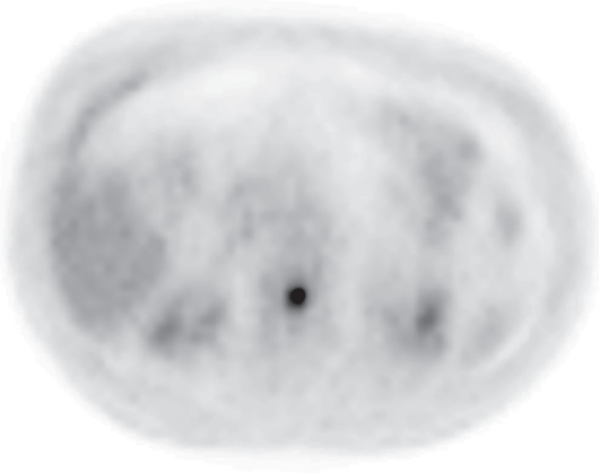

**Figure A4**

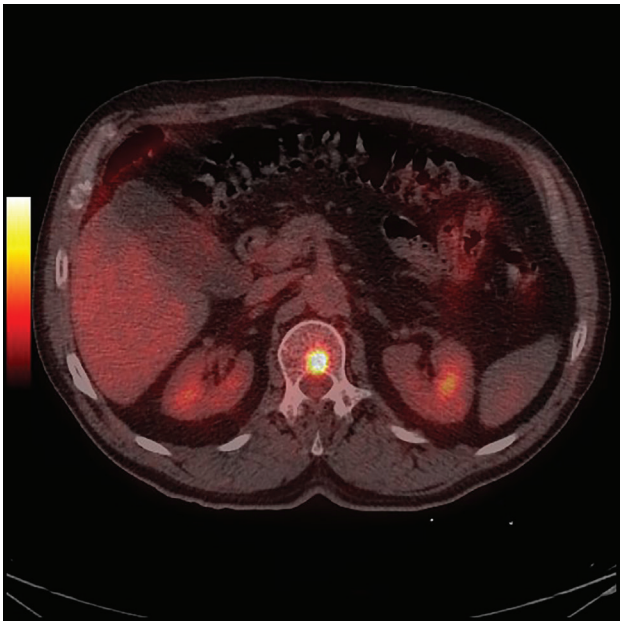

**Figure B1**

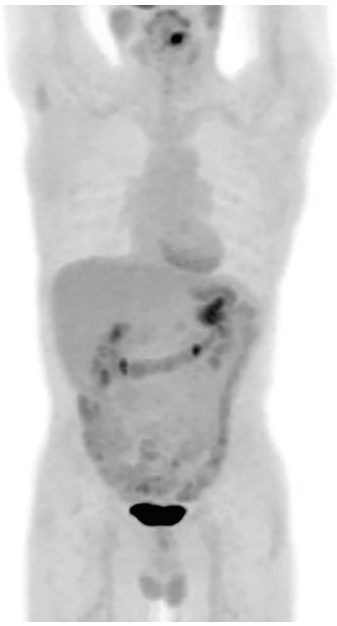

**Figure B2**

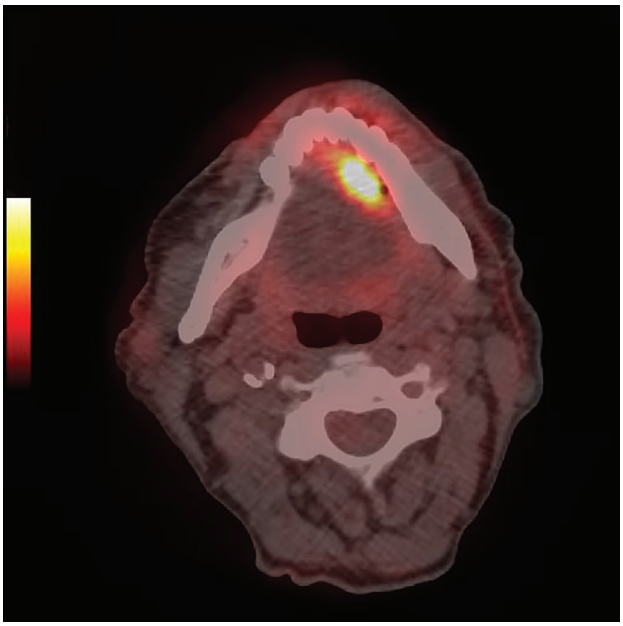

**Figure B3**

**Figure B4**

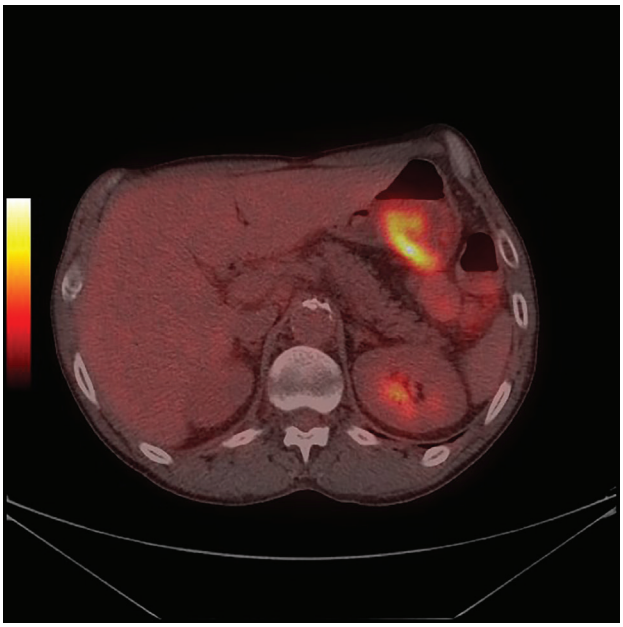

**Figure C1**

**Figure C2**

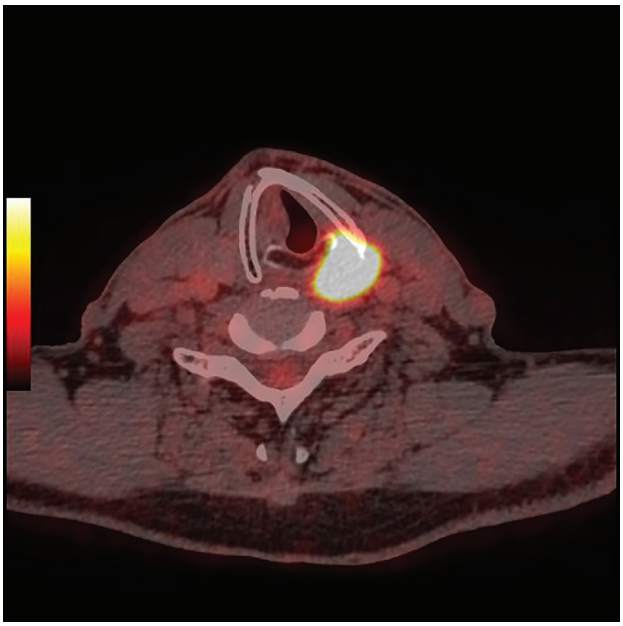

**Figure C3**

**Figure C4**

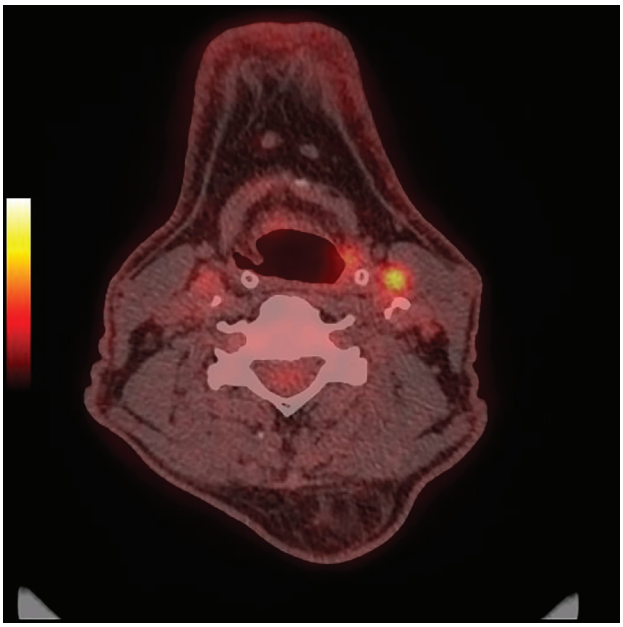

**Figure D1**

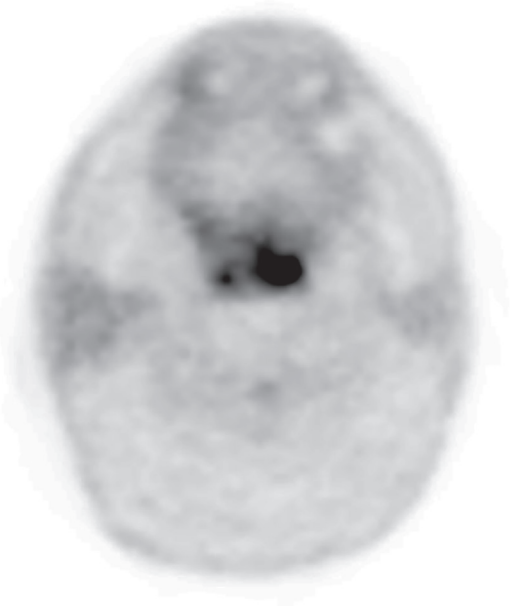

**Figure D2**

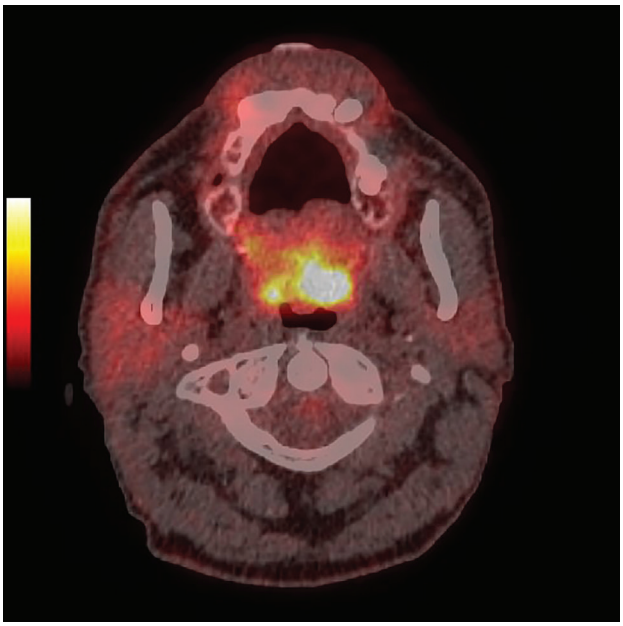

**Figure D3**

**Figure D4**

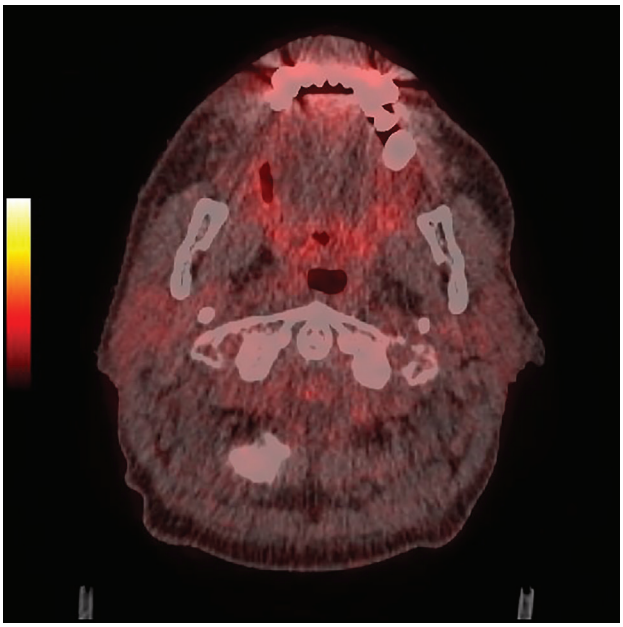

## REFERENCES


1. Mehanna, H., et al., Head and neck cancer–Part 2: Treatment and prognostic factors. Bmj, 2010. 341(c4690): p. 721-725.

2. Pulte, D. and H. Brenner, Changes in survival in head and neck cancers in the late 20th and early 21st century: a period analysis. The oncologist, 2010. 15(9): p. 994-1001.

3. Oyen, W., H. Marres, and J. Kaanders, Progress in nuclear medicine procedures in head and neck oncology. 2011.

4. Corvò, R., Evidence-based radiation oncology in head and neck squamous cell carcinoma. Radiotherapy and Oncology, 2007. 85(1): p. 156-170.

5. Hentschel, M., et al., Serial FDG-PET on patients with head and neck cancer: implications for radiation therapy. International journal of radiation biology, 2009. 85(9): p. 796-804.

6. Czernin, J., M. Allen-Auerbach, and H.R. Schelbert, Improvements in cancer staging with PET/CT: literature-based evidence as of September 2006. Journal of Nuclear Medicine, 2007. 48(1 suppl): p. 78S-88S.

7. A Connell, C., et al., Clinical impact of, and prognostic stratification by, F-18 FDG PET/CT in head and neck mucosal squamous cell carcinoma. Head & neck, 2007. 29(11): p. 986-995.

8. Mak, D., et al., Role of FDG-PET/CT in staging and follow-up of head and neck squamous cell carcinoma. The quarterly journal of nuclear medicine and molecular imaging: official publication of the Italian Association of Nuclear Medicine (AIMN)[and] the International Association of Radiopharmacology (IAR),[and] Section of the Society of... 2011. 55(5): p. 487-499.

9. Roh, J.-L., et al., Utility of 2-[18F] fluoro-2-deoxy-D-glucose positron emission tomography and positron emission tomography/computed tomography imaging in the preoperative staging of head and neck squamous cell carcinoma. Oral oncology, 2007. 43(9): p. 887-893.

10. Johansen, J., et al., FDG-PET/CT for detection of the unknown primary head and neck tumor. The quarterly journal of nuclear medicine and molecular imaging: official publication of the Italian Association of Nuclear Medicine (AIMN)[and] the International Association of Radiopharmacology (IAR),[and] Section of the Society of.. 2011. 55(5): p. 500-508.

11. Wong, W., et al., 18F-fluorodeoxyglucose positron emission tomography/computed tomography in the assessment of occult primary head and neck cancers—an audit and review of published studies. Clinical oncology, 2012. 24(3): p. 190-195.

12. Brouwer, J., et al., Screening for distant metastases in patients with head and neck cancer: Is there a role for 18FDG-PET? Oral oncology, 2006. 42(3): p. 275-280.

13. Lonneux, M., et al., Positron emission tomography with [18F] fluorodeoxyglucose improves staging and patient management in patients with head and neck squamous cell carcinoma: a multicenter prospective study. Journal of Clinical Oncology, 2010. 28(7): p. 1190-1195.

14. Strobel, K., et al., Head and neck squamous cell carcinoma (HNSCC)–detection of synchronous primaries with 18 F-FDG-PET/CT. European journal of nuclear medicine and molecular imaging, 2009. 36(6): p. 919-927.

15. Narayana, A., et al., Second primary tumors in laryngeal cancer: results of long-term follow-up. International Journal of Radiation Oncology Biology Physics, 1998. 42(3): p. 557-562.

16. Dinapoli, N., et al., Multidisciplinary approach in the treatment of T1 glottic cancer. Strahlentherapie und Onkologie, 2010. 186(11): p. 607-613.

17. Kyzas, P.A., et al., 18F-fluorodeoxyglucose positron emission tomography to evaluate cervical node metastases in patients with head and neck squamous cell carcinoma: a meta-analysis. Journal of the National Cancer Institute, 2008. 100(10): p. 712-720.

18. Smith, K.A., et al., Cost-effectiveness of positron emission tomography-CT in the evaluation of cancer of unknown primary of the head and neck. Head & neck, 2015. 37(12): p. 1781-1787.

19. Yoo, J., S. Henderson, and C. Walker-Dilks, Evidence-based guideline recommendations on the use of positron emission tomography imaging in head and neck cancer. Clinical Oncology, 2013. 25(4): p. e33-e66.

20. Schöder, H., et al., 18F-FDG PET/CT for detecting nodal metastases in patients with oral cancer staged N0 by clinical examination and CT/MRI. Journal of Nuclear Medicine, 2006. 47(5): p. 755-762.

21. Pfister, D.G., et al., Head and neck cancers. Journal of the National Comprehensive Cancer Network, 2011. 9(6): p. 596-650.

22. Buchbender, C., et al., Oncologic PET/MRI, part 1: tumors of the brain, head and neck, chest, abdomen, and pelvis. Journal of Nuclear Medicine, 2012. 53(6): p. 928-938.

23. Daisne, J.-F., et al., Tumor volume in pharyngolaryngeal squamous cell carcinoma: comparison at CT, MR imaging, and FDG PET and validation with surgical specimen. Radiology, 2004. 233(1): p. 93-100.

24. Arens, A., et al., FDG-PET/CT in radiation treatment planning of head and neck squamous cell carcinoma. Quarterly Journal of Nuclear Medicine and Molecular Imaging, 2011. 55(5): p. 521.

25. Schinagl, D.A., et al., Comparison of five segmentation tools for 18f-fluoro-deoxy-glucose–positron emission tomography–based target volume definition in head and neck cancer. International Journal of Radiation Oncology Biology Physics, 2007. 69(4): p. 1282-1289.

26. Troost, E.G., et al., Clinical evidence on PET–CT for radiation therapy planning in head and neck tumours. Radiotherapy and Oncology, 2010. 96(3): p. 328-334.

27. Lee, N.Y., et al., Fluorine-18-labeled fluoromisonidazole positron emission and computed tomography-guided intensity-modulated radiotherapy for head and neck cancer: a feasibility study. International Journal of Radiation Oncology Biology Physics, 2008. 70(1): p. 2-13.

28. Passero, V., et al., Response assessment by combined PET–CT scan versus CT scan alone using RECIST in patients with locally advanced head and neck cancer treated with chemoradiotherapy. Annals of oncology, 2010. 21(11): p. 2278-2283.

29. Weber, W.A., Assessing tumor response to therapy. Journal of nuclear medicine, 2009. 50(Suppl 1): p. 1S-10S.

30. Yao, M., et al., Clinical significance of postradiotherapy [18F]-fluorodeoxyglucose positron emission tomography imaging in management of head-and-neck cancer—a long-term outcome report. International Journal of Radiation Oncology Biology Physics, 2009. 74(1): p. 9-14.

31. Porceddu, S.V., et al., Results of a prospective study of positron emission tomography–directed management of residual nodal abnormalities in node-positive head and neck cancer after definitive radiotherapy with or without systemic therapy. Head & neck, 2011. 33(12): p. 1675-1682.

32. Higgins, K.A., et al., Analysis of pretreatment FDG-PET SUV parameters in head-and-neck cancer: tumor SUVmean has superior prognostic value. International Journal of Radiation Oncol-

# Congenital Lumbar hernia with lumbo-costo vertebral syndrome with ipsilateral short femur, tibial and fibular hemimelia

**Dr. Sanjay Khaladkar[1], Dr.Pooja Karanjule[1], Dr. Arijit Ghosh[1], Dr. Vaibhav Aher[1]**

*[1]Department of Radio-diagnosis, Dr. D. Y. Patil Medical College and Research Center, Dr. D.Y. Patil Vidyapeeth, Pimpri, Pune, India*

**ABSTRACT**

Congenital lumbar hernia is a rare anomaly. Congenital lumbar hernia is usually associated with lumbo-costo vertebral syndrome. Lumbo-costo vertebral syndrome is a condition that includes spinal anomalies like hemivertebrae, absent ribs, and abdominal wall muscle hypoplasia. It usually presents as a symptomatic large mass in lumbar triangle (either superior or inferior lumbar triangle). Congenital hernias occurred due to defects in the musculoskeletal system. These defects occur probably due to single somatic defect which occurs between 3-5 weeks of gestational age with resultant malformation of vertebral bodies, ribs and abdominal musculature. Incomplete form of lumbo-costo vertebral syndrome shows congenital hernia, spinal anomalies with no rib abnormalities. Congenital lumbar hernia occurs in superior lumbar triangle in lumbo-costo vertebral syndrome due to absence of 11th and 12th ribs with attenuation and weakened attachments of the involved adjacent musculature. We report a case of 2-year female child having swelling right lumbar region since birth due to congenital lumbar hernia with associated spinal anomalies.

***Keywords:*** Lumbar hernia, lumbo-costo vertebral syndrome, congenital, abdominal wall defect

## CASE REPORT

A 2 -year old female child presented with swelling in right lumbar region since birth which increased on crying. Her right thigh, leg and foot were small in size (Figure 1). Ultrasound of abdomen showed a large defect in abdominal wall in right lumbar region through which herniation of bowel loops was noted suggestive of lumbar hernia (Figure 2). Antero-posterior and lateral radiographs of dorso-lumbar spine were taken in view of abnormal curvature in dorso-lumbar spine. Radiographs revealed marked scoliosis in lumbar spine with convexity towards left. D12 vertebra showed butterfly vertebra with hypoplastic right half of vertebral body.L1 to L3 verte-

**Figure 1 – Photograph of patient showing (A) - right lumbar hernia, (B)- small sized right leg and foot.**

bral bodies showed butterfly vertebrae. There was partial agenesis of the Sacrum with absence of S4-S5 sacral segments. Right 11th and 12th ribs were absent. Discontinuity in pro-peritoneal fat planes was noted in right lumbar region through which bowel loop herniation was seen suggestive of lumbar hernia (Figure 3). Radiograph of right thigh and leg showed short right femur and hypoplastic (hemimelia) right tibia and fibula (Figure 4). MRI of Lumbo-Sacral spine showed partial sacral agenesis with absence of S4-S5 sacral segments, scoliosis of lumbar spine with convexity towards left. Butterfly D12 vertebra with hypoplastic right half, butterfly L1-L3 vertebrae, widened spinal canal in lumbar region. Syringomyelia was noted at D12-L1 level and defect

**Figure 2 – Ultrasound in right lumbar region (A, B) – showing defect in parietal peritoneum (marked by white arrow) in right lumbar region with herniation of colon suggestive of lumbar hernia.**

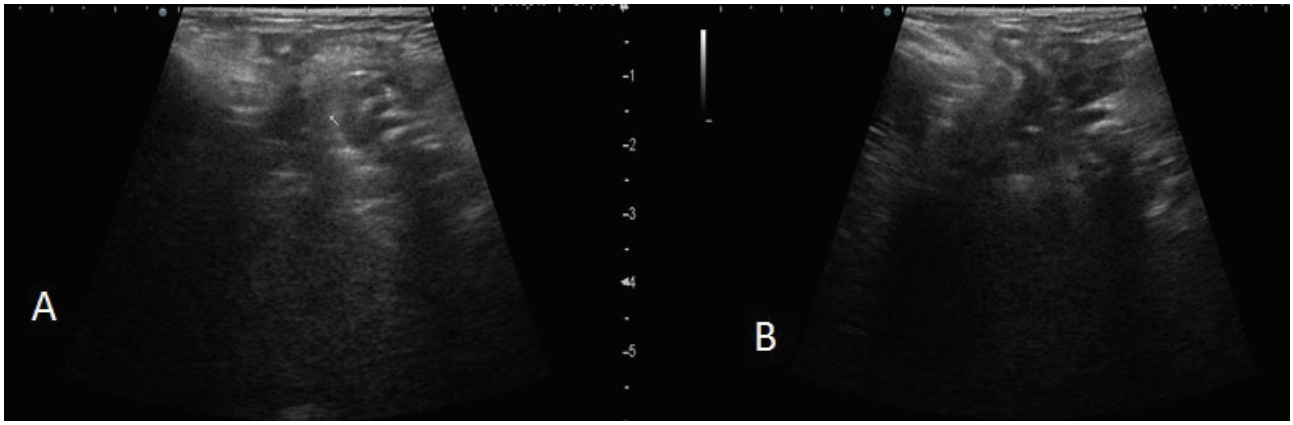


**Figure 3 – Radiograph of lumbosacral spine AP (A), lateral (B) showing multiple vertebral anomalies in lumbar spine, absent right 11th and 12th ribs with right lumbar hernia.**

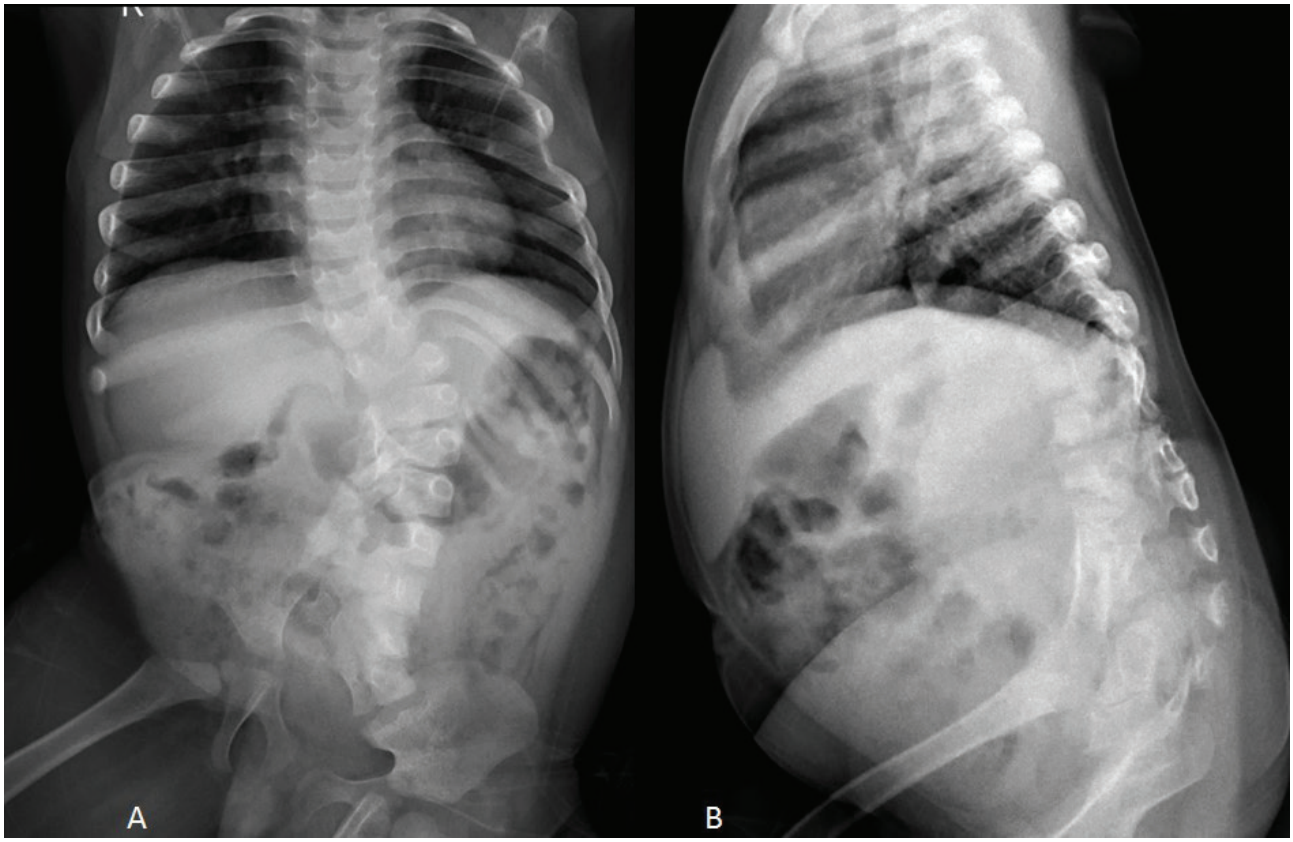

**Figure 4 – Radiograph of both thighs AP(A), right leg AP (B)- showing short right femur and right tibial and fibular hemimelia.**

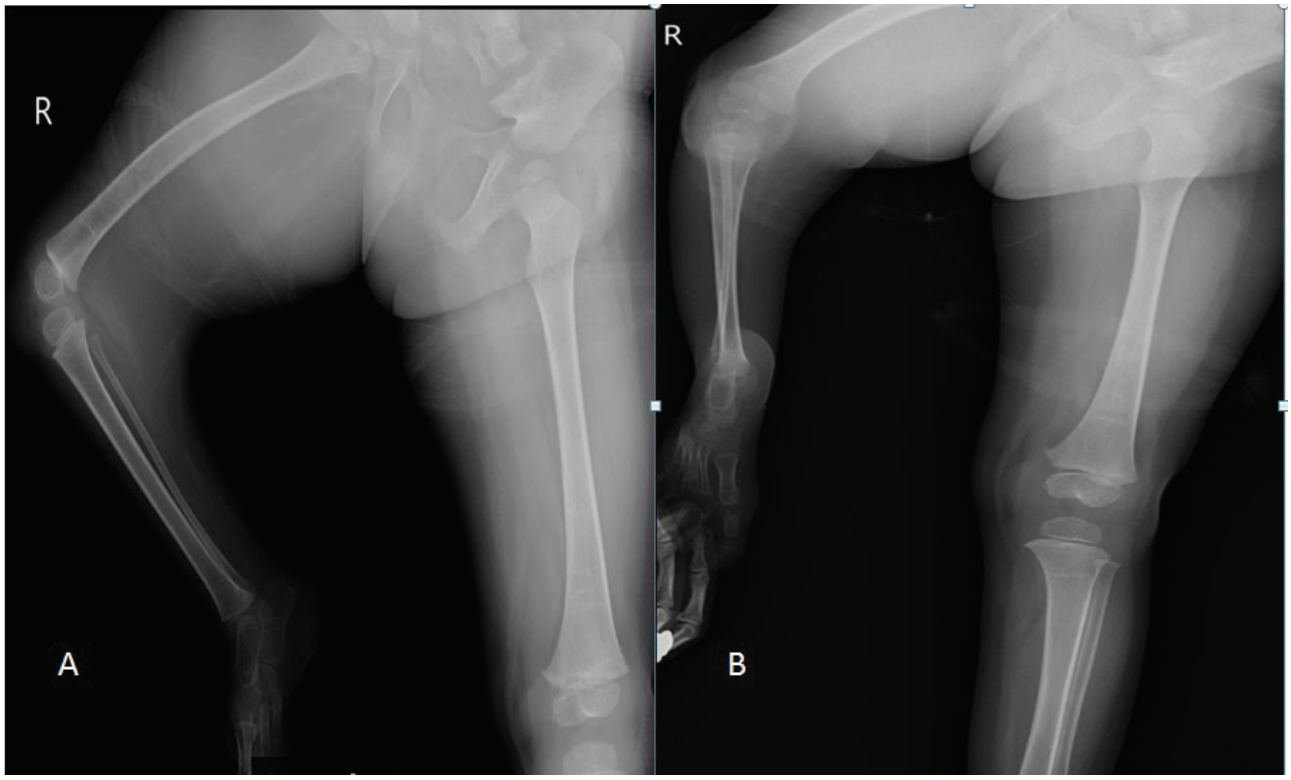


**Figure 5 – MRI Lumbo sacral spine Coronal STIR (A,B)- showing right lumbar hernia containing colon(A) and multiple vertebral anomalies in lumbar spine(B).**

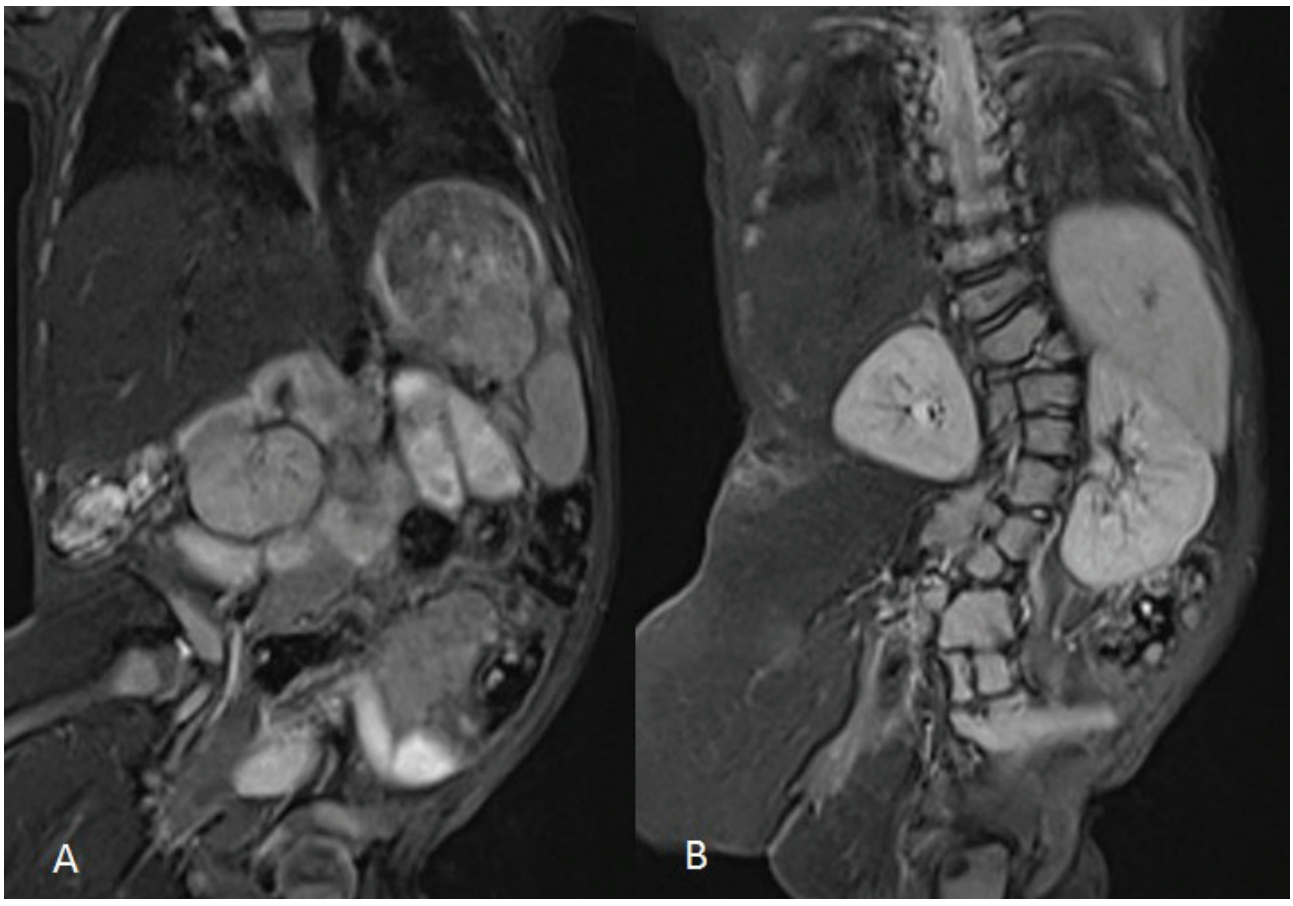

**Figure 6 – MRI Lumbosacral spine axial T1WI (A, B) and axial T2WI (C,D) showing right lumbar hernia containing right colon.**

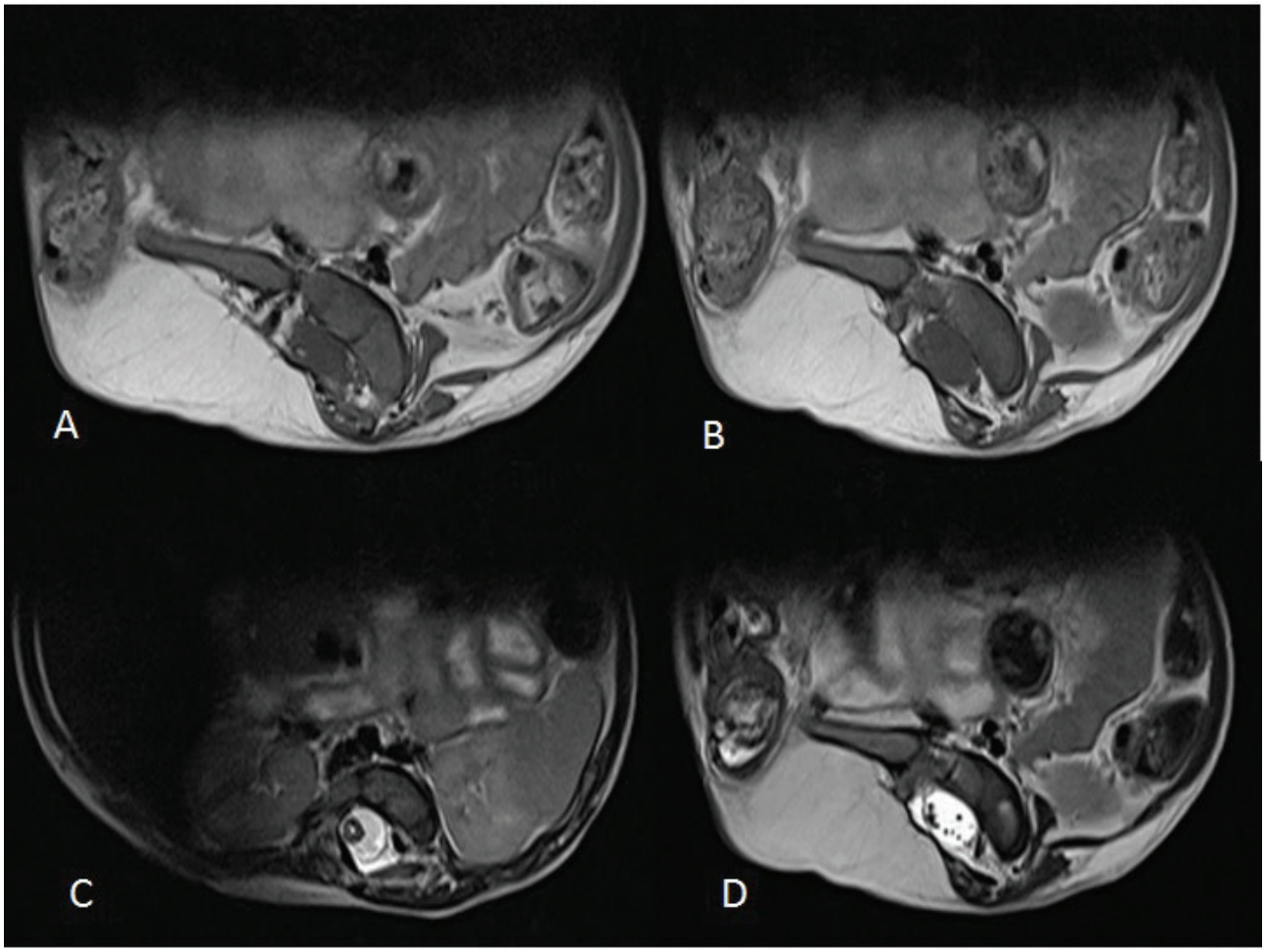


## DISCUSSION

Congenital lumbar hernia is a rare anomaly. Earliest report was made in 1803.1,2 Congenital lumbar hernia is usually associated with lumbo-costo vertebral syndrome. Lumbo-costo vertebral syndrome is a rare condition with only 16 cases reported in English literature.1 Lumbo-costo vertebral syndrome is a condition that includes spinal anomalies like hemivertebrae, absent ribs, and abdominal wall muscle hypoplasia. It usually presents as a symptomatic large mass in lumbar triangle (either superior or inferior lumbar triangle).[1] Lumbo-costo vertebral syndrome may be associated with other malformations like VACTERL association (Comprising vertebral anomalies, anal atresia, cardiac defects, trachea-oesophageal fistula, esophageal atresia, renal anomalies and limb abnormalities), diaphragmatic hernia, PUJ obstruction, renal agenesis, cloacal extrophy, cryptorchidism, hydrocephalus, focal nodular hyperplasia of the liver, spinal dysraphism, caudal deficiency, syndactyly. 3,4 Lumbo-costo vertebral syndrome may be seen in infant of diabetic mother.1 Lumbar hernia can be congenital (20% of total) or acquired ( 80%). Congenital hernias occurred due to defects in the musculoskeletal system. They occur individually or in association with other abdominal hernias, lumbo-costo vertebral syndrome and neurofibromatosis (Type1).5 Acquired lumbar hernia can be primary or secondary. Primary lumbar hernias (55%) are spontaneous without any causal factors like surgery, trauma, and infection. Secondary lumbar hernia (25%) occur due to blunt, penetrating or crushing trauma, surgical lesions, post-operative, infections in pelvic bone, ribs or lumbodorsal fascia, infected retroperitoneal hematomas, hepatic abscess. Tovloukian in 1972 first described lumbo-costo vertebral

syndrome.[6] Lumbo-costo vertebral syndrome includes abdominal wall muscular hypoplasia, congenital absence of ribs, hemi-vertebrae and anterior myelomeningocoele. These defects occur probably due to single somatic defect which occurs between 3-5 weeks of gestational age with resultant malformation of vertebral bodies, ribs and abdominal musculature. The crown rump length of embryo is 1.5 mm between 3-5 weeks of gestational age when mesoderm between the endoderm and ectoderm on either sides of notochord differentiation into somites which differentiate into the sclerotome (which form the vertebrae and costal process and the myotome (that forms skeletal muscle of tongue and the dermatome (which forms skin and subcutaneous tissue). Vertebral, costal and abdominal wall defects can occur if there is any disturbance during this stage like anoxia demonstrated in animal study. Neurulation occurs during the 3-5 gestational age during which formation neural groove, closure of anterior (25 days) and posterior (27-28 days) neuropores, appearance of ventral horn cells, formation of anterior and posterior roots and disc junction of neuroectoderm from the surface ectoderm occurs.[7] Hence lumbo-costo vertebral syndrome can be associated with spinal cord malformations. Hence spinal dysraphism may be also associated.[7] Other anomalies associated with LCVS are congenital sciatic hernia / absent tibia, post myelomeningocoele. Rarely lumbo-costo vertebral syndrome may be associated with congenital subcostal hernia.[8] Etiologies of both subcostal hernia and lumbar hernia are same in lumbo-costo vertebral syndrome. Anomalies associated with lumbo-costo vertebral syndrome are lung hypoplasia, supernumery digits, undescended testis, hydrocephalus due to Arnold Chiari malformation, hypoplastic sacrum.[9] Incomplete form of lumbo-costo vertebral syndrome shows congenital hernia, spinal anomalies with no rib abnormalities.[10] Less than 50 cases of congenital lumbar hernia associated with other congenital anomalies have been reported in English literature.[11] Predisposition of lumbar hernia in superior triangle is due to multitude of factors like length and angulation of rib, size of the quadratus lumborum, serratus posterior muscles, the insertion of latissimus dorsa between 11th and 12th ribs, variable insertion of external oblique muscle above the 12th rib.[11] Due to absence of 11th and 12th rib ,the involved adjacent musculature is attenuated with weakened attachments. Hence congenital lumbar hernia occurs in superior lumbar triangle in lumbo-costo vertebral syndrome.[11] Other abnormalities associated are congenital club foot, arthrogryposis.[11]

## CONCLUSION

Congenital lumbar hernia is rare and occurs in superior lumbar triangle. It is often associated with spinal and rib anomalies in lumbo-costo-vertebral syndrome. Incomplete form of lumbo-costo vertebral syndrome shows congenital lumbar hernia, spinal anomalies with no rib abnormalities. Other associated congenital anomalies may be seen.

## REFERENCES

1. Okumus N, Bas AY, Demirel N, Zenciroglu A, Surmeli S, Ceylaner S. Lumbocostovertebral syndrome in an infant of a diabetic mother. Am J Med Genet A. 2010;152A(6):1374-1377.

2. Sharma A, Pandey A, Rawat J, Ahmed I, Wakhlu A, Kureel SN. Congenital lumbar hernia: 20 years' single centre experience. J Paediatr Child Health. 2012;48(11):1001-1003.

3.Lyngdoh TS, Mahalik S, Naredi B, Samujh R, Khanna S. Lumbocostovertebral syndrome with associated VACTERL anomaly. J Pediatr Surg. 2010;45(9):e15-e17.

4.Singh G, Ahuja S, Kumar R, et al. Posterior spinal dysraphism with lumbocostovertebral syndrome.Br J Neurosurg. 2010;24(2):216-218.

5. Rehman S, Muqim R, Hassan R, Zarin M, Wazir MA, Aurangzeb M. Inferior lumbar hernia of petit in a patient with neurofibromatosis Type-1. Pak J Med Sci 2009;25(6):1015-1017.

6. Touloukian RJ. The lumbocostovertebral syndrome: A single somatic defect. Surgery. 1972;71:174-81.

7. Kumar G S, Kulkarni V, Haran R P Lumbo-costo-vertebral syndrome with posterior spinal dysraphism Neurology India , September 2005, volume 53, issue 3, 351-353

8. Muncie C , Christopher Ng ,Giles H ,Blewett C Congenital subcostal hernia in a patient with Lumbo-Costovertebral Syndrome, case report and review of the literature, J Ped Surg Case Reports 14 (2016) 49-51

9. Harris K, Dorn C, Bloom B.Lumbocostovertebral syndrome with associated VACTERL anomalad: a neonatal case report.J Perinatol. 2009 Dec;29(12):826-7 PMID: 19935732

10. Krishnamurthy S, Kapoor S.An incomplete form of lumbocostovertebral syndrome in association with atrial septal defect, arthrogryposis and clubfeet.Indian J Pediatr. 2009 Apr;76(4):411-3 PMID: 19205643
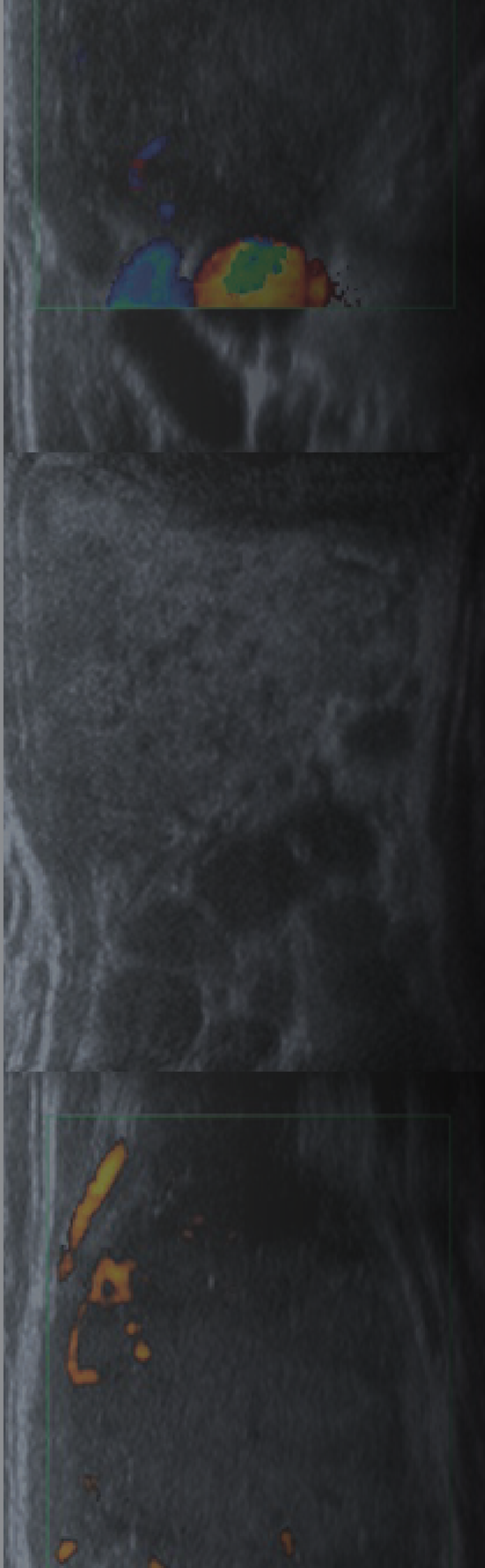
11. Vagholkar K, Dastoor K Congenital lumbar hernia with lumbocostovertebral syndrome: a case report and review of the literature Case Rep Pediatr. 2013;2013:532910.PMID: 24159401 PMCID: PMC3789277.